Université de Montréal

A New Avalanche Model for Solar Flares

par

Laura F. Morales

Département de Physique

Faculté des arts et des sciences

Thése présentée à la Faculté des études Supérieures

en vue de l'obtention du grade de

Philosophiæ Doctor (Ph.D.) en Physique

Decembre, 2008

Université de Montréal

Faculté des études supérieures

Cette thése intitulée:

A New Avalanche Model for Solar Flares

présenté par:

Laura F. Morales

a été évalué par un jury composé des personnes suivantes:

François Wesemael, président-rapporteur

Paul Charbonneau, directeur de recherche

Alain Vincent, membre du jury

Markus J. Aschwanden, examinateur externe

Michel Delfour, représentant du doyen de la FES

Thése acceptée le:_____

ABSTRACT

The solar corona is formed by a magnetized plasma characterized by temperatures of the order of 2×10^6 degrees Kelvin. When a solar eruption takes place the temperature can reach locally values in excess of 10^7 degrees. Many physical explanations and models were proposed to explain this coronal heating. In 1988, Parker suggested a physical scenario that may lead to the dissipation of huge amounts of energy, via a great many small-scale energy release events which he called: *nanoflares*. Parker's model can be interpreted like a model for eruptions of all sizes. However, considering the enormous disparity between the various time and space scales involved, it is not advisable to try to solve the problem starting from the magnetohydrodynamical equations. On the other hand, all physical components required to produce a self-organised critical (SOC) state appear in Parker's model: a dissipative system subject to a local threshold instability which requires a triggering condition (magnetic reconnection), and an external mechanical forcing on a long time scale compared to the dynamical time scales. Such systems are interaction-dominated and their dynamical behavior is an emergent property of the relatively simple interaction between many degrees of freedom.

In this work, we developed a new generation of self-organized critical models for solar flares. We designed a cellular automaton based on an idealized representation of a coronal loop as a bundle of magnetic flux strands wrapping around one another. This system produced avalanches of reconnection events characterized by scale-free size distributions that compare favorably with the corresponding size distribution of solar flares, as inferred observationally. We calculated the spreading exponents that characterize such avalanches and could show that they satisfy the mutual numerical relationships expected in SOC systems. We also produced synthetic loops and study the geometrical properties and fractal dimensions of projected synthetic flares gener-

ated by the model. In all cases the model produced robust results that compare well with observations, while resolving many discrepancies and interpretative ambiguities presented by earlier SOC models.

Subject headings:

Solar Physics, Astrophysics, and Astronomy: Solar Corona, Solar Flares

Space Plasma Physics: Nonlinear phenomena, Magnetic Reconnection, Self-organized criticality

RÉSUMÉ

La couronne solaire est constituée d'un plasma magnétisé atteignant des températures d'environ 2×10^6 degrés Kelvin. Quand une éruption solaire se produit, la couronne atteint localement des températures pouvant dépasser 10^7 degrés. Plusieurs scénarios physiques on été élaborés pour expliquer ce chauffage coronal. En 1998, Parker en a suggéré un qui pourrait à la fois mener à la dissipation de quantités d'énergie suffisantes pour chauffer la couronne, et expliquer les éruptions solaires. L'hypothèse de Parker peut être interprétée comme un modèle applicable à toutes les éruptions de toutes les grandeurs possibles mais, si on considére l'énorme écart entre les différentes échelles temporelles et spatiales impliquées, il ne semble pas une bonne idée d'essayer de résoudre le problème en partant des équations de la magnétohydrodynamique. Cependant, toutes les composantes physiques nécessaires pour produire un état critique auto-régulé (SOC) sont présentes dans le modèle de Parker: un système dissipatif sujet à une instabilité locale qui exige une condition de déclenchement avec seuil (reconnexion magnétique) et un forçage externe mécanique caractérisé par une échelle temporelle plus grande que les échelles temporelles dynamiques. De tels systèmes sont dominés par les interactions, et leur comportement dynamique est une propriété globale émergeant de l'interaction assez simple entre plusieurs degrés de liberté.

Dans ce travail nous avons développé une nouvelle génération de modèles SOC applicables aux éruptions solaires. Ce nouveau modèle numérique est basé sur un automate cellulaire définissant une représentation idéalisée d'une boucle coronale comme un ensemble de lignes de flux magnétique entortillées entre elles. Ce système produit des avalanches d'épisodes de reconnexion magnétique caractérisés par une vaste gamme d'échelles spatiales et temporelles. Les propriétés statistiques de ces avalanches sont en bon accord avec les résultats observationnels au niveau des fonctions de densité de probabilité des taille, durée et énergie des éruptions solaires. Nous avons également calculé

les exposants de propagation qui caractérisent les avalanches et avons démontré que ces exposantes satisfont aux relations numériques attendues d'un système SOC. Nous avons, à partir des simulations, reconstruit des boucles coronales de géométrie réaliste et avons démontré que l'indice fractal des avalanches projetées sur la ligne de visée se compare bien aux observations. Dans tous les cas, le modèle s'est montré robuste, tout en corrigeant plusieurs des écarts et difficultés conceptuelles d'interprétation associés aux modèles SOC antérieurs.

Mots clefs:

Physique solaire, astrophysique, et astronomie: Couronne Solaire, Éruptions solaires
Physique des plasmas de l'espace: Phénomènes non linéaires, Criticalité Auto-régulée, Reconnexion Magnétique

...vi en el Aleph la tierra,
y en la tierra otra vez el Aleph
y en el Aleph la tierra,
vi mi cara y mis vísceras,
vi tu cara, y sentí vértigo y lloré
porque mis ojos habían visto ese objeto secreto y conjetural
cuyo nombre usurpan los hombres,
pero que ningún hombre ha mirado: el inconcebible universo.

Jorge Luis Borges, 'El Aleph', 1949

Contents

List of Figures

List of Tables

Chapter 1

Introduction

The Sun is the main source of light, heat and energy of our planet. Mankind has been trying to understand how it works, why it changes, and how these changes influence life on Earth for more than three thousand years.

Total eclipses of the Sun have been observed for centuries with the naked eye. In fact the oldest eclipse records can be situated around 1300 years B.C. For a lucky coincidence when an eclipse occurs the Moon covers the total Sun's disk unveiling in this way its most tenuous atmosphere: the solar corona. For this reason, there is a close relation between eclipse observations and the solar corona.

In the twelfth century some atmospheric features such as sunspots and solar prominences were somehow registered (see [Van Helden, 1996]) but it was only with the invention of the telescope that the Sun's atmosphere was systematically observed. It was in the early decades of the 17th century that Johann Goldsmid, Thomas Harriout, Christopher Scheiner and Galileo Galilei himself acknowledged the existence of sunspots. This observations were continued throughout the rest of that century by Johannes Hevelius and Jean Picard.

Early sunspots observers had noted the curious fact that sunspots rarely appear outside of a latitudinal band of about 30° centered about the solar equator, but could not discover any clear pattern in the appearance and disappearance of sunspots. In fact, sunspots had been numerously reported for more than a hundred years but it was only in 1826 that an actual systematic observation survey was performed. Samuel Heinrich Schwabe wanted to discover intra-mercurial planets. He thought that the best way to do that was to document the apparent shadows that the intra-mercurial planets would cast upon crossing the visible solar disk during conjunction. This program posed a big problem: he might confuse the planets with small sunspots. In order to avoid such a problem Schwabe registered the position of every sunspot visible on the solar disk on any clear day. Finally, after 17 consecutive years of observations, Schwabe found no intra-mercurial planets; instead, his observations revealed that the number of sunspots increased and decreased in a cyclic way. He estimated this period to be around 10 years.

Some years later the cyclic time evolution of sunspots number was compared with the time evolution of geomagnetic activity by Edward Sabine. He concluded that both sets of data were "absolutely identical". His discovery indicated that the Sun provides the Earth with more than light and heat and marked the beginning of Sun-Earth-connection research.

Around the 1860's two other phenomena were discovered in the solar corona: solar flares (in 1859) and coronal mass ejections (1860). Even though the solar atmosphere was intensively observed the physical nature of sunspots was unknown until 1908 when George Hale discovered the existence of magnetic fields in sunspots on the basis of the Zeeman splitting of the sunspots spectra. This was a groundbreaking discovery not only for the solar physics community but to astronomers in general since the existence of magnetic fields outside the Earth's environment was conclusively established for the first time with Hale's observations.

With Hale's discovery the problem of studying the coronal plasma, that up to the moment was thought as a simple fluid that could be described using the hydrodynamics equations, turned into a much more complicated task and opened a whole new field of research. Scientists tried to give answers to new questions such as: how and where is the magnetic field generated; how does magnetic field influence the other coronal phenomena such as flares and coronal mass ejections and ultimately, how does the Sun's magnetic field affects the Earth's magnetosphere.

In particular, modeling the solar flare phenomena requires solving a set of non-linear equations: *magnetohydrodynamics equations*. This set of equations can only be analytically solved in very restrictive situations and so to be able to do predictions it is necessary to attack the problem using numerical simulations. Unfortunately, for solar flares a numerical simulation needs to resolve a wide range of temporal and spatial scales. In this context, in 1991 Lu & Hamilton ([Lu & Hamilton, 1991]) suggested that self-organized criticality (SOC) could be a new and simpler tool that may help to understand and ultimately predict solar flares. Their work ushered in a whole new branch in solar flares studies that produced outstanding results during a decade but had reached a stagnation point. In this work we try to take a major step forward by proposing a new SOC model for solar flares that deals with many of the problems presented by classical SOC models and their immediate descendants.

The rest of this chapter goes as follow: First we discuss the solar corona in general and solar flares in particular; then we go through some of the most important models of solar flares: starting from a diffusion model, advancing through magnetic reconnection model and finishing with Parker's vision. We proceed by presenting the classical SOC model for solar flares, together with the main mathematical tools for analyzing the cellular automaton results. We conclude by discussing the physical pros and cons of classical SOC models.

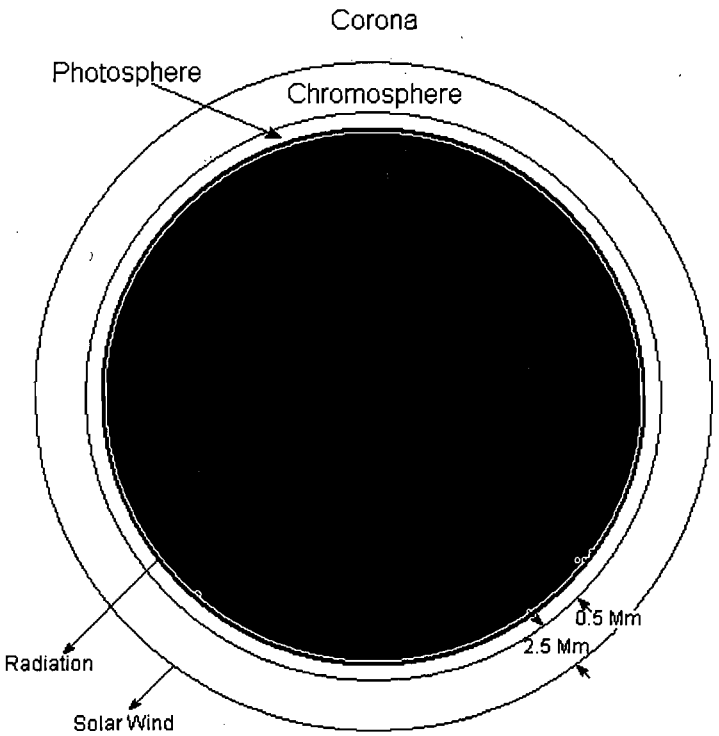

Figure 1.1: Three-layered structure of the solar atmosphere (adapted from [Kivelson & Russel, 1995].

1.1 The Solar Atmosphere

The atmosphere of the sun is formed by three layers, each of them featuring substantial different properties such as the density and the temperature. These three regions are: the photosphere, the chromosphere and the corona (see figure 1.1). In the following paragraphs we describe briefly each of them.

The **photosphere** is the visible surface of the Sun. Strictly speaking the photosphere is the layer where the optical depth becomes $\tau \sim 1$. Because of its gaseous nature it is not a solid surface but rather a fictitious spherical surface, approximately 100 km thick, from which the bulk of solar radiation originates. Within this region the temperature of the gas decreases from a value of ~ 6500 K at the base, to a minimum

of ~ 4400 K at the top. The photosphere is neither uniformly bright nor perfectly still; it includes different characteristic elements such as: dark sunspots, bright faculae, and granules which cover the whole Sun at the photospheric level (except the areas covered by sunspots). The typical scale of granulation varies between 300 km and 2000 km with average velocities of ~ 1.5 km/s and mean lifetime of 10 minutes. Larger granules can also be found in the photosphere, the supergranules, and have an average size of about ~ 35000 km across; individual supergranules last for a day or two and have flow speeds of about ~ 0.5 km/s.

The photospheric magnetic field is far from being dipolar, which is the common assumption in other stars. Actually it consists of small magnetic elements that are shuffled around and evolve rather rapidly. However, these small-scale features are organized into some large-scale patterns, namely sunspots, plage regions, large-scale unipolar areas, supergranulation fields and ephemeral regions.

Sunspots represent large concentrations of magnetic flux and are much cooler than their surroundings while plage regions are part of an active region outside the sunspot. Large-scale unipolar regions extend over $\sim 1 \times 10^5$ km in both longitude and latitude. They contain elements of predominantly one polarity and have long life times. These regions seem to rotate faster than the photospheric plasma and show less differential rotation. The supergranulation field consists of the magnetic flux which is concentrated at the supergranule boundaries, while ephemeral regions are basically tiny bipolar magnetic fields.

The **chromosphere** is an irregular layer above the photosphere where the density drops by nearly a factor of 10^4 and where the temperature begins to rise with increasing altitude, reaching about 20000 K. Above the chromosphere the temperature rises extremely rapidly reaching a temperature of $\sim 10^6$ K in a hundred kilometers (see figure 1.2). This region is known as the **transition region**.

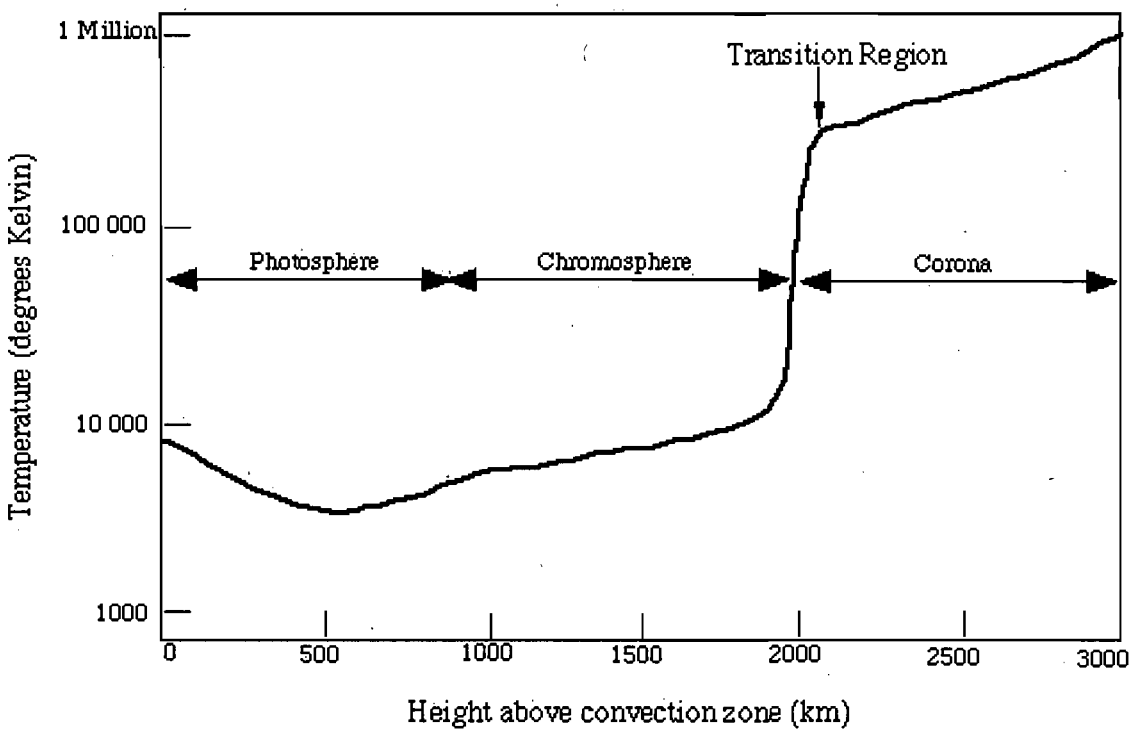

Figure 1.2: Solar atmospheric temperature vs height.
http://solar.physics.montana.edu/YPOP/Spotlight/SunInfo/transreg.html

The outer solar atmosphere is the **corona**. It extends out into space for several solar radii. Because of its temperature much of the coronal emission is generated in ultraviolet and X-ray wavelengths. These wavelength range are mostly absorbed by the Earth's atmosphere so current coronal observations are made from space. The coronal plasma consists mostly of electrons and protons with a small percentage of ionized helium. The solar corona is permeated by magnetic fields. Its electrical conductivity is very high so the magnetic field moves along with the fluid. This phenomena is known as the *frozen-in condition.*

The high temperature of the corona reveals the existence of some type of mechanical energy input since thermodynamic equilibrium would normally require the temperature

Loss Mechanism	*Quiet Sun* *	*Active region* *	*Coronal Hole* *
Thermal Conduction	2.10^5	$10^5 - 10^7$	6.10^4
Radiation	10^5	5.10^6	10^4
Solar wind	$< 5.10^4$	$< 10^5$	7.10^5

Table 1.1: Average coronal energy losses [Withbroe, 1981] ($^*\,\mathrm{erg\,cm^{-2}sec^{-1}}$).

to fall as one moves outward. Assuming that the outer atmosphere is in a steady state, it is possible to estimate the energy input by means of the energy loss. Essentially, there are three main mechanisms involved in coronal energy losses: (1) thermal conduction, both inwards toward the transition layer and the upper chromosphere and outwards into the solar wind, (2) radiation and (3) the energetic requirements of the solar wind. These quantities vary significantly in different parts of the corona as shown in table (1.1). From those values we can deduce that the total need of energy for the corona is about 10^7 $\mathrm{erg\,cm^{-2}\,sec^{-1}}$ [Parker, 1988].

Although many efforts have been made in the last decades, the question of how the solar corona is heated to its temperature of millions of degrees has not been fully answered yet. However, among the different features observed in the Sun such as eruptions and instabilities, solar flares seem to have one thing in common: when a flare occurs, the plasma reaches temperatures of 10^7 K or greater. The collective energy release by all flares can be considered a coronal heating mechanism, albeit spatially and temporally intermittent. In the following section we will describe some basic facts about solar flares.

1.2 Solar Flares

The exact definition of what a solar flare is has evolved and become more complex since flares were first identified on the sun's photosphere in independent observations performed by [Carrington, 1859] and [Hodgson, 1859]. Nowadays the solar community agrees that *"...a solar flare is a process associated with a rapid temporary release of energy in the solar corona triggered by an instability of the underlying magnetic field configuration that evolves into a more stable state by changing and reconnecting the magnetic topology. As a result of this process nonthermal particles are accelerated and the coronal/chromospheric plasma is heated"* [Aschwanden, 2006].

1.2.1 Solar flare observations

From the very first (documented) detection of a solar flare performed by [Carrington, 1859] (see a reproduction of his hand made drawing in figure 1.3) to the images captured more recently by Hinode and Stereo, solar physicists have managed to obtain a wide variety and a great quantity of data from the energetic events occurring at the solar atmosphere. In this section we describe the most important observational concepts related to solar flares.

Solar flares have been detected over a large range of wavelengths and also by a great variety of techniques. Flares emit high levels of radiation at wavelengths from the radio spectrum (10 km) to short-wavelength or even gamma rays (10^{-16} km) and release energies ranging between 10^{27} to 10^{33} ergs. In figure 1.4 we show a typical example of solar flare as observed in X-rays. The sequence begins with the active region observed on July 2nd of 1993. The activity increases from July 3rd to 4th peaking on July 4th and decreases again on July 5th.

Flares are usually classified by their emissivity in different wavelengths. Two main classification schemes are generally used: the H_α importance and the soft $X - ray$

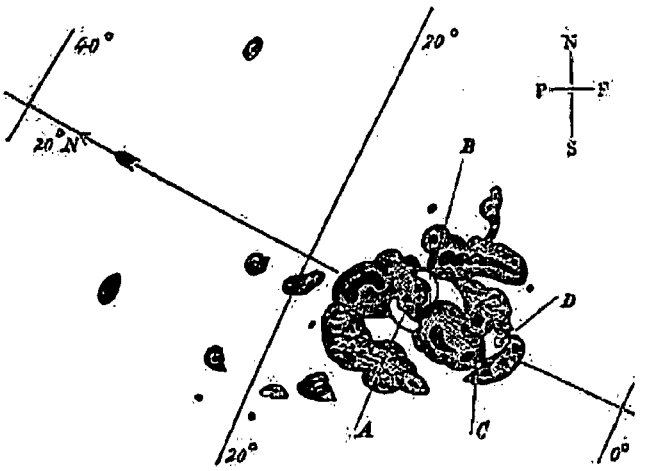

Figure 1.3: Reproduction of a drawing by R.C. Carrington showing the location of the flare he observed while making a drawing of an active region [Carrington, 1859].

classification. The H_α-lines have the advantage of being formed in the visible region of the spectrum and of reacting strongly to the presence of a flare. They provide two pieces of information: the area covered by the flare, known as the importance or class of the flare (see classification on table (1.2)) and the strength of the H_α emission in the flaring region, known as the brightness. Flare brightness-scale is indicated by f faint; n normal and b brilliant. A flare covering 1000 millionth of the disk and with exceptionally bright H_α emission is a $3b - flare$.

On the other hand $X - ray$ classification is based on the integrated total output of soft $X - rays$ detected in the wavelength range of 1 to 8 $\AA$. With this information the strength of the flare is defined by the value of the peak intensity in units of power over length square as shown in figure 1.5. The most intense flares are the *X-class*. They can trigger planet-wide radio blackouts and long-lasting radiation storms, their intensity is 10^{-1} erg cm^{-2} s^{-1}, greater flares are designated by adding a number to the

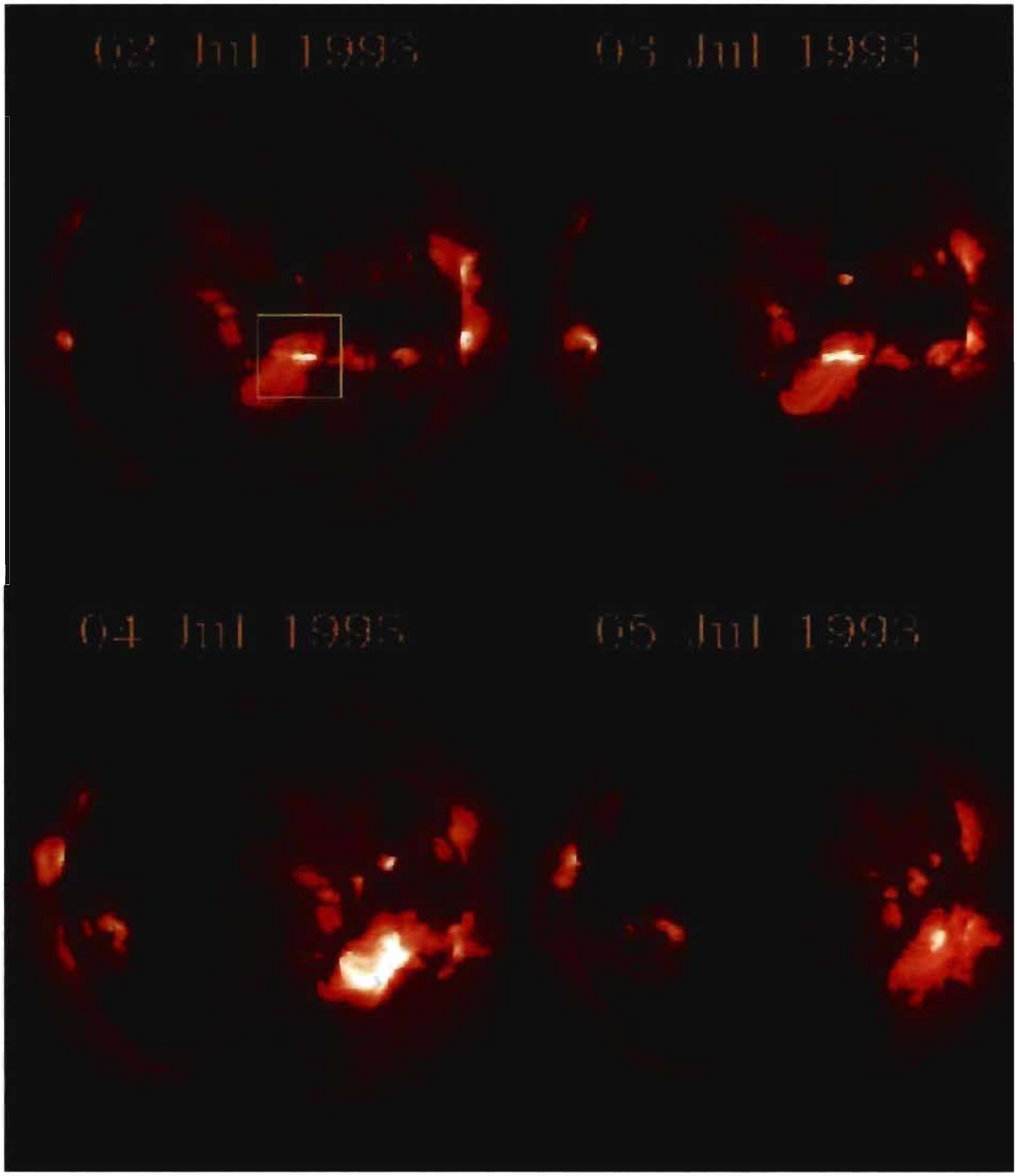

Figure 1.4: A sequence of a flaring region observed in X-rays by Yohhoh. http://www.hao.ucar.edu/Public/education/slides/slide15.html

Area (*)	Importance
< 100	S (subflare)
$100 - 250$	1
$250 - 600$	2
$600 - 1200$	3
> 1200	4

Table 1.2: The importance classification of solar flares (* in millionths of a solar hemisphere).

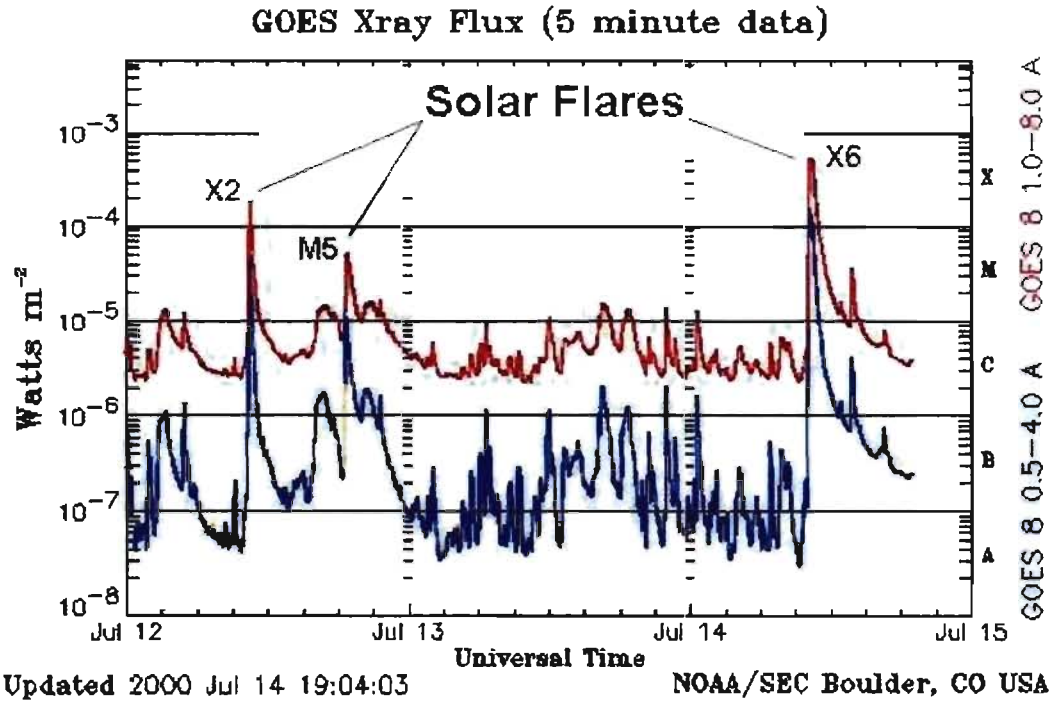

Figure 1.5: Two X-class flares and M-class detected by NOAA satellites in July 2000. http://cse.ssl.berkeley.edu/hess_epo/html/xraysolarflares_ifiles/flareclasses.html

letter X thus and *X20* flare has an intensity of 2 $\mathrm{erg\,cm^{-2}\,s^{-1}}$ (20 times the intensity of an X flare). *M-class* flares are medium-size with an intensity ten times smaller than X flares. The least intense flares that can be observed but that have almost no influence on the Earth environment are C and B flares. Their intensities are 10^{-3} $\mathrm{erg\,cm^{-2}\,s^{-1}}$ and 10^{-4} $\mathrm{erg\,cm^{-2}s^{-1}}$ respectively.

From figure 1.5 it is apparent that in flare phenomena we can identify two different stages: the rising phase and the thermalization phase. The former is characterized by a rapid (couple of seconds) increase of energy while in the latter, energy decreases with a smoother slope that can last hundreds of seconds.

When analyzing many hundred of thousands of recorded flares observers found that the frequency distribution of the energy released by flares had the form of a tight power law, spanning at least eight orders of magnitude in flare energy [Aschwanden et al., 2000]. Specifically, if $f(E)dE$ is the fraction of flares releasing an amount of energy between E and $E + dE$ per unit of time the frequency distribution takes the form:

$$f(E) = f_0\, E^{-\alpha} \tag{1.1}$$

with $\alpha > 0$. This power-law is indicative of the absence of a typical scale for the releasing of energy meaning that the system behaves in a self-similar way.

In table (1.3) we present recent determinations of flare power-law indices for the energy release. Translating the observed flare X-ray or EUV fluxes to volumetric energy release is a very complex task that involves many assumptions such as: the geometrical shape of the flaring region, the physical conditions within the flare volume and the mechanism responsible for the emission of hard radiation (for more details in [Lee et al, 1993]). In fact the definition of what is to be considered a flare depends strongly on the detection threshold and the temporal and spatial limits imposed by detection instruments (a complete discussion on the subject can be found in [Aschwanden et al., 2000]). In these observational and data analysis difficulties lies the

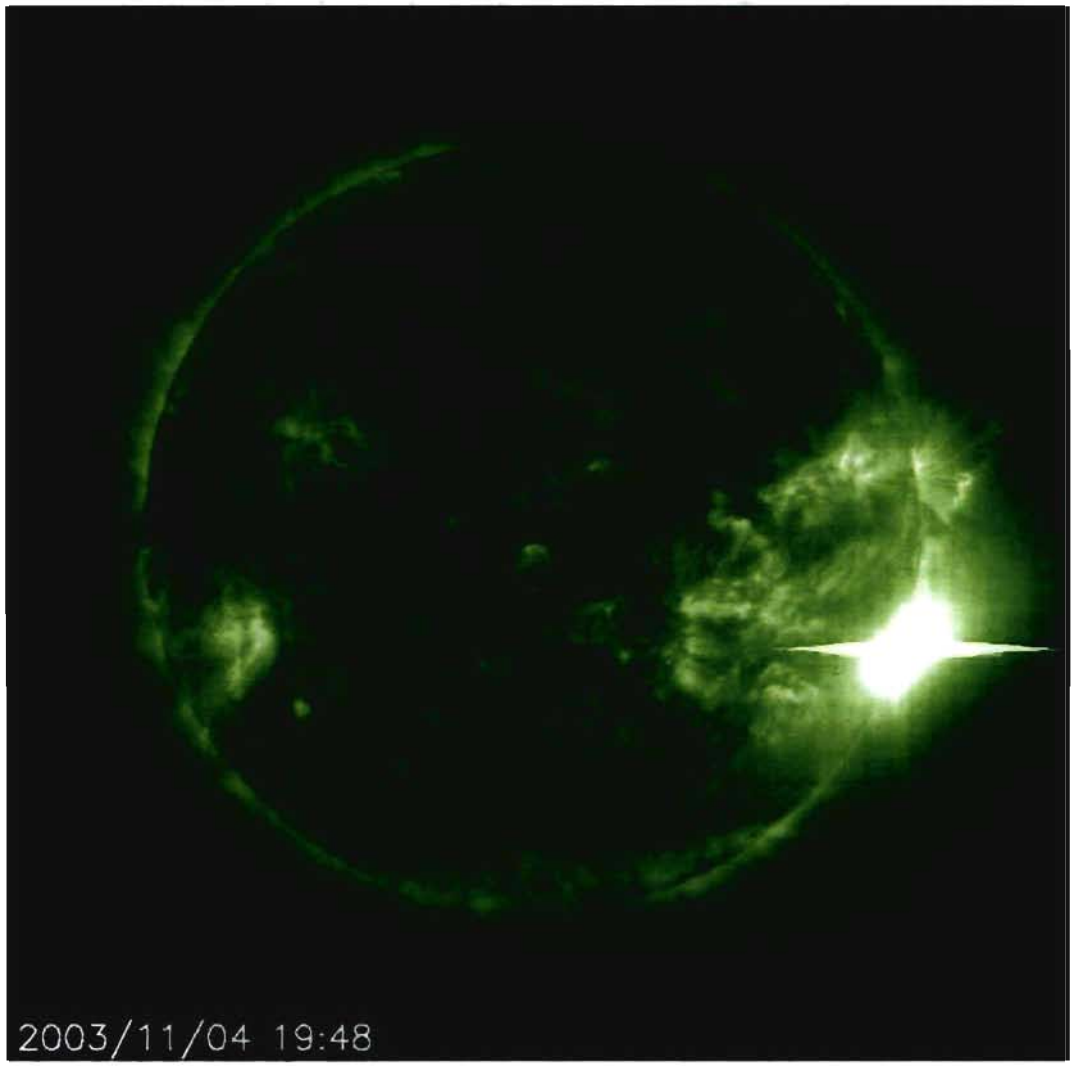

Figure 1.6: X28 flare in EIT 195 filter observed on 4th November 2003. It saturated the $X - ray$ detector aboard NOAA's GOES satellite that monitors the Sun http://sohowww.nascom.nasa.gov/.

Data	*Instrument*	*Reference*	α_E
HXR	WATCH/GRANAT	Crosby et al 1998	1.39 ± 0.02
HXR	SMM/HXRBS	Crosby et al 2000	1.53 ± 0.02
HXR	ISEE 3/ICE	Bromund et al 1995	1.67 ± 0.02
SXR	YOKKOH/SXT	Shimizu 1995	$1.5 - 1.6$
EUV	SOHO/EIT	Krucker & Benz 1998	$2.3 - 2.6$
EUV	TRACE	Parnell & Jupp 2000	$2.02 - 2.56$
EUV	TRACE	Aschwanden et al 2000	1.79 ± 0.08

Table 1.3: Observational determinations of flare power-law indices for the energy release.

reason for the significantly variation between the power-law indices reported in table (1.3) even when in some cases the same instruments have been used.

In order to understand and predict solar flares many models have arisen, each of them featuring different characteristics. Nevertheless, there is universal agreement on the fact that the magnetic fields is the main ingredient and plays a crucial role both as an energy source and as a trigger mechanism. In the following section, we present a standard model of solar flares that takes this fact into account.

1.3 A simple model of solar flares

The magnetic structure of the magnetic field around sunspots is the key concept when modeling the occurrence of flares. Flares almost always occur in active regions which, in their simplest form, are bipolar magnetic structures, consisting of adjacent patches of outwardly and inwardly oriented magnetic field, as shown in figure 1.7. To describe a magnetized plasma like the one existing in the coronal environment we use

Figure 1.7: Ultraviolet-light image of coronal loops. Large arcs of gas and energetic particles confined by the magnetic field that make up the solar corona are seen by the the TRACE satellite telescope.
http://www.gsfc.nasa.gov/gsfc/spacesci/sun_earth/tracecl.htm

the magnetohydrodynamic (MHD) equations. The MHD approximation embodies the conservations principles derived from the equations of fluid dynamics and electromagnetism.

If ρ is the mass density of the magnetic fluid and $\boldsymbol{v}$ is the flow field the mass conservation equation takes the form:

$$\frac{\partial \rho}{\partial t} - \boldsymbol{v} \cdot \nabla \rho = -\rho \nabla \cdot \boldsymbol{v} \,. \tag{1.2}$$

In the incompressible case, equation (1.2) can be written as: $\nabla \cdot \boldsymbol{v} = 0$.

The Navier Stokes equation that expresses the momentum conservation is:

$$\frac{\partial \boldsymbol{v}}{\partial t} + (\boldsymbol{v} \cdot \nabla)\boldsymbol{v} = \frac{1}{4\pi\rho}(\nabla \times \boldsymbol{B}) \times \boldsymbol{B} - \frac{1}{\rho}\nabla p + \nu \nabla^2 \boldsymbol{v} \tag{1.3}$$

where $\boldsymbol{B}$ is the magnetic field, P is the fluid pressure and ν is the kinematic viscosity.

The magnetic field is related to the current density and electric field by Ohm's law which, for the case of a neutral nonrelativistic fluid, takes the simplified form:

$$\sigma(\boldsymbol{E} + \frac{\boldsymbol{v}}{c} \times \boldsymbol{B}) = \boldsymbol{j} \,, \tag{1.4}$$

where σ is the electrical conductivity of the plasma. The current $\boldsymbol{j}$ is related to the magnetic fields by Ampère's law:

$$\nabla \times \boldsymbol{B} = \frac{4\pi}{c}\boldsymbol{j} \tag{1.5}$$

where we have neglected the displacement current: $(1/c)\partial_t E$.

Substituting equation (1.4) into Faraday's equation:

$$\frac{\partial \boldsymbol{B}}{\partial t} = -c \nabla \times \boldsymbol{E} \tag{1.6}$$

we can obtain the induction equation which gives the evolution of the magnetic field:

$$\frac{\partial \boldsymbol{B}}{\partial t} = \nabla \times (\boldsymbol{v} \times \boldsymbol{B}) + \frac{c^2}{4\pi\sigma}\nabla^2 \boldsymbol{B} \ . \tag{1.7}$$

The set of equations is completed with the solenoidal condition for the magnetic field: $\nabla \cdot \boldsymbol{B} = 0$. Equation (1.7) is known as the *induction equation.* The first term on the right hand side describes the advection of field lines by the fluid, while the second term is the diffusive term.

The ratio of these terms for a typical length scale L and a velocity scale v is the magnetic Reynolds number:

$$R_m = \frac{L\,v}{\eta} \ , \tag{1.8}$$

with $\eta = c^2/(4\pi\sigma)$ the magnetic diffusivity.

The fact that equation (1.7) is highly non-linear makes it difficult to extract immediate consequences for the behavior of the magnetic field; nevertheless, some conclusions may be derived when studying two extreme cases: $R_m \gg 1$ and $R_m \ll 1$. In the case of a high conductivity fluid ($\sigma \to \infty$), there is no diffusion and the induction equation takes the form:

$$\frac{\partial \boldsymbol{B}}{\partial t} = \nabla \times (\boldsymbol{v} \times \boldsymbol{B}) \ . \tag{1.9}$$

Equation (1.9) expresses the conservation of the magnetic flux that goes through any closed curve that moves with velocity $\boldsymbol{v}$ [Priest, 1982]. Thus, the magnetic field moves with the fluid. This result is the magnetic analogy of the Kelvin's theorem of vorticity, which states that, for an inviscid flow, vortex lines move with the fluid. If $R_m \ll 1$ then the advective term is negligible and the induction equation becomes a diffusion equation. In this case the typical timescale for the diffusion of magnetic field is:

$$\tau_d = \frac{4\pi\sigma L^2}{c^2} = \frac{L^2}{\eta} \ . \tag{1.10}$$

To explore this deeply let's consider the simple case presented by [Priest & Forbes, 2000]. For a one-dimensional magnetic field $B(x,t)\hat{\mathbf{y}}$ satisfying:

$$\frac{\partial B}{\partial t} = \eta \frac{\partial^2 B}{\partial x^2} \tag{1.11}$$

the solution for this equation is:

$$B(x,t) = \int G(x-x',t)B(x',0)dx' \tag{1.12}$$

where $B(x,0)$ is some initial condition and G is the Green function:

$$G(x-x',t) = \frac{1}{\sqrt{4\,\pi\,\eta\,t}} \exp\left[\frac{-(x-x')^2}{4\eta\,t}\right] . \tag{1.13}$$

If we assume that initially we have an infinitesimally thin current sheet as shown in figure 1.8: $B = B_0$ for $x > 0$ and $B = -B_0$ for $x < 0$. We expect that the steep magnetic gradient will spread out as the magnetic field evolves in time. The solution of equation (1.11) can be written in terms of the error function:

$$B(x,t) = \frac{2\,B_0}{\sqrt{\pi}} erf\left(\frac{x}{\sqrt{4\,\eta\,t}}\right) = \frac{2\,B_0}{\sqrt{\pi}} \int_0^{x/\sqrt{4\eta t}} e^{-u^2}\,du\ . \tag{1.14}$$

According to this expression, the magnetic field diffuses away in time at a speed η/l where l is the width of the sheet and is of the order of $\sqrt{\eta\,t}$. The resulting magnetic field strength at a fixed value of x decreases with time so the field is annihilated as we show in figure 1.9.

It is worth calculating the evolution of magnetic energy:

$$\frac{\partial}{\partial t} \int_{-\infty}^{\infty} \frac{B^2}{8\,\pi}\,dx = \int_{-\infty}^{\infty} \frac{B}{4\,\pi} \frac{\partial B}{\partial t}\,dx \tag{1.15}$$

substituting then expression for $\frac{\partial B}{\partial t}$ with equation (1.11) and integrating by parts we find:

$$\int_{-\infty}^{\infty} \frac{c\,B\,\eta}{4\,\pi} \frac{\partial^2 B}{\partial x^2} = \frac{c^2}{(4\,\pi)^2\,\sigma} \left\{ \left[B \frac{\partial B}{\partial x} \right]_{-\infty}^{\infty} - \int_{-\infty}^{\infty} \left(\frac{\partial B}{\partial x} \right)^2 dx \right\} . \tag{1.16}$$

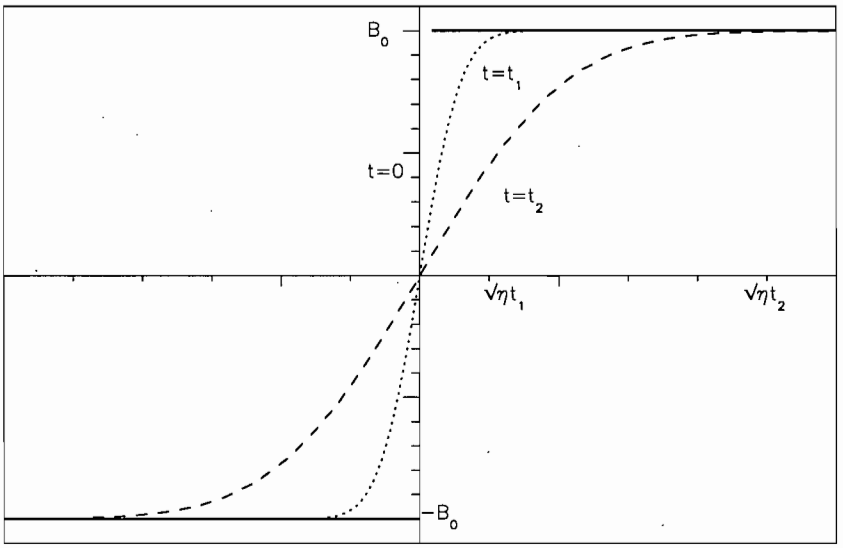

Figure 1.8: The magnetic field as a function of distance in a one-dimensional sheet that is diffusing from one of initially zero thickness. Three different consecutive times are plotted ($t = 0$, $t = t_1$ and $t = t_2$).

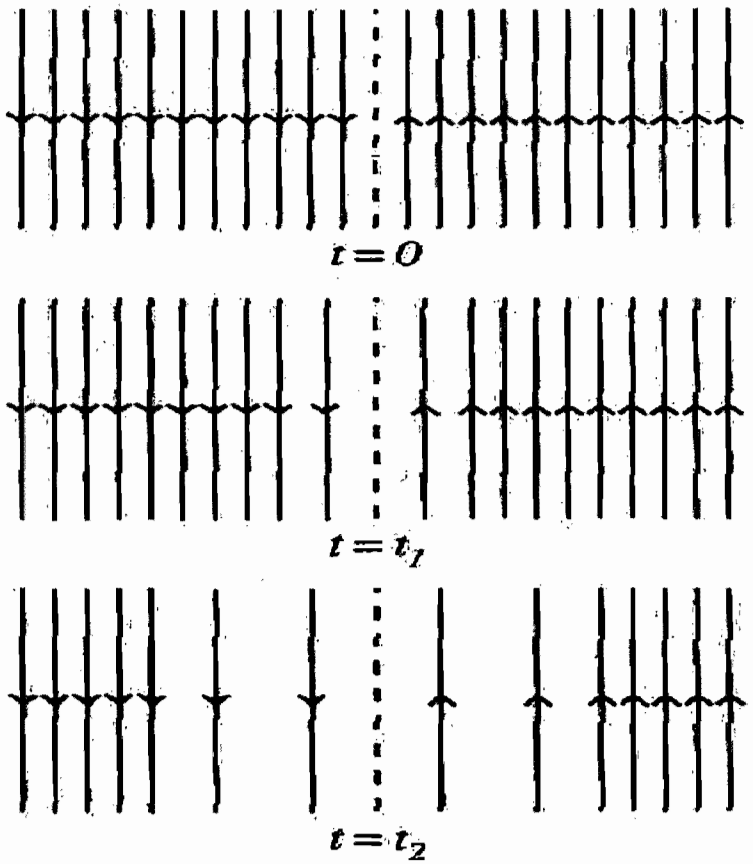

Figure 1.9: Annihilation of magnetic field lines (Figure 3.2 in [Priest & Forbes, 2000]).

The first term on the right side vanished because $\frac{\partial B}{\partial x} = 0$ at infinity and, remembering that for this example the current is $j = \frac{c}{4\pi}\frac{\partial B}{\partial x}$, we obtain:

$$\frac{\partial}{\partial t}\int_{-\infty}^{\infty} B = -\int \frac{j^2}{\sigma}\, dx \; ; \tag{1.17}$$

this means that all the magnetic energy is transformed into heat by ohmic dissipation. Under normal coronal conditions the dissipation timescale τ_d is of the order or 10^{10-16} sec which is many orders of magnitude longer than the onset and thermalization times for flares. The former is typically $1-2$ sec and the latter is of the order of 100 sec (as shown in figure 1.5).

Magnetic reconnection is the most plausible mechanism to obtain timescales in accordance with the rapid release of energy in the solar corona. The following section is devoted to a presentation of the basic theory regarding this process.

1.4 Magnetic Reconnection

Magnetic reconnection is a fundamental physical process occurring in a magnetized plasma and is probably the most promising one for explaining large-scale, dynamic releases of magnetic energy. During the reconnection process, magnetic field lines break and rearrange in a lower energy state. The excess magnetic energy is converted into kinetic energy and heat, and large electric currents and electric field are created. Figure 1.10 shows a simple scheme of the reconnection process: magnetic field lines of opposite polarities are brought together. As this takes place the value of the magnetic gradient in the central region increases and produces a strong current along a diffusion region called *current sheet* and perpendicular to the field lines. Within this region field lines are broken and reconnected producing a new magnetic topology. This process may go on as fresh magnetic fields are brought into the diffusion region.

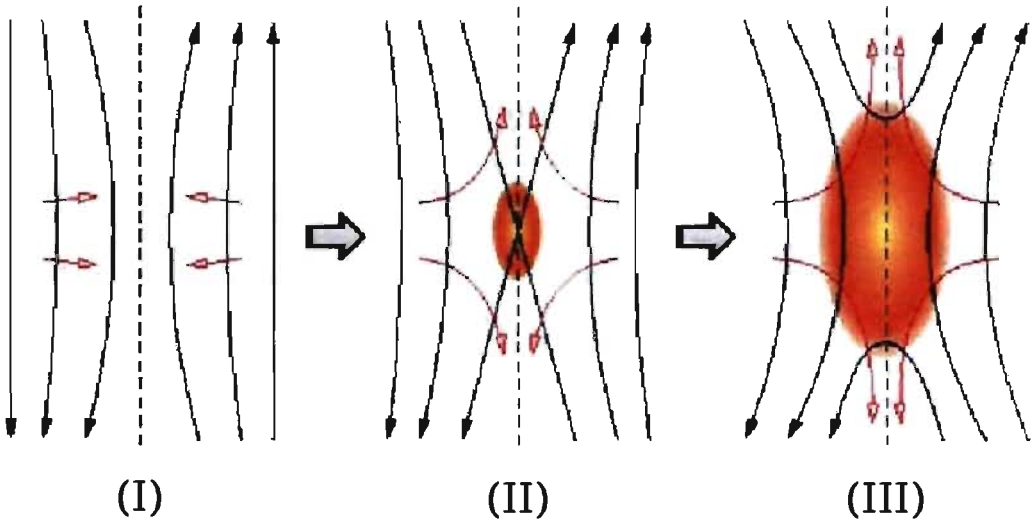

Figure 1.10: Three stages in the reconnection process. (I) Driven field lines approaching. (II) A diffusion region is formed. A strong current perpendicular to the plane of the paper appears. Field lines broke and reconnect. (III) New connectivity between field lines. Magnetic energy is converted into kinetic and thermal energy http://www.aldebaran.cz/astrofyzika/plazma/reconnection/.

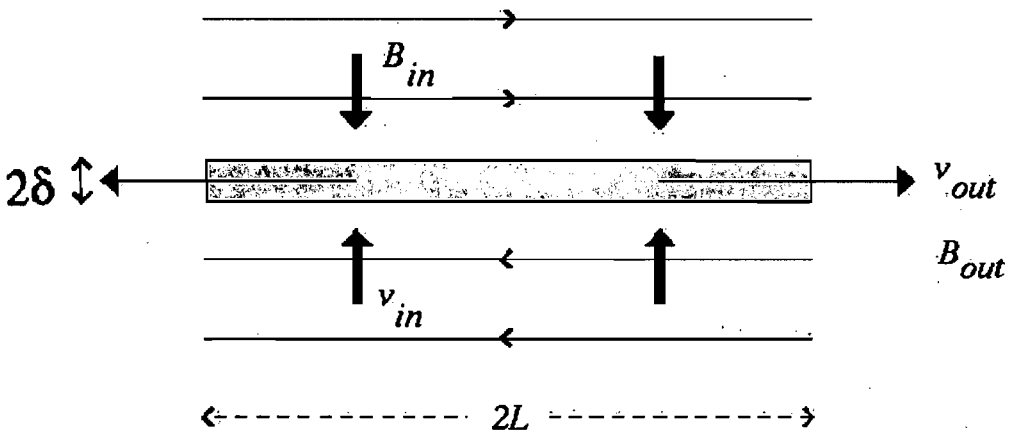

Figure 1.11: Sweet-Parker model. The diffusion region is shaded. Plasma velocity is indicated by thick-headed arrows and the magnetic field lines by thin-headed arrows (Figure 4.2 in [Priest & Forbes, 2000])

One of the most important questions to decide if reconnection is or is not the mechanism responsible of energy release in solar flares has to do with the typical timescales dominating the process. To begin this discussion we present the simplest model of magnetic reconnection.

1.4.1 Sweet-Parker Mechanism

The Sweet-Parker model assumes that reconnection takes place in a thin region known as *the diffusion region.* The main goal of this model is to describe the magnetized fluid by means of the the magnetohydrodynamic equations (MHD) and to estimate the value of each term in the steady state in order to obtain the typical rate of reconnection of magnetic field lines.

In a 2D-steady state the electric field is uniform within the difussion region, so Ohm's law takes the form:

$$E \propto \frac{1}{\sigma} j \ . \tag{1.18}$$

Outside this region the current is zero so:

$$E \propto \frac{v_{in} B_{in}}{c} \ , \tag{1.19}$$

where v_{in} and B_{in} are the velocity and magnetic fields entering the diffusion region. In this system Ampère's law takes the form:

$$j \propto \frac{B_{in}}{\delta} \ . \tag{1.20}$$

Eliminating E between equations (1.18) and (1.19) and combining the result with equation (1.20) we can obtain the velocity at the entrance of the diffusion zone as a function of the width of the current sheet:

$$v_{in} \propto \frac{\eta}{\delta} \ . \tag{1.21}$$

Assuming that the reconnection of lines is steady then conservation of mass implies that the rate at which the mass is entering the sheet is the same as the going-out rate, so that:

$$L\, v_{in} \propto \delta\, v_{out} \ , \tag{1.22}$$

where L is the length of the diffusion zone (see figure 1.11). Eliminating the width (δ) using equation (1.21) and (1.22) we obtain:

$$v_{in}^2 \propto \eta \frac{v_{out}}{L} \ , \tag{1.23}$$

and the flux conservation condition gives:

$$L\,B_{in} \propto \delta\,B_{out}\ . \tag{1.24}$$

The relation between the velocity and the magnetic fields can be obtained combining equations (1.23) and (1.24):

$$v_{in}\,B_{in} \propto v_{out}\,B_{out}\ , \tag{1.25}$$

and with this relation we can estimate the value of the current $j \sim B_{in}/\delta$ so that Lorentz's force along the current sheet is:

$$(\boldsymbol{j} \times \boldsymbol{B})_x \propto j\,B_{out} \propto \frac{B_{in}B_{out}}{\delta}\ . \tag{1.26}$$

This force accelerates the plasma from rest at the neutral point to v_{out}. Replacing this into "Navier-Stokes" equation we have:

$$\frac{\rho\,v_{out}^2}{L} \propto \frac{B_{in}B_{out}}{4\pi\delta}\ , \tag{1.27}$$

Eliminating B_{out} with equation (1.25) and (1.27) we obtain:

$$v_{out} \propto \frac{B_{in}}{\sqrt{4\pi\rho}} = v_a \tag{1.28}$$

where v_a is the Alfvén's speed. Thus the magnetic force accelerates the plasma to the Alfvén's speed.

The dimensionless reconnection rate (M) is defined as the ratio between the incoming and the outgoing flux:

$$M = \frac{v_{in}}{v_{out}}\ . \tag{1.29}$$

Considering equation (1.29) as the reconnection rate has led to some confusion, since properly speaking the reconnection rate is the rate of flux change at the neutral point but in steady conditions M is conventionally used as a measure of the reconnection rate. Dividing the square root of equation (1.23) by v_{out} (which is equal to v_a by equation (1.28)) we can obtain an expression for the reconnection rate:

$$M = \sqrt{\frac{\eta}{L\, v_a}} = \frac{1}{\sqrt{R_m}}\,, \tag{1.30}$$

where R_m is the Reynolds magnetic number, that can be written in terms of the magnetic diffusivity:

$$R_m = \frac{L\, v_a}{\eta}\,. \tag{1.31}$$

In the solar outer atmosphere Reynolds magnetic number has typical values between 10^8 and 10^{14}; this yields typical reconnection timescales which are $1/\sqrt{R_m}$ smaller than dissipation timescale in the corona. The Sweet-Parker reconnection timescale is still far from eruptive flare phenomena. In an attempt to give an answer to this question in 1983 E. N. Parker proposed a collective reconnection effect occurring in the corona: *nanoflares*.

1.4.2 Coronal heating and Parker's conjecture

Regardless of the many open questions that magnetic reconnection theory still poses, there is no doubt that, when reconnection occurs, most of the energy liberated by the process ends up heating the plasma surrounding the flaring site as the charged particles, accelerated by the electrical field produced during reconnection, thermalize with the surrounding cooler plasma.

Given the flare frequency distribution $f(E)$ (see equation (3.1)), the total energy per unit time released collectively by an ensemble of solar flares is:

$$\frac{dE_T}{dt} = \int_{E_{min}}^{E_{max}} f(E)\, E\, dE = f_0 \left[\frac{E^{2-\alpha}}{2-\alpha} \right]_{E_{min}}^{E_{max}} \qquad \text{for } \alpha \neq 0 \ . \tag{1.32}$$

If $\alpha = 2$ the total energy is:

$$E_T \ = \ f_0 \log \left(E_{max} / E_{min} \right) \ . \tag{1.33}$$

The values of f_0 and E_{max} have already been estimated (see [van Ballegooijen, 1986]). They are insufficient to provide a total flux of the order of 10^7 erg/cm^2/s even at the solar maximum. This implies that, if the largest flares are to be responsible for coronal heating, then $\alpha < 2$; on the contrary if $\alpha > 2$, the smallest flares dominate the energy release. Parker has conjectured theoretically that these 'nanoflares' are responsible for coronal heating.

In Parker's conception the magnetic free energy is stored in the corona. Stochastic movements of the photospheric fluid do move around the footpoints of magnetic coronal loops as shown in figure 1.12. Because the coronal plasma is highly conductive the frozen-in condition for the magnetic field holds up resulting in a complex, entangled magnetic field force free almost everywhere except in many small electrical currents sheets which form spontaneously in highly-stressed regions (current sheets). As the current in these sheets goes beyond some threshold, reconnection takes place and magnetic energy is released.

If Parker's model is correct then α should be greater than two. In order to complement observational analysis a theoretical calculation of α appeared necessary. There have been attempts to solve numerically the MHD equations that describe Parker's scenario (see for example; [Galsgaard, 1996], [Mikic et al., 1989], [Longcope & Sudan, 1994]). Those simulations could not reach a parameter regime where all scales were resolved,

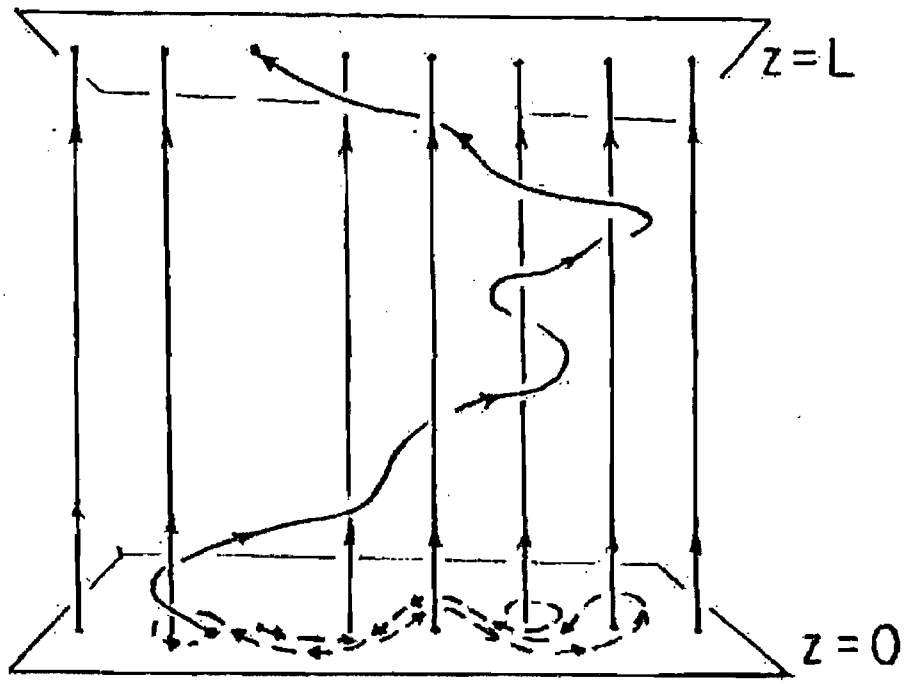

Figure 1.12: A sketch of the idealized situation of the uniform magnetic field that conforms a coronal loop. The magnetic structure has been straightened and extends between the two extremes $z = 0$ to $z = L$ located at the photosphere through the highly conducting fluid that forms the solar corona. The field is fixed at $z = L$ while the footpoint ($z = 0$) is driven randomly among its neighbors by photospheric turbulent convective motions, leading to the formation of current sheets. (extracted from Figure 11.2 in [Parker, 1979])

and thus could not obtain reliable probability distribution functions with which to estimate α. Self-organized criticality came along as a shortcut towards this goal.

1.5 Self-Organized Criticality and Flares

Self-organized criticality (SOC) has been proposed in the late eighties by Bak, Tang and Wiesenfeld [Bak, Tang & Wiesenfeld, 1988] as a general framework to understand the occurrence of power laws in nature. The basic idea of their model is that dynamical systems with many spatial degrees of freedom can, under certain circumstances, evolve into a self-organized critical state. The prototypical SOC model is the so-called sandpile model.

1.5.1 The sandpile system

Consider a circular table on which sand grains are dropped one at a time. The grains might be added at random positions or only at one point. This process can cause local disturbances but there is no obvious direct communication between grains that are far apart in the pile. Eventually, the sand dropping will lead to the buildup of a more or less conical pile as shown in figure 1.13. The sandpile steepens until its slope reaches a critical angle: *the angle of repose* beyond which further addition of sand leads to an *avalanche*, thus sand is swept down so that the slope remains close to its critical value. The addition of grains of sand has transformed the system from a state in which the individual grains follow their own local dynamics to a critical state where the emergent dynamics are global. At this point the sandpile is in a statistically stationary state, with the average rate of sand falling off the table's edge equal to the rate in which sand grains are supplied. But it is a dynamical stationary state in which relaxation is related

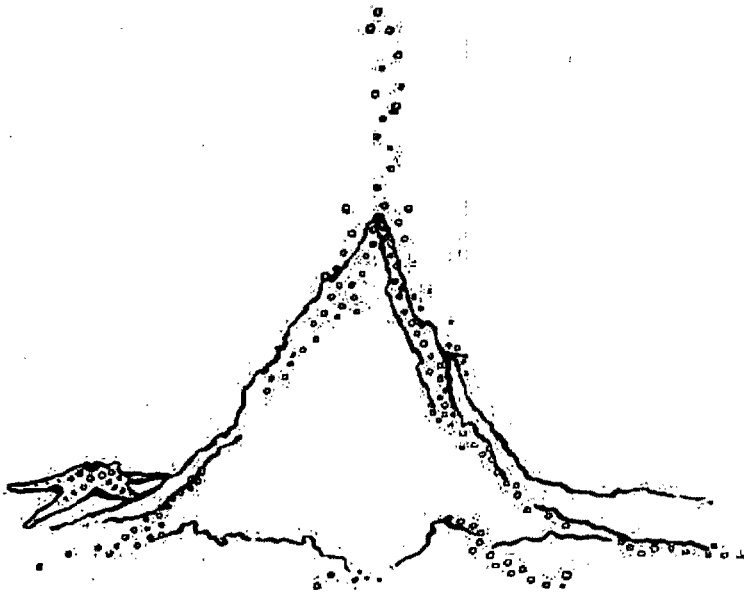

Figure 1.13: Cartoon sandpile (adapted from Figure 1 in [Bak, 1996]).

to the occurrence of occasional avalanches that may span the whole pile. This means that a newly dropped grain can affect another sand grain located anywhere throughout the pile by triggering the avalanche so the system is in a *critical state.*

The sandpile is an open dynamical system. It has many degrees of freedom: the number of grains of sand. One of those grains landing on the pile represents the addition of potential energy. When the sand moves along the slope this energy is transformed into kinetic energy. Once the grain reaches an equilibrium the kinetic energy is transformed into heat. The critical state is maintained by the external addition of sand. A typical feature of this kind of systems is that the energy input is slow and steady while the energy release is strongly intermittent. The sandpile is only an example of the critical behavior of different phenomena. In the next section we resume the main characteristics of self-organized critical systems.

1.5.2 Self-Organized Critical State

The central aspects of self-organized critical systems can be found by understanding the meaning beneath each word. A *self-organized* system naturally evolves to a state without detailed specification of the initial conditions or external control during evolution. A self-organized state is said to be *critical* when although the interaction between the elements of the system is local, the emergent property of this interaction is global. It does not matter how two elements of the system interact as long as this interaction is local and allows the definition of a threshold. It is in this sense that the critical state is said to be an *attractor* of the dynamics. Thus, if the driving rate is suddenly increased, large avalanches will appear and they will rapidly remove the surplus of sand from the system. On the other hand if one artificially removes sand from the pile, the frequency of large, boundary-discharging avalanches will go down until the angle of repose has been restored throughout the pile. Another important feature in order to obtain an interaction-dominated system is the driving rate. Strong driving will not allow the system to relax from one metastable configuration to the other. Finally, a universal characteristic of physical systems in a SOC state is that energy is dissipated in all length scales. Once the critical state is reached the system stays there and it is possible to characterize the behavior of the system by a number of critical exponents.

Self-organized criticality of interacting systems is often studied using cellular automata models. A cellular automaton (CA) consists of a discrete dynamical system with many degrees of freedom. Space, time, and the states of the system are discretized. Each element of the system evolves according some set of discrete local rules. In 1991 Lu and Hamilton [Lu & Hamilton, 1991] proposed that the solar coronal magnetic field is in a self-organized critical state and presented the first CA model for solar flares. Since then several CA for solar flares haven been proposed. Although different in many aspects all of these models share common features with Lu and Hamilton's model. For this reason we present in the next section a basic lattice model adapted

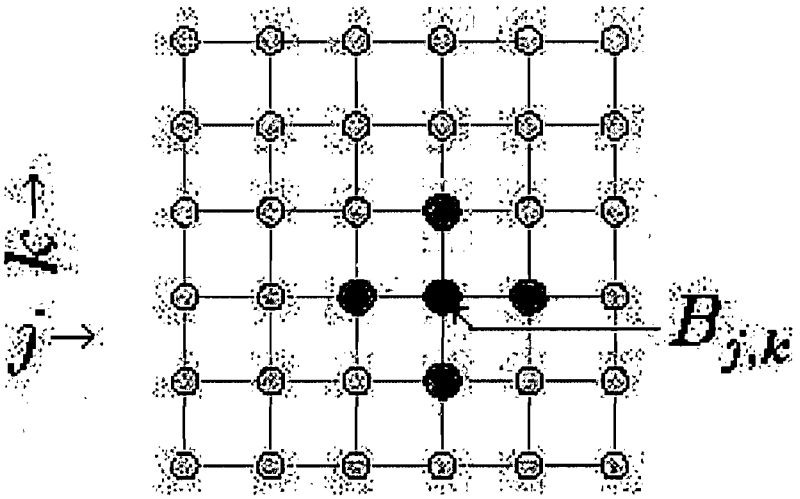

Figure 1.14: A two-dimensional regular cartesian lattice. A field quantity B is defined at each node (j, k). Four nearest neighbors are red-dotted. (see Figure 1 in [Charbonneau et al., 2001])

from [Lu et al., 1993] and examine the physical interpretations and limitations of the lattice model.

1.6 A basic lattice model

1.6.1 The lattice and the driving mechanism

On a simple regular 2D-cartesian lattice it is possible to define a physical quantity $B_{\mathbf{k}}$ on each lattice node. This quantity is and assumed to be a continuous, scalar variable (see figure 1.6.1).

In the context of solar flares $B_{\mathbf{k}}$ is interpreted as a measure of the magnetic field

and $B_{\mathbf{k}}^2$ gives the magnetic energy, so the lattice energy (E_l) is:

$$E_l = \sum_k B_{\mathbf{k}}^2 \ , \tag{1.34}$$

and the lattice mean magnetic field $< B >$ is:

$$< B >= \frac{1}{N^D} \sum_k \sum_j B_{kj} \ , \tag{1.35}$$

where N and D are the size and dimension of the lattice.

The existence of a globally stationary state requires that the physical quantity defined on the lattice be externally driven. The simplest way to do this is to add a succession of perturbations δB at randomly selected interior nodes. This occurs only when the system is not avalanching. In order to ensure a SOC state to be attained the driving must be weak and the relation between δB and $< B >$ should be:

$$\frac{|\delta B|}{< B >} \ll 1 \ . \tag{1.36}$$

Once the perturbation process has started each node has to be tested for stability.

1.6.2 The stability criterion

The stability criterion is based on the curvature of the magnetic field (ΔB), defined as:

$$\Delta B = B_{\mathbf{k}} - \frac{1}{2\,D} \sum_{nn=1} B_{\mathbf{k}} \ , \tag{1.37}$$

where the sum runs over the two-dimensional nearest neighbors "n, n" on the lattice. The configuration is defined to be unstable when $|\Delta B| > B_c$. B_c is a critical value that must remain non-zero. The idea of measuring the curvature of the magnetic field was originally developed by Lu & Hamilton [Lu & Hamilton, 1991]. Up to that point most models used a height-triggered or slope-based stability criteria.

In Lu & Hamilton's conception, ΔB is a gradient but actually it has the form of a second-order centered finite difference expression for a D-dimensional Laplacian operator as shown in [Galsgaard, 1996]. All models with this kind of stability criterion are referred to in the literature as 'curvature-triggered' systems.

1.6.3 The redistribution rule

If ΔB exceeds the critical value some action is needed to restore stability. A natural procedure is to decrease B at the unstable node and distribute the excess at neighboring nodes. So the new magnetic field at the unstable node is:

$$B_{\mathbf{k}} \rightarrow B_{\mathbf{k}} - \frac{2\,D}{2\,D+1} B_c \ , \tag{1.38}$$

and at the neighboring nodes is:

$$B_{nn} \rightarrow B_{nn} + \frac{2\,D}{2\,D+1} B_c \ . \tag{1.39}$$

After the redistribution has been applied as prescribed by equation (1.39), it is possible that one or more nearest-neighbor nodes might have become also unstable; if this is the case, the redistribution rule is to be applied on those nodes and so on until stability is restored everywhere. The redistribution rule presented in (1.39) is locally conservative, meaning that $B_{\mathbf{k}} + \sum B_{nn}$ remains constant but the total energy of the lattice is reduced. The discrete energy lost is:

$$e_r = \frac{2\,D}{2\,D+1} (2 \frac{|\Delta B|}{B_c} - 1) B_c^2 \ . \tag{1.40}$$

From this expression one can deduce that the smallest energy that can be released by a single node that has infinitesimally exceeded the threshold value B_c is:

$$e_0 = \frac{2\,D}{2\,D+1} B_c^2 \ . \tag{1.41}$$

In Lu & Hamilton's conception, ΔB is a gradient but actually it has the form of a second-order centered finite difference expression for a D-dimensional Laplacian operator as shown in [Galsgaard, 1996]. All models with this kind of stability criterion are referred to in the literature as 'curvature-triggered' systems.

1.6.3 The redistribution rule

If ΔB exceeds the critical value some action is needed to restore stability. A natural procedure is to decrease B at the unstable node and distribute the excess at neighboring nodes. So the new magnetic field at the unstable node is:

$$B_{\mathbf{k}} \rightarrow B_{\mathbf{k}} - \frac{2\,D}{2\,D+1} B_c \,, \tag{1.38}$$

and at the neighboring nodes is:

$$B_{nn} \rightarrow B_{nn} + \frac{2\,D}{2\,D+1} B_c \,. \tag{1.39}$$

After the redistribution has been applied as prescribed by equation (1.39), it is possible that one or more nearest-neighbor nodes might have become also unstable; if this is the case, the redistribution rule is to be applied on those nodes and so on until stability is restored everywhere. The redistribution rule presented in (1.39) is locally conservative, meaning that $B_{\mathbf{k}} + \sum B_{nn}$ remains constant but the total energy of the lattice is reduced. The discrete energy lost is:

$$e_r = \frac{2\,D}{2\,D+1} (2\frac{|\Delta B|}{B_c} - 1) B_c^2 \,. \tag{1.40}$$

From this expression one can deduce that the smallest energy that can be released by a single node that has infinitesimally exceeded the threshold value B_c is:

$$e_0 = \frac{2\,D}{2\,D+1} B_c^2 \,. \tag{1.41}$$

The total energy release after one iteration will be:

$$E_r = \sum e_r \ , \tag{1.42}$$

with the sum extending over all the nodes that have been unstable during the corresponding iteration. Regardless the details of the energy input method all SOC models of solar flares have one important thing in common: energy injection is slow and steady whereas energy release is strongly intermittent, mimicking in this way the classical sandpile.

Since 1991, many SOC models for solar flares have been constructed using different kind of lattices, varying the stability criteria or the redistribution rule. Many of them have successfully calculated power-law indices that remain close the one observed in solar flares. In table (1.4) we show (just as an example) some of the power-law indices obtained for total energy for several SOC models available in the literature. Slight differences between the models are related to the different manners each group went about carrying out the fits. From table (1.4) we note that there are not great differences between $2\,D$ and $3\,D$ models and the α indices fall nicely within the ranges set by the observational inferences (see table (1.3)).

1.7 Physical Interpretation

Up to this point we have described all the elements that are included in most classical SOC models for solar flares. Now we head forward to discuss the physical meaning of each of those elements.

The most straightforward physical association of the nodal field $B_{\mathbf{k}}$ is to the magnetic field $\mathbf{B}$, in which case equation (1.35) for lattice energy makes sense. However in general this leads to $\nabla \cdot \mathbf{B} \neq 0$. Associating $B_{\mathbf{k}}$ with a vector potential $\mathbf{A}$ such that $\boldsymbol{B} = \nabla \times \mathbf{A}$

Reference	*Geometric Model* $N^D(*)$	α_E
Lu et al. 1993	50^3	1.51
Lu & Hamilton 1991	30^3	1.4
Charbonneau et al 2001	1024^2	1.421
	128^3	1.485
Longcope & Noonan	300^2	1.34
Zirker & Cleveland	32^2	1.45

Table 1.4: Power-law indices for total energy (E).
(*) N is the size of the lattice and D is the dimensionality of the model.

solves the problem of the conservation of the magnetic flux but also offers a plausible interpretation of the driving process. Adding an increment $\delta\mathbf{A}$ to the lattice can be thought of as a twisting of the magnetic field. The problem with this interpretation is that $\sum B_{\mathbf{k}}^2$ is no longer a measure of the magnetic energy and jeopardizes the whole idea of comparing model time series to flare observations. The re-interpretation of $B_{\mathbf{k}}$ as the vector potential provides a physically meaningful interpretation for the instability threshold. It can be noted here that equation (1.37) has the form of a finite difference expression for the Laplacian operator, so the threshold condition implies that magnetic reconnection takes place when $\nabla^2\mathbf{A}$ exceeds certain value.

Remembering that $\mathbf{B} = \nabla \times \mathbf{A}$, Ampère's law (equation 1.5) takes the form:

$$\boldsymbol{j} = \frac{c}{4\pi}\nabla \times (\nabla \times \mathbf{A}) = \frac{\mathbf{c}}{4\pi}[-\nabla^2\mathbf{A} + \nabla(\nabla \cdot \mathbf{A})] \; . \tag{1.43}$$

Using the Coulomb Gauge ($\nabla \cdot \mathbf{A} = \mathbf{0}$), equation (1.43) leads us to:

$$|\boldsymbol{j}| \propto |\nabla^2\mathbf{A}| \; . \tag{1.44}$$

Thus, the threshold condition implies that reconnection takes place when the local electric current exceeds a certain value which is physically interesting for reconnection-triggering plasma instabilities.

In 2000 Isliker and collaborators [Isliker, Anastasiadis & Vlahos, 2000] argued that $B_{\mathbf{k}}$ should be identified with a smooth vector potential and interpreted the redistribution rule in terms of the current dissipation. They also show that the frequency distribution of events sizes constructed using measures of current dissipation does not differ significantly from those arising from the traditional $B_{\mathbf{k}} \rightarrow B$ identification ([Isliker, Anastasiadis & Vlahos, 2000]). Also in 2000 Longcope and Noonan [Longcope & Noonan, 2000] constructed a 2D model where the dynamical elements are currents flowing along separatrix surfaces. This is produced by shearing the currents in the plane of the lattice so the threshold and the redistribution rule are easily related to these currents. They also obtained power-law distributions of events sizes with indices close to those of classical SOC models.

SOC models were successful in reproducing the power-law form of some flare parameters and to yield to slopes that are in good agreement with observations. There is still a remaining problem in order to give a full physical interpretation to each of its elements. In chapter 2 we propose a new SOC model closer to the physical picture underlying Parker's hypothesis.

1.8 Scaling laws and avalanches

Calculation of the so-called avalanche exponents is common practice when working in the context of solar flares. Nevertheless, the determination of the geometrical properties of avalanches has been little explored [McIntosh et al., 2002] and the connections between avalanche exponents and spreading exponents has only been established for

the case of general systems with absorbing states [Muñoz et al., 1999] or for the case of the Earth-magnetosphere [Uritsky et al., 2001] but has not yet been developed for the analysis of flare data or flare numerical models. We introduce here the main vocabulary and properties related to this way of characterizing avalanches as we have performed in this thesis a complete study of avalanche exponents.

1.8.1 Geometrical properties of avalanches

We start with the simplest geometrical property of the avalanches produced by SOC models namely the area of avalanches. We consider the following two related measures of avalanches area: the total number of lattice nodes having avalanched (that is being unstable) at least once during the course of a given avalanche, A^*; and the total number of unstable nodes at the time of peak energy release, A. Figure 1.8.1 (A) shows a snapshot of an avalanche at the peak if its energy release, extracted from a simulation performed by [Charbonneau et al., 2001] (in this case 329 nodes had been unstable) while figure 1.8.1 (B) shows a time-integrated avalanche where $\sim$ 4200 nodes had gone unstable.

1.8.2 Fractal dimensions

Another way of characterizing avalanches is using their fractal dimension D. Essentially, two different ways of calculating D have been usually applied: one is based on the calculation of the area/volume or radius/area relationship while the other is based on the so-called box-counting methods.

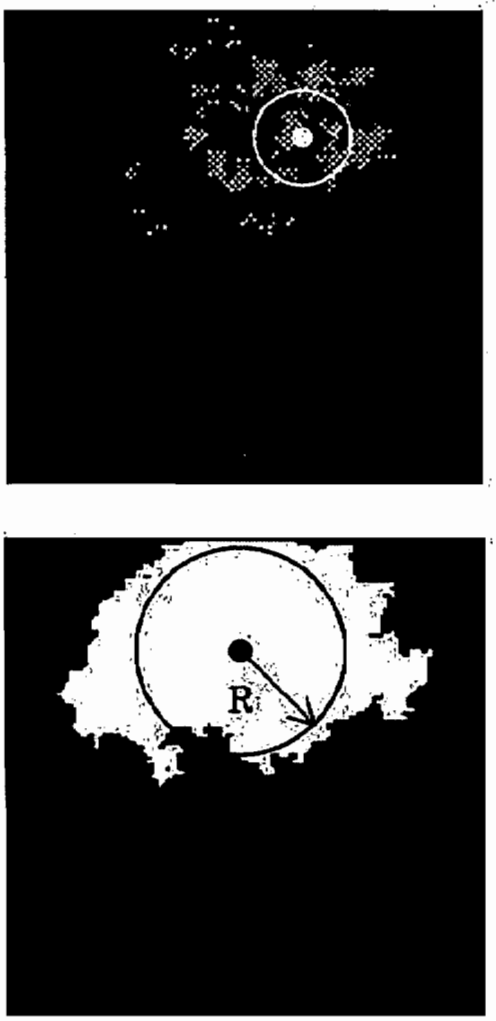

Figure 1.15: The spatial structure of an avalanche in a 128×128 lattice. (A) shows the avalanche at its peak and (B) shows the time-integrated avalanche. (adapted from Figure 5 in [Charbonneau et al., 2001])

Let $\mathbf{r}_i$ be the position of the i-th avalanching node, measured from some arbitrary but fixed reference point in the lattice. The center of mass $\mathbf{R_0}$ and radius of gyration (R) of the cluster of avalanching nodes are given by:

$$\mathbf{R_0} = \frac{1}{V}\sum_{i=1}^{V}\mathbf{r}_i \,, \tag{1.45}$$

$$\mathbf{R^2} = \frac{1}{V}\sum_{i=1}^{V}|\mathbf{r}_i - \mathbf{r}_0|^2 \,, \tag{1.46}$$

where V is the volume of the ensemble of avalanching nodes. The radius of gyration is generally used as a way of estimating the linear size of cluster. It is nothing more than the radius of the disk having the same 'mass' and moment of inertia as the original cluster. So the fractal dimension γ_{VR} is the logarithmic slope in equation (1.47):

$$\log_{10}(V/V_0) = \gamma_{VR}\log_{10} R \,. \tag{1.47}$$

As for the geometrical properties one can obtain the fractal dimension for two different situations: the peak fractal dimension (γ_{VR}) and the time-integrated fractal dimension (γ^*_{VR}) that can be calculated using figures 1.8.1 (A) and (B) respectively.

For the classical SOC model for solar flares, [McIntosh et al., 2002] performed an extensive study of the avalanches properties. They calculated the geometrical properties as well as the fractal dimensions. In table 1.5 we present their results since we will compare our results against theirs in the upcoming chapters. Another way of estimating the fractal dimension of a given structure involves the box-counting methods. These kind of methods are commonly used to establish D from observational data ([Aschwanden & Aschwanden, 2008] and references therein). As an example we reproduce in figure 1.16 one of the recent results obtained by [Aschwanden & Aschwanden, 2008] for one of the most intense flare ever detected.

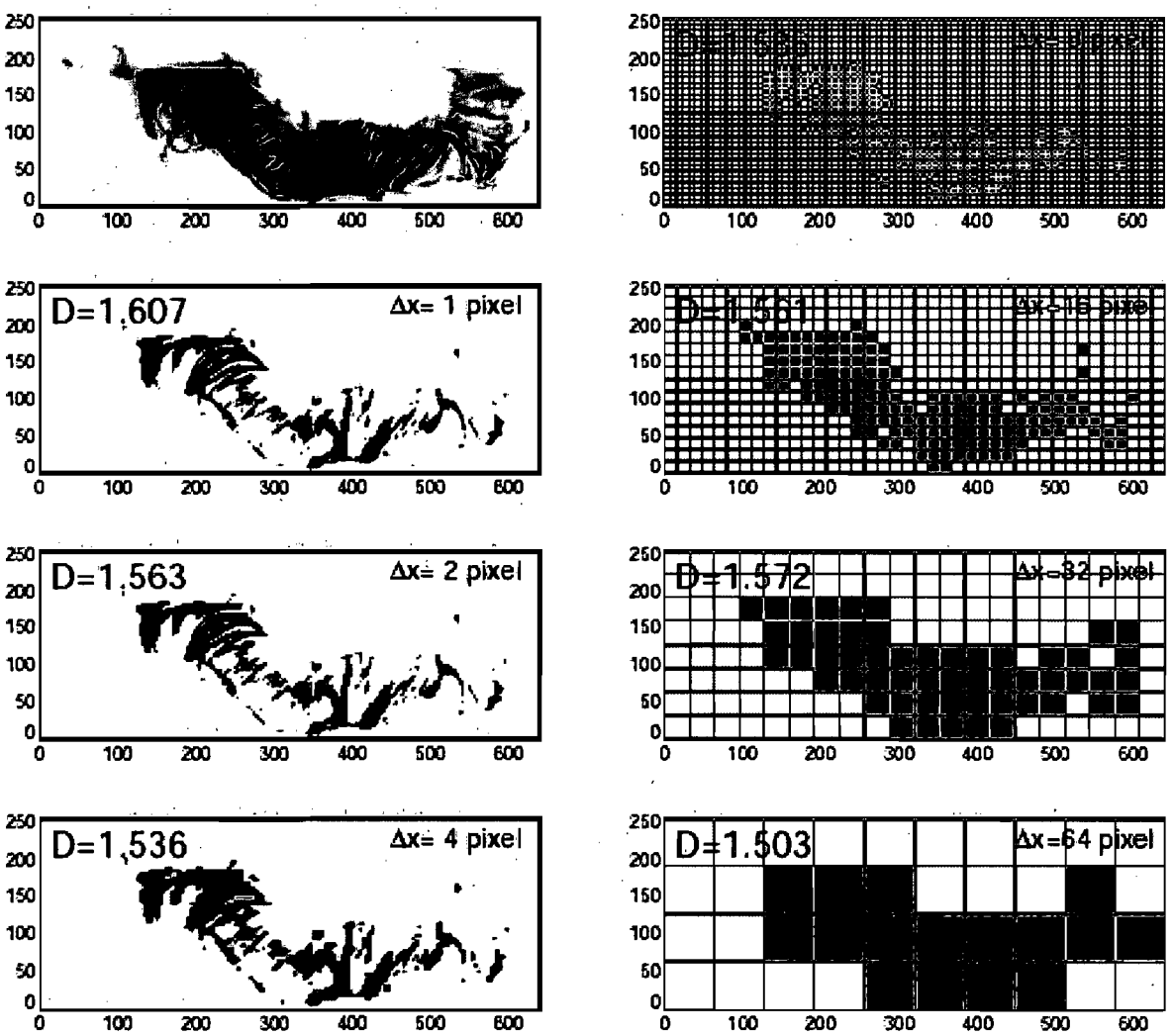

Figure 1.16: Measurement of the fractal area of the Bastille-Day flare observed on July 14th, 2000 by TRACE 171 $\AA$ (taken from Figure 1 of [Aschwanden & Aschwanden, 2008])

N^D	γ_{VR}	γ^*_{VR}	α_A	α^*_A
32^2	1.61 ± 0.02	2.01 ± 0.04	n/a	n/a
128^2	1.57 ± 0.03	2.01 ± 0.03	n/a	n/a
256^2	1.56 ± 0.04	2.00 ± 0.004	n/a	n/a
32^3	1.80 ± 0.03	2.98 ± 0.02	1.15 ± 0.04	0.62 ± 0.03
48^3	1.78 ± 0.03	2.98 ± 0.03	1.20 ± 0.04	0.63 ± 0.03
64^3	1.79 ± 0.02	2.98 ± 0.03	1.12 ± 0.05	0.63 ± 0.03
EUV 171 A			2.45 ± 0.09	
EUV 195 A			2.16 ± 0.18	

Table 1.5: Power-law indices for correlations plots as calculated from numerical simulations in [McIntosh et al., 2002] and calculated from observation by [Aschwanden & Aschwanden, 2008].

Since in the last chapter of this thesis we calculated the fractal dimension of avalanche clusters using this method we show here a classical example to illustrate how the fractal dimension can be estimated.

If we want to calculate the fractal dimension D of a given surface we can begin by covering that surface with a regular square of side 1. Then, it is always possible to divide the big square using an evenly spaced squared grid of side δ so that the total surface of the square is:

$$1 \propto N(\delta)\delta^D \ , \tag{1.48}$$

where $N(\delta)$ is the number of segments (for a full development of this formula see chapter 4). From equation (1.48) it can be easily derived that:

$$D \propto \frac{\log(N(\delta))}{\log(1/\delta)} \tag{1.49}$$

The fact that D remains constant when changing the value of δ is a clear indication that the aforementioned surface has a fractal structure.

In figure 1.8.2 we show a typical fractal structure, the so-called *Box Fractal* and covered it with squares of two different side length: $\delta = 1/3$ and $\delta = 1/9$. Applying equation (1.49) for both values of δ we obtained $D = 1.46$ thus showing clearly that we were dealing with a fractal structure. This result may seem obvious but the procedure followed here is the standard one when trying to know if a structure is a fractal one and, if that is the case, what its fractal dimension D is. In the publication presented in chapter 4 we used extensively this procedure to estimate the fractal dimensions of the avalanches produced by the SOC model of solar flares.

1.8.3 Spreading exponents

Spreading exponens are usually determined when studying avalanching systems. Compared to the avalanche statistics, spreading exponent analysis provides a more accurate and unambiguous determination of the critical point in an avalanching system.

In order to characterize spreading systems, it is customary to take several measurements: $n(t)$ is the number of avalanching sites at a specific time t and $P(t)$ measures the probability of having an ongoing avalanche at a time t. In particular, in the vicinity of the critical state, these magnitudes take the form of a power law and scale as:

$$n(t) \sim t^{\eta} \,, \tag{1.50}$$

$$P(t) \sim t^{-\delta} \,, \tag{1.51}$$

In Lu & Hamilton's conception, ΔB is a gradient but actually it has the form of a second-order centered finite difference expression for a D-dimensional Laplacian operator as shown in [Galsgaard, 1996]. All models with this kind of stability criterion are referred to in the literature as 'curvature-triggered' systems.

1.6.3 The redistribution rule

If ΔB exceeds the critical value some action is needed to restore stability. A natural procedure is to decrease B at the unstable node and distribute the excess at neighboring nodes. So the new magnetic field at the unstable node is:

$$B_{\mathbf{k}} \rightarrow B_{\mathbf{k}} - \frac{2\,D}{2\,D+1} B_c \,, \tag{1.38}$$

and at the neighboring nodes is:

$$B_{nn} \rightarrow B_{nn} + \frac{2\,D}{2\,D+1} B_c \,. \tag{1.39}$$

After the redistribution has been applied as prescribed by equation (1.39), it is possible that one or more nearest-neighbor nodes might have become also unstable; if this is the case, the redistribution rule is to be applied on those nodes and so on until stability is restored everywhere. The redistribution rule presented in (1.39) is locally conservative, meaning that $B_{\mathbf{k}} + \sum B_{nn}$ remains constant but the total energy of the lattice is reduced. The discrete energy lost is:

$$e_r = \frac{2\,D}{2\,D+1} (2 \frac{|\Delta B|}{B_c} - 1) B_c^2 \,. \tag{1.40}$$

From this expression one can deduce that the smallest energy that can be released by a single node that has infinitesimally exceeded the threshold value B_c is:

$$e_0 = \frac{2\,D}{2\,D+1} B_c^2 \,. \tag{1.41}$$

The total energy release after one iteration will be:

$$E_r = \sum e_r \ , \tag{1.42}$$

with the sum extending over all the nodes that have been unstable during the corresponding iteration. Regardless the details of the energy input method all SOC models of solar flares have one important thing in common: energy injection is slow and steady whereas energy release is strongly intermittent, mimicking in this way the classical sandpile.

Since 1991, many SOC models for solar flares have been constructed using different kind of lattices, varying the stability criteria or the redistribution rule. Many of them have successfully calculated power-law indices that remain close the one observed in solar flares. In table (1.4) we show (just as an example) some of the power-law indices obtained for total energy for several SOC models available in the literature. Slight differences between the models are related to the different manners each group went about carrying out the fits. From table (1.4) we note that there are not great differences between $2\,D$ and $3\,D$ models and the α indices fall nicely within the ranges set by the observational inferences (see table (1.3)).

1.7 Physical Interpretation

Up to this point we have described all the elements that are included in most classical SOC models for solar flares. Now we head forward to discuss the physical meaning of each of those elements.

The most straightforward physical association of the nodal field $B_{\mathbf{k}}$ is to the magnetic field $\mathbf{B}$, in which case equation (1.35) for lattice energy makes sense. However in general this leads to $\nabla \cdot \mathbf{B} \neq 0$. Associating $B_{\mathbf{k}}$ with a vector potential $\mathbf{A}$ such that $\boldsymbol{B} = \nabla \times \mathbf{A}$

Reference	*Geometric Model* $N^D(*)$	α_E
Lu et al. 1993	50^3	1.51
Lu & Hamilton 1991	30^3	1.4
Charbonneau et al 2001	1024^2	1.421
	128^3	1.485
Longcope & Noonan	300^2	1.34
Zirker & Cleveland	32^2	1.45

Table 1.4: Power-law indices for total energy (E).
(*) N is the size of the lattice and D is the dimensionality of the model.

solves the problem of the conservation of the magnetic flux but also offers a plausible interpretation of the driving process. Adding an increment $\delta\mathbf{A}$ to the lattice can be thought of as a twisting of the magnetic field. The problem with this interpretation is that $\sum B_{\mathbf{k}}^2$ is no longer a measure of the magnetic energy and jeopardizes the whole idea of comparing model time series to flare observations. The re-interpretation of $B_{\mathbf{k}}$ as the vector potential provides a physically meaningful interpretation for the instability threshold. It can be noted here that equation (1.37) has the form of a finite difference expression for the Laplacian operator, so the threshold condition implies that magnetic reconnection takes place when $\nabla^2\mathbf{A}$ exceeds certain value.

Remembering that $\mathbf{B} = \nabla \times \mathbf{A}$, Ampère's law (equation 1.5) takes the form:

$$\boldsymbol{j} = \frac{c}{4\pi}\nabla \times (\nabla \times \mathbf{A}) = \frac{\mathbf{c}}{4\pi}[-\nabla^2\mathbf{A} + \nabla(\nabla \cdot \mathbf{A})] \; . \tag{1.43}$$

Using the Coulomb Gauge ($\nabla \cdot \mathbf{A} = \mathbf{0}$), equation (1.43) leads us to:

$$|\boldsymbol{j}| \propto |\nabla^2\mathbf{A}| \; . \tag{1.44}$$

Thus, the threshold condition implies that reconnection takes place when the local electric current exceeds a certain value which is physically interesting for reconnection-triggering plasma instabilities.

In 2000 Isliker and collaborators [Isliker, Anastasiadis & Vlahos, 2000] argued that $B_{\mathbf{k}}$ should be identified with a smooth vector potential and interpreted the redistribution rule in terms of the current dissipation. They also show that the frequency distribution of events sizes constructed using measures of current dissipation does not differ significantly from those arising from the traditional $B_{\mathbf{k}} \rightarrow B$ identification ([Isliker, Anastasiadis & Vlahos, 2000]). Also in 2000 Longcope and Noonan [Longcope & Noonan, 2000] constructed a 2D model where the dynamical elements are currents flowing along separatrix surfaces. This is produced by shearing the currents in the plane of the lattice so the threshold and the redistribution rule are easily related to these currents. They also obtained power-law distributions of events sizes with indices close to those of classical SOC models.

SOC models were successful in reproducing the power-law form of some flare parameters and to yield to slopes that are in good agreement with observations. There is still a remaining problem in order to give a full physical interpretation to each of its elements. In chapter 2 we propose a new SOC model closer to the physical picture underlying Parker's hypothesis.

1.8 Scaling laws and avalanches

Calculation of the so-called avalanche exponents is common practice when working in the context of solar flares. Nevertheless, the determination of the geometrical properties of avalanches has been little explored [McIntosh et al., 2002] and the connections between avalanche exponents and spreading exponents has only been established for

the case of general systems with absorbing states [Muñoz et al., 1999] or for the case of the Earth-magnetosphere [Uritsky et al., 2001] but has not yet been developed for the analysis of flare data or flare numerical models. We introduce here the main vocabulary and properties related to this way of characterizing avalanches as we have performed in this thesis a complete study of avalanche exponents.

1.8.1 Geometrical properties of avalanches

We start with the simplest geometrical property of the avalanches produced by SOC models namely the area of avalanches. We consider the following two related measures of avalanches area: the total number of lattice nodes having avalanched (that is being unstable) at least once during the course of a given avalanche, A^*; and the total number of unstable nodes at the time of peak energy release, A. Figure 1.8.1 (A) shows a snapshot of an avalanche at the peak if its energy release, extracted from a simulation performed by [Charbonneau et al., 2001] (in this case 329 nodes had been unstable) while figure 1.8.1 (B) shows a time-integrated avalanche where $\sim$ 4200 nodes had gone unstable.

1.8.2 Fractal dimensions

Another way of characterizing avalanches is using their fractal dimension D. Essentially, two different ways of calculating D have been usually applied: one is based on the calculation of the area/volume or radius/area relationship while the other is based on the so-called box-counting methods.

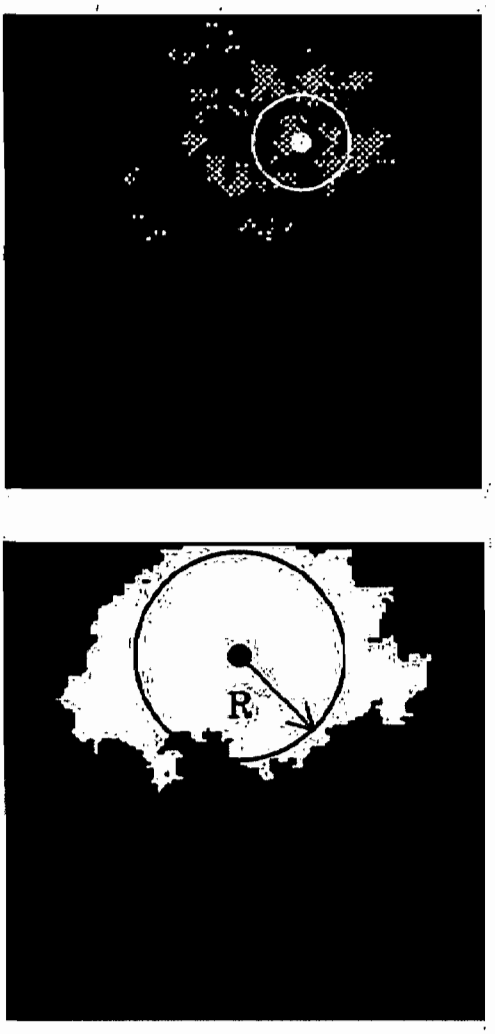

Figure 1.15: The spatial structure of an avalanche in a 128 × 128 lattice. (A) shows the avalanche at its peak and (B) shows the time-integrated avalanche. (adapted from Figure 5 in [Charbonneau et al., 2001])

Let $\mathbf{r}_i$ be the position of the i-th avalanching node, measured from some arbitrary but fixed reference point in the lattice. The center of mass $\mathbf{R_0}$ and radius of gyration (R) of the cluster of avalanching nodes are given by:

$$\mathbf{R_0} = \frac{1}{V}\sum_{i=1}^{V}\mathbf{r}_i \ , \tag{1.45}$$

$$\mathbf{R^2} = \frac{1}{V}\sum_{i=1}^{V}|\mathbf{r}_i - \mathbf{r}_0|^2 \ , \tag{1.46}$$

where V is the volume of the ensemble of avalanching nodes. The radius of gyration is generally used as a way of estimating the linear size of cluster. It is nothing more than the radius of the disk having the same 'mass' and moment of inertia as the original cluster. So the fractal dimension γ_{VR} is the logarithmic slope in equation (1.47):

$$\log_{10}(V/V_0) = \gamma_{VR}\log_{10} R \ . \tag{1.47}$$

As for the geometrical properties one can obtain the fractal dimension for two different situations: the peak fractal dimension (γ_{VR}) and the time-integrated fractal dimension (γ^*_{VR}) that can be calculated using figures 1.8.1 (A) and (B) respectively.

For the classical SOC model for solar flares, [McIntosh et al., 2002] performed an extensive study of the avalanches properties. They calculated the geometrical properties as well as the fractal dimensions. In table 1.5 we present their results since we will compare our results against theirs in the upcoming chapters. Another way of estimating the fractal dimension of a given structure involves the box-counting methods. These kind of methods are commonly used to establish D from observational data ([Aschwanden & Aschwanden, 2008] and references therein). As an example we reproduce in figure 1.16 one of the recent results obtained by [Aschwanden & Aschwanden, 2008] for one of the most intense flare ever detected.

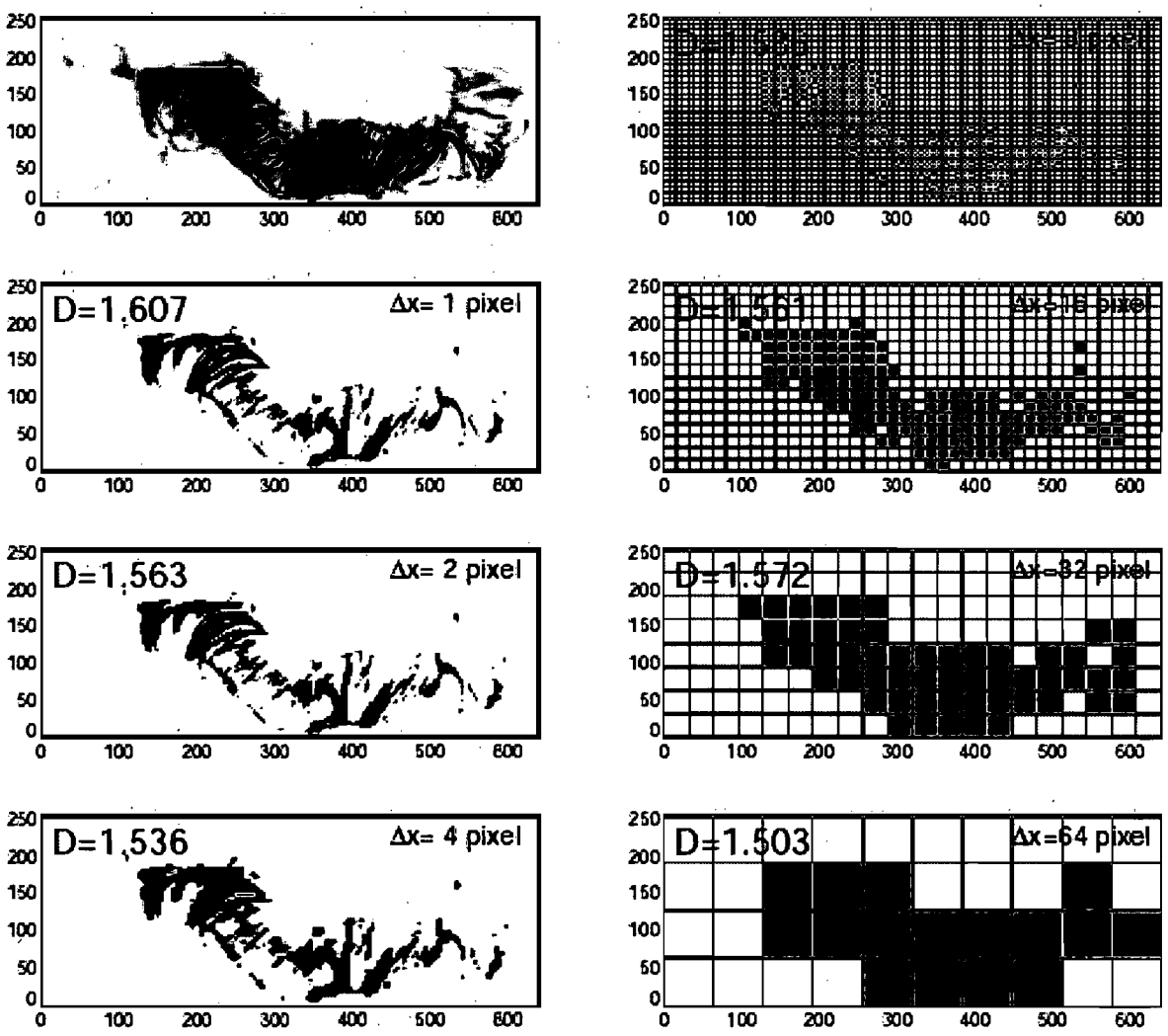

Figure 1.16: Measurement of the fractal area of the Bastille-Day flare observed on July 14th, 2000 by TRACE 171 $\AA$ (taken from Figure 1 of [Aschwanden & Aschwanden, 2008])

N^D	γ_{VR}	γ^*_{VR}	α_A	α^*_A
32^2	1.61 ± 0.02	2.01 ± 0.04	n/a	n/a
128^2	1.57 ± 0.03	2.01 ± 0.03	n/a	n/a
256^2	1.56 ± 0.04	2.00 ± 0.004	n/a	n/a
32^3	1.80 ± 0.03	2.98 ± 0.02	1.15 ± 0.04	0.62 ± 0.03
48^3	1.78 ± 0.03	2.98 ± 0.03	1.20 ± 0.04	0.63 ± 0.03
64^3	1.79 ± 0.02	2.98 ± 0.03	1.12 ± 0.05	0.63 ± 0.03
EUV 171 A			2.45 ± 0.09	
EUV 195 A			2.16 ± 0.18	

Table 1.5: Power-law indices for correlations plots as calculated from numerical simulations in [McIntosh et al., 2002] and calculated from observation by [Aschwanden & Aschwanden, 2008].

Since in the last chapter of this thesis we calculated the fractal dimension of avalanche clusters using this method we show here a classical example to illustrate how the fractal dimension can be estimated.

If we want to calculate the fractal dimension D of a given surface we can begin by covering that surface with a regular square of side 1. Then, it is always possible to divide the big square using an evenly spaced squared grid of side δ so that the total surface of the square is:

$$1 \propto N(\delta)\delta^D \,, \tag{1.48}$$

where $N(\delta)$ is the number of segments (for a full development of this formula see chapter 4). From equation (1.48) it can be easily derived that:

$$D \propto \frac{\log(N(\delta))}{\log(1/\delta)} \tag{1.49}$$

The fact that D remains constant when changing the value of δ is a clear indication that the aforementioned surface has a fractal structure.

In figure 1.8.2 we show a typical fractal structure, the so-called *Box Fractal* and covered it with squares of two different side length: $\delta = 1/3$ and $\delta = 1/9$. Applying equation (1.49) for both values of δ we obtained $D = 1.46$ thus showing clearly that we were dealing with a fractal structure. This result may seem obvious but the procedure followed here is the standard one when trying to know if a structure is a fractal one and, if that is the case, what its fractal dimension D is. In the publication presented in chapter 4 we used extensively this procedure to estimate the fractal dimensions of the avalanches produced by the SOC model of solar flares.

1.8.3 Spreading exponents

Spreading exponens are usually determined when studying avalanching systems. Compared to the avalanche statistics, spreading exponent analysis provides a more accurate and unambiguous determination of the critical point in an avalanching system.

In order to characterize spreading systems, it is customary to take several measurements: $n(t)$ is the number of avalanching sites at a specific time t and $P(t)$ measures the probability of having an ongoing avalanche at a time t. In particular, in the vicinity of the critical state, these magnitudes take the form of a power law and scale as:

$$n(t) \sim t^{\eta} \,, \tag{1.50}$$

$$P(t) \sim t^{-\delta} \,, \tag{1.51}$$

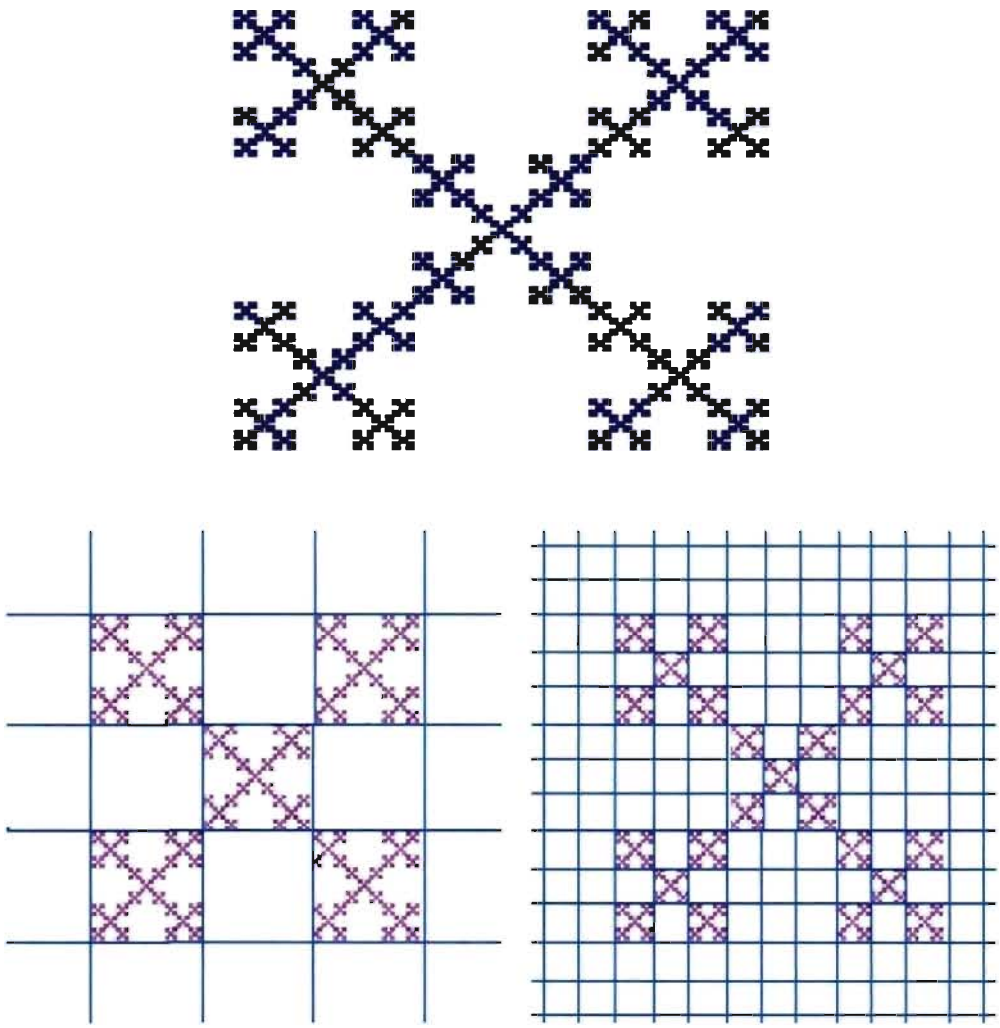

Figure 1.17: The so-called *Box Fractal* structure covered by squares of size two different sizes $\delta = 1/3$ and $\delta = 1/3$, resulting in a fractal dimension of $D = 1.46$ (adapted from: http://library.thinkquest.org/26242/full/tutorial/ch7.html)

where η and δ are the so-called spreading exponents. From these definitions, one can deduce that the total number of particles in surviving run goes as:

$$N_s \sim t^{\eta+\delta} \tag{1.52}$$

and its time integral is:

$$\int N_s \sim t^{1+\eta+\delta} \ . \tag{1.53}$$

Therefore, in an avalanche that extinguishes by time t, the number of sites involved is defined as the avalanche size and takes the form:

$$s \sim t^{1+\eta+\delta} \tag{1.54}$$

with $1 + \eta + \delta \equiv \kappa$. One last exponent can be written in terms of η and δ, using the avalanche size probability distribution. An avalanche of size s_1 can have different durations, since t and s are not related in a deterministic way. So the probability of an avalanche of size s to have any duration between t_{min} and t_{max} is:

$$P(s) = \int_{t_{min}}^{t_{max}} P(s|t)\,(1 - t^{-\delta})ds \ , \tag{1.55}$$

$P(s|t)$ is the conditional probability that an avalanche having size s expires at time t. Since $P(s|t)$ is bell shaped and has a maximum at $t \sim s^{\frac{1}{1+\eta+\delta}}$ (see [Muñoz et al., 1999]) $P(s)$ is:

$$P(s) \propto s^{\frac{-(1+2\delta+\eta)}{1+\eta+\delta}} \ , \tag{1.56}$$

thus leading to aforementioned extra exponent:

$$\beta = \frac{1+\eta+2\delta}{1+\eta+\delta} \ . \tag{1.57}$$

To the best of our knowledge, the spreading exponents for observed flares have not been calculated yet. Nevertheless this technique has been extensively applied to the dynamics of the magnetosphere [Uritsky et al., 2001], [Uritsky & Klimas, 2004]. In their analysis of an extended set of auroral images provides by POLAR UVI instruments, these authors found that the occurrence probability of auroral emissions over lifetime, energy, area and peak power output have power-law forms with nearly constant scaling exponents over a broad range of precipitating electron energies and for quite different interplanetary conditions [Uritsky et al., 2001].

1.9 This PhD Project

The main goal of this thesis is to develop a two-dimensional cellular automaton with features that could bring the numerical model closer to the theoretical scenario suggested by Parker ([Parker, 1983], [Parker, 1988]). Specifically, the following work is made up of three articles that cover different aspects of the study of avalanching systems.

The first paper is presented in chapter 2 and constitutes the pillar of this thesis. In this publication we present all the details concerning the methodology and conceptual design that lead to the new SOC model of solar flares, as well as an exhaustive analysis of the main avalanches produced by the numerical simulation. To do this, we calculate the usual power-law index estimated for classical SOC models and we also incorporate some new parameter analysis. We end the paper by replacing the simulation parameters by typical coronal dimensions and compare the results obtained with observations and theoretical predictions.

Chapter 3 is devoted to some new results obtained by calculating the spreading exponents of the cellular automaton presented in chapter 2. While this approach has been used extensively for other avalanching systems such as magnetic substorms and

direct percolation experiments, the originality of our work resides in the application of this technique to SOC models for solar flares. Another issue we consider in the paper is the study of probability distribution functions of the areas covered by the avalanching nodes. In this respect we are now in a position to resolve one the major discrepancies between the classical SOC model for solar flares and observations: the value of the power-law index that characterizes the flaring area (or in terms of a SOC model, the avalanching area).

In chapter 4 we pushed our model even closer to a coronal loop. We transform the 2D cellular automaton into a synthetic-coronal loop by applying a series of transformation matrices to the original nodes that constitute the lattice. In this context, we study the fractal properties of the avalanches produced by our numerical simulations by applying a box counting method. Although this method has been widely used on observational data, our work is a forerunner in that it extends its use to numerical simulation results of SOC flare models. In addition it is worth noticing that the synthetic loops constructed on the basis of the 2D lattice may be very helpful for improving and validating the algorithm techniques of flare detection. The synthetic flares produced by our simulation may be used as benchmark for future discrimination criteria.

In the last chapter we recapitulate the main results presented in this thesis and outline future lines of research.

Chapter 2

Self-Organized Critical model of energy release in an idealized coronal loop

Laura F. Morales & Paul Charbonneau

Département de Physique, Université de Montréal,

C.P. 6128 Succ. Centre-ville, Montréal, Qc, H3C-3J7 CANADA

Received 2007 September 27; accepted 2008 March 16

Published in *The Astrophysical Journal*, July 20, 2008, Volume 682, 654-666

2.1 Abstract

We present and discuss a new avalanche model for solar flares, based on an idealized representation of coronal loop as a bundle of magnetic flux strands wrapping around one another. The model is based on a two-dimensional cellular automaton with anisotropic connectivity, where linear ensembles of interconnected nodes define the individual strands collectively making up the coronal loop. The system is driven by random deformation of the strands, and a form of reconnection is assumed to take place when the angle subtended by two strands crossing at the same lattice site exceed some preset threshold. Driven in this manner, the cellular automaton produces avalanches of reconnection events characterized by scale-free size distributions that compare favorably with the corresponding size distribution of solar flares, as inferred observationally. Although lattice-based and highly idealized, the model satisfies the constraints $\nabla \cdot \mathbf{B} = 0$ by design, and is defined in such a way as to be readily mapped back onto coronal loops with set physical dimensions. Carrying this exercise for a generic coronal loop of length 10^{10} cm and diameter 10^{8} cm yields flare energies ranging from 10^{23} to 10^{29} erg, for a instability threshold angle of 11 degrees between contiguous magnetic flux strands. These figures square well with both observational determinations and theoretical estimates.

2.2 Flares as avalanches

Solar flares, most spectacularly visible in the extreme ultraviolet and soft X-ray domain of the electromagnetic spectrum, are the manifestation of intermittent and impulsive release of energy in the corona. The spatial coincidence of flares with magnetic structures at the solar surface leaves no doubt that flares draw their energy from the sun's magnetic field, and their very short onset time points to magnetic reconnection as the physical mechanism responsible for extracting that energy. Systematic studies of flares

from space-borne platforms have revealed the remarkable fact that the frequency distribution of solar flare energy release follows a well-defined power law, spanning eight orders of magnitude in flare energy (e.g. [Dennis, 1985], [Aschwanden et al., 2000]) with a logarithmic slope that is independent of the phase of the solar cycle even though the latter strongly modulates their frequency of occurrence. This is indicative of self-similarity, i.e., lack of an intrinsic scale in the flaring process, and is a particularly challenging characteristic for flare models to reproduce.

Large flares, though quite energetic, are known to be too infrequent to contribute significantly to coronal heating. The less energetic but far more numerous very small flares may however contribute significantly. E. N. Parker has championed this idea now for nearly a quarter of a century (see, e.g., Parker 1983, 1988, 1994; also Klimchuk 2006 for a general review of this and other coronal heating mechanisms). His basic point is that even if a coronal loop starts off as a modeler's dream, for example as a set of fieldlines nicely parallel to one another contained within a bent cylinder, stochastic displacement of photospheric footpoints by convective motions will inexorably distort and entangle fieldlines. Because of the high electrical conductivity of the coronal plasma, tangential discontinuities will form wherever two fieldlines are forced to bend around one another in their attempt to relax to a force-free state. The associated localized electrical currents will grow until one or more plasma instabilities set in, leading to reconnection, with concomitant plasma heating, particle acceleration, and emission of hard electromagnetic radiation. Note the energy flow here: the reservoir is the kinetic energy of convective fluid motions. Work done against magnetic tension at photospheric levels pumps energy in the form of kinks propagating upward into the coronal loop, where it becomes stored in the form of electrical current systems localized about tangential discontinuities. It is finally released as thermal energy into the corona by magnetic reconnection. Using typical values for the magnetic field strength in coronal loop and granular flow velocities, Parker (1988) estimated that the smallest reconnection

event that could be produced in this manner would release some 10^{24} erg, and postulated that these "nanoflares" could account for the bulk of coronal heating..

Only one minor (and physically reasonable) addition is needed to turn Parker's coronal heating model into an avalanche model for flare of all sizes: the assumption that reconnection at one tangential discontinuity can alter physical conditions in the vicinity of the reconnection site in a manner such that other neighboring tangential discontinuities can be pushed beyond the instability threshold; further reconnection at some of these sites can then trigger more reconnection at other sites further away from the original reconnection site, and so on along and across the loop until stability has been restored everywhere. The energy released by the ensemble of tangential discontinuities having undergone reconnection is then what we call a flare. Under this picture, there is nothing fundamentally different between a very small and a very large flare; the number of small reconnection events is just widely different.

Augmented in this way, Parker's model also contains all required ingredients for self-organized criticality (hereafter SOC; see [Bak, 1996], [Kadanoff et al, 1989], [Jensen, 1998] and references therein): a slowly driven (photospheric motions) open dissipative system (coronal loop) subjected to self-limiting local threshold instability (magnetic reconnection). The system is said to be "critical" because the correlation length of a perturbation is comparable to the size of the system (i.e., one small reconnection somewhere in the coronal loop can trigger reconnection along the whole loop); "self-organized" because this critical state materializes naturally following the system's own dynamics, without the need for external tuning of a control parameter. In the flare context, the SOC state is reached because photospheric fluid motions inexorably entangle the magnetic field-lines within the coronal loop, building up more and more tangential discontinuities until the instability threshold is exceeded somewhere. The exact form of the fluid motions does not matter, as long as they displace the footpoints on a timescale much longer than the readjustment time of the magnetic field within the loop.

This idea of flares as avalanches of reconnection events was first embodied into a working model by Lu & Hamilton 1991 (hereafter LH91), but see also Zirker & Cleveland (1993). Following the seminal work of Bak, Tang & Wiesenfeld (1987) on self-organized criticality in sandpile models, they designed a cellular automaton where a quantity B_k related to the magnetic field is defined on every node k of a computational grid. Small increments δB are then added in succession at randomly chosen nodes on the grid. A node is deemed to become unstable if the quantity

$$Z_k = \left| B_k - \frac{1}{n} \sum_n B_n \right| , \tag{2.1}$$

where the sum runs over node k's n nearest neighbors on the lattice, exceeds a pre-set threshold value Z_c. Whenever this happens, the nodal field B_k is redistributed according to the following discrete rules, which are the model's analog of reconnection:

$$B_k \rightarrow B_k - \frac{6}{7} Z_k , \qquad B_n \rightarrow B_n + \frac{1}{7} Z_k , \tag{2.2}$$

where the index n runs over the same nearest neighbors nodes involved in eq. (2.1), and the numerical factors pertain to a 3D cartesian grid with six nearest neighbors per interior node [1]. These rules conserve the magnitude of B, but lead to a decrease in B^2 summed over the nodes involved in the redistribution, which is taken to represent energy liberated by magnetic reconnection, and is the model's equivalent of a Parker nanoflare. But the crucial aspect is that this redistribution can also push one of the nearest neighbor node over the stability threshold, triggering further redistribution events, and so on across the lattice until every node is once again satisfying the stability criterion. Flares are then associated with these avalanche of redistribution events, and again here the distinction between large and small flares is simply the number of nodes involved in the avalanche. Lu & Hamilton (1991; see also [Lu et al., 1993], hereafter LHMB) showed that this very simple model naturally produces robust power laws in

[1] Note that on a regular Cartesian grid, eq.(2.1) is equivalent to a second-order centered finite difference discretization of a Laplacian operator acting on the nodal field.

the frequency distributions of flare energy release, peak amplitude, and duration, with logarithmic slopes in fairly good agreement with observationally-inferred values (see [Charbonneau et al., 2001] for a review of this and related SOC models of solar flares). To go beyond flare statistics, however, one needs to assign physical meaning to the nodal variable. This is where things rapidly become tricky. The obvious identification of the nodal variable is with the coronal magnetic field $\mathbf{B}$, in which case $\sum \mathbf{B}_k^2$ is indeed a magnetic energy. However the driving process is such that over the lattice, $\nabla \cdot \mathbf{B} \neq 0$ in general, which is physically unsatisfactory. LHMB proposed an alternate identification of the nodal field with a magnetic vector potential $\mathbf{A}$, where the magnetic field $\mathbf{B} = \nabla \times \mathbf{A}$. The solenoidal constraint $\nabla \cdot \mathbf{B} = 0$ is now satisfied identically, and adding a nodal increment $\delta\mathbf{A}$ becomes akin to adding some twist somewhere in the coronal loop, which is in line with Parker's picture of forcing via footpoint motions. The stability measure (2.1) is now expressed in terms of the Laplacian of $\mathbf{A}$, which in turn is directly related to the magnitude of the electrical current density $\mathbf{J}$ under the pre-Maxwellian form of Ampere's Law:

$$\nabla \times \mathbf{B} = -\nabla^2 \mathbf{A} = \frac{4\pi}{c}\mathbf{J} \ , \tag{2.3}$$

under the Coulomb gauge $\nabla \cdot \mathbf{A} = \mathbf{0}$. However, the lattice sum $\sum \mathbf{A}_k^2$ is now no longer a magnetic energy. [Isliker, Anastasiadis & Vlahos, 2000], [Isliker et al., 2001] have shown, in the context of a specific sandpile model, that variations of this quantity during a large avalanche do correlate, albeit statistically, with variations in $\sum(\nabla \times \mathbf{A})^2$. Unfortunately, the corresponding magnetic field configurations are not particularly solar-like.

Another important interpretive issue in the flare context is the underlying physical nature of the stability criterion and redistribution rules. The fundamentally discrete nature of the sandpile model places it a long way from the modeling framework most commonly used in the flare context, namely magnetohydrodynamics. Aware of this fact, Lu [Lu (1995)] demonstrated that a driven 1D nonlinear diffusion equation can lead to

SOC and power-law in dissipated energies. Partial differential equations have also been obtained by reverse engineering of the various cellular automaton rules used in SOC models of solar flares ([Isliker et al, 1998]; [Charbonneau et al., 2001]). In particular, [Liu et al, 2002] obtained in this manner a nonlinear hyperdiffusion equation from a 1D sandpile model *à la* Lu & Hamilton. They went on to extract critical exponents by a renormalization analysis, and found that the numerical values of these exponents compared favorably to those inferred empirically from running the discrete sandpile model. More recently [Bélanger et al., 2007] have repeated Lu (1995)'s computational experiment, but using a 2D version of [Liu et al, 2002]'s nonlinear hyperdiffusion equation, and found avalanching behavior comparing very well with the corresponding discrete 2D model. The upshot of all this is that the discrete CA rules of sandpile models, as *ad hoc* as they may appear, are in fact mimicking a physical process with a known and sound physical pedigree, namely diffusion. Whether or not the aforementioned reverse-engineered partial differential equations should be considered superior to the original discrete cellular automaton is a question in epistemology, and one far from uninteresting at that. The fact remains that these nonlinear hyperdiffusions equations are not related to the usual partial differential equations of magnetohydrodynamics in any obvious way, which leaves their physical interpretation essentially as open as that of the discrete CA model from which they were obtained.

In this paper we adopt the alternate approach of designing an avalanche model that, right from the beginning, follows Parker's physical picture much more closely than the now-classical SOC sandpile models of the type introduced by Lu & Hamilton. The idea is to use magnetic fieldlines as basic dynamical elements, which guarantees $\nabla \cdot \mathbf{B} = 0$. Starting with a set of parallel fieldlines of uniform strength defining a 'coronal loop', we drive the system by introducing successive, discrete local deformations, which leads to tangential discontinuities where fieldlines 'cross' , and use the angle subtended by the two fieldlines at the crossing points as a criterion for stability. When instability occurs, we reconnect fieldlines, thus restoring stability, altering topology, and releasing

magnetic energy. The model remains a form of cellular automaton, since the driving and redistribution are both introduced as simple, discrete rules for modifying the shape and connectivity of fieldlines.

Section 4.3 describes the various ingredient of our cellular automaton model, focusing in particular on the redistribution rules introduced to mimic magnetic reconnection. Representative simulation results are presented in §2.4, where we examine both the evolution towards the SOC state, as well as statistical properties of flares/avalanches in the SOC state. Section 4.5 comes back to physical considerations in the solar flare context, including rescaling of the energy release in the model in terms of physical units. We conclude in §4.7 by summarizing our most important results, identifying aspects of the model open for further improvement, and outlining the road ahead towards more physically accurate modeling of solar flares in the SOC context.

2.3 The cellular automaton

As with other SOC avalanche models, definition of the cellular automaton requires that one specifies a lattice structure, a driving mechanism, a stability criterion and a set of redistribution rules. In the flare context one also needs to assign a magnetic energy to any state of the lattice, and compute the energy liberated by avalanches of redistribution events. We consider each of these model components in turn.

2.3.1 The lattice

The system consists of a $2\,D$ lattice of size $N \times N$ that (initially) forms a network of equally spaced vertically interconnected nodes, with periodic boundary conditions in the horizontal direction. We assume that each vertical line so defined represents a magnetic flux strand (or tube), i.e., a bundle of magnetic fieldlines behaving as a

coherent entity. Figure 2.1 shows an example of a 6×6 lattice, where two nodes have been displaced from their starting position (more shortly on nodal displacements). The lattice can be thought as the external surface of a 'straightened' coronal loop made of close-packed magnetic flux strands, with the upper and lower boundaries corresponding to the photosphere. For the time being, in keeping with cellular automaton tradition, the vertical and horizontal internodal distances are taken to be the same, and define our length unit. The lattice can easily be rescaled *a posteriori* to a pseudo-loop of length much longer than its diameter for the purpose of physical analysis, as will be done in §4.5 below.

We label each node using a vectorial index $\mathbf{k} = (i, j)$, where the index i labels a magnetic flux strand and the index k the position along the i^{th} strand. Initially each set of vertically interconnected nodes defines a flux strand of dimensionless length $l_i(0) = N - 1$. It will prove important to distinguish, in what follows, between a node (identifying a position along a strand) and a lattice site, i.e., a pair of discrete $[x, y]$ cartesian coordinates; the latter will be denoted by square brackets.

Because the lattice is horizontally periodic, the first and last flux strands are one and the same; we label the first flux strand $i = 0$ to emphasize that it is not an independent entity. Note also that the lattice connectivity is here strongly anisotropic, with only top+down connectivity, unlike the top+down+right+left in 2D classical cellular automaton of the Lu & Hamilton variety (see Fig. 1 in [Charbonneau et al., 2001]).

2.3.2 Lattice energy

We need to define a measure of the magnetic energy stored in the lattice at any given iteration. The total magnetic energy within a volume V is:

$$E_B = \frac{1}{8\pi} \int_V \mathbf{B}^2 \mathrm{d}V \ . \tag{2.4}$$

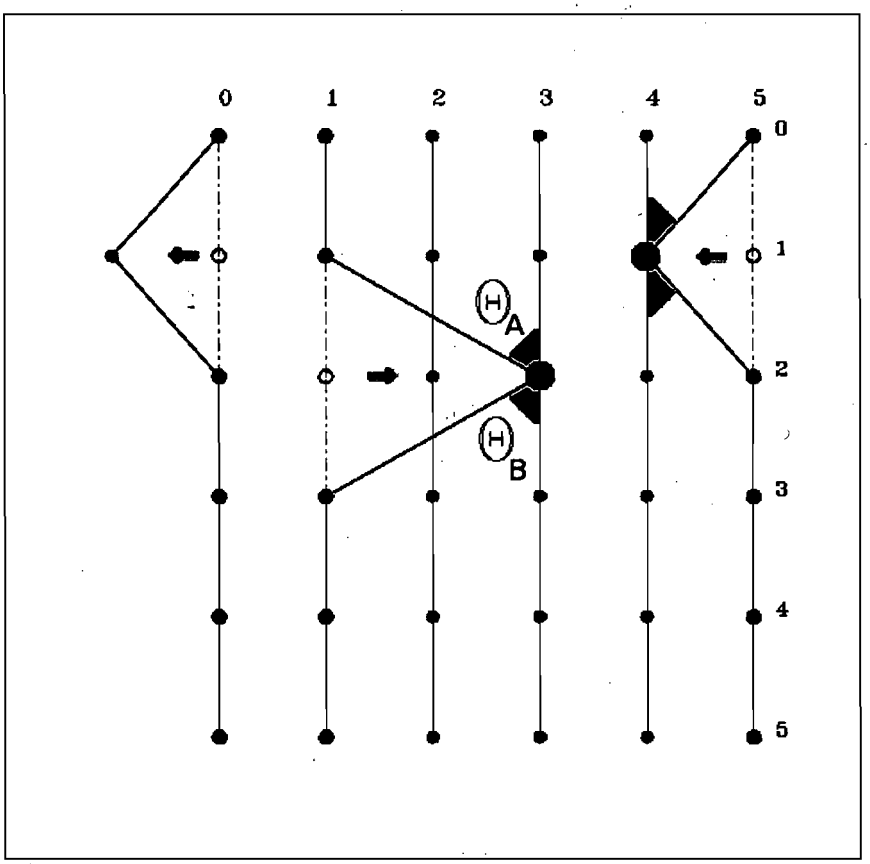

Figure 2.1: Detail of a small lattice showing the basic lattice structure and driving mechanism. Strands are numbered from left to right and nodes along a given strand, from top to bottom. Here for strand 1 the node $(1, 2)$ has been displaced two units to the right. Periodic boundary conditions are enforced, so that strands 0 and 5 always experience the same displacement (here one unit to the left for node $(5, 1)$). The gray shaded region indicates that two angles formed where two flux strands meet at the same lattice site. The first is between strands 4 and 5: $\Theta_{[4,1]} = \frac{\pi}{2}$ and the one formed between strands 1 and 3 is $\Theta_{[3,2]} \sim 2.21$. Here and in all similar figures to follow, open circles indicate lattice sites currently unoccupied by a node.

We begin by establishing a relation between the length of each flux strand and its magnetic field strength. The mass contained within a cylindrical flux strand of length l, cross-section A and constant density ρ is: $M = \rho A l$. If the flux strand behaves as a coherent entity, then upon stretching to a length l', its cross-section will shrink to A' so as to satisfy the mass conservation constraint $A\,l = A'\,l'$ in an incompressible fluid. On the other hand, conservation of magnetic flux also imposes a relation between the magnetic field strength and the cross-section: $B\,A = B'\,A'$, for a vertically-oriented, constant magnetic field within the strand. From these two conservation laws we obtain the intensity of the new magnetic field B' in terms of the length the flux strands: $B' = B \times (l'/l)$.

In terms of this model representation of the coronal loop, eq. (2.4) becomes

$$E(t) = \frac{l_0\,A_0}{8\pi}\,B_0^2 \sum_{i=1}^{N-1} l_i^2(t), \tag{2.5}$$

where l_0, A_0 and B_0 are the initial length, cross-section and field strength of the strands, and $l_i(t)$ is the length of strand i at time t. Since a flux strand is "discretized" into N nodes (including boundary nodes), it has an initial length $l_0 \propto N-1$; further assuming that in the initial state the flux strands are space-filling, the initial energy of a $N \times N$ lattice will be:

$$E_0 = \frac{l_0\,A_0}{8\pi}\,B_0^2\,(N-1)^3 \tag{2.6}$$

This quantity will be used as our unit of energy in all that follows.

2.3.3 Driving mechanism

We now need a driving mechanism to inject energy into the lattice. This is achieved by introducing, at each (non-avalanching) iteration horizontal displacements of a randomly chosen single node. Displacement towards the right is referred to as positive (δ_+), and

to the left as negative (δ_-).

For example, on Figure 2.1 the set of nodes $\{(1,0),(1,1),(1,2),(1,3),(1,4),(1,5)\}$ still defines flux strand number 1, after node $(1,2)$ was displaced two units to its right.

We set $\delta_+ = 2$ and $\delta_- = 1$, with equal probability for each choice at any node and iteration. Each node then ends up executing, over a great many iteration, a biased 1D random walk. The choice $\delta_+ > \delta_-$ is arbitrary, but an inequality is needed for the flux strands to develop a global pattern of twist as the simulation proceeds. This will also lead, statistically, to a gradual lengthening of each flux strand, so that the lattice energy goes up, as per eq. (2.5), following the introduction of these nodal displacements. Evidently more complicated schemes on the same theme could be devised, but this very simple one was found to succesfully drive the system to a SOC state, as demonstrated shortly.

Note that in the initial state, all lattice sites are occupied by a single node belonging to a single vertical flux strand. As driving proceeds, however, some lattice sites can become empty, such as site $[1,2]$ on Fig. 2.1 (open circle), or be occupied by more than one node, such as site $[3,2]$, occupied by nodes $(1,2)$ and $(3,2)$, or site $[4,1]$, occupied by nodes $(4,1)$ and $(5,1)$.

Consider now any horizontal plane, equivalent to a cross-section of the loop. The nature of our driving mechanism is such that the number of flux strands crossing that plane is always $N-1$. Moreover, our adopted procedure to vary the strength of a flux strand in response to variations in its length conserves magnetic flux within the strand by design. This implies that our model automatically satisfies the flux conservation constraint $\nabla \cdot \mathbf{B} = 0$ globally as well.

As with most conventional SOC model, driving only takes place when the lattice is everywhere stable (i.e., no avalanches). In the solar flare context this is a good approximation, given that driving is associated with photospheric fluid motions (with characteristic timescale of some tens of minutes for the granular flow), while avalanching

is associated with magnetic reconnection and characteristic timescale below a few minutes. Nodes at the upper and lower boundaries are excluded from the driving process, again in order to favor the buildup of a global twist pattern along our pseudo-loop.

2.3.4 Stability criterion

Each node in the lattice now has to be tested for stability. Parker (1983) argues that whenever two misaligned flux strands are pressed together, a tangential discontinuity forms, with which is associated an electrical current sheet. Reconnection takes place if the current magnitude exceeds some threshold, which translates into a critical angle subtended by the magnetic fieldlines forming the outer flux surfaces of each flux tube (see also Parker 1988). The evolution of such a flux strand configuration has been simulated recently by [Dahlburg et al., 2005], who confirm Parker's general scenario, although they trace the onset of fast reconnection to a secondary instability of the current sheet.

This overall scenario is readily representable in our model, by using the angle subtended by two flux strands crossing at the same lattice site as a criterion for instability. We define the total angle $\Theta_{[i,j]}$ formed between two strands as the sum between the angle formed with respect to the vertical direction by the two strands that "enter" site $[i,j]$ from above and the two strands that "leave" the site towards the bottom. On Figure 2.1 for example, strands number 1 and 3 meet at site $[3,2]$. In this case both angles (Θ_A and Θ_B) are the same: $\Theta_A = \Theta_B = \arctan[\frac{|1-3|}{|2-1|}] = 1.107\,\mathrm{rad}$, where the numerator of the fraction is obtained by the difference between the first component of the upper node (in this case 1) and the first component of the site where the angle is being formed (in this case 3). On the other hand the denominator of the fraction will always be equal to 1 because it always corresponds to a single vertical increment (internodal distance) along each strand. This gives a total angle of $\Theta_{[3,2]} = 2\arctan(2) = 2.214\,\mathrm{rad}$. We then assume that the site is unstable whenever this total angle is greater than some

preset threshold value Θ_c. If it were the case that $\Theta_c = 2\,\mathrm{rad}$, then here the site [3,2] is unstable and we need to introduce a redistribution rule.

2.3.5 Redistribution rules

If any one lattice site has been found to be unstable, a redistribution process is needed to restore stability. This can be achieved either by reducing the angle subtended by flux strands crossing at the unstable site[2], or displacing the offending node from one of the flux strands away from the site, thus "eliminating" the unstable angle. Whichever occurs, an important additional constraint is that the redistribution must release magnetic energy (otherwise it could not be mimicking a "spontaneously" occurring magnetic instability).

For illustrative purposes, consider the situation shown on Fig. 2A, again for an exceedingly small 6×6 lattice. Following a positive displacement of node $(1,3)$ by two units, strands 1 and 3 now cross at site $[3,3]$ with a total angle $\Theta_{[3,3]} = 2.21$; for a threshold $\Theta_c = 2$, this angle is deemed unstable (indicated by a larger solid dot). The reconnection procedure begins with the reconnection of strands 1 and 3, by a cut-and-splice operation at site $[3,3]$ (A→B on Fig. 2B). After this procedure node $(3,3)$ is displaced from the unstable site $[3,3]$ to site $[2,3]$ (B→C). Site $[3,3]$ is now trivially stable since it is only occupied by strand 1, but strand 3 now crosses strand 2 at site $[2,3]$. The total angle formed there is $\Theta_{[2,3]} = \pi/2$, and is here stable for $\Theta_c = 2$.

At this point we check whether energy has been released: if the energy of the new configuration is smaller than the energy of the previous configuration the two-step redistribution scheme is considered complete, and the simulation can go on to the following iteration. However, the relocation of one of the nodes may have now produced

[2]Of course, real vector magnetic fields do not "cross" (null points notwithstanding), as this would imply that **B** is no longer a single-valued function at the crossing point. Crossings on our 2D lattice are simply the analogue of Parker's tangential discontinuities.

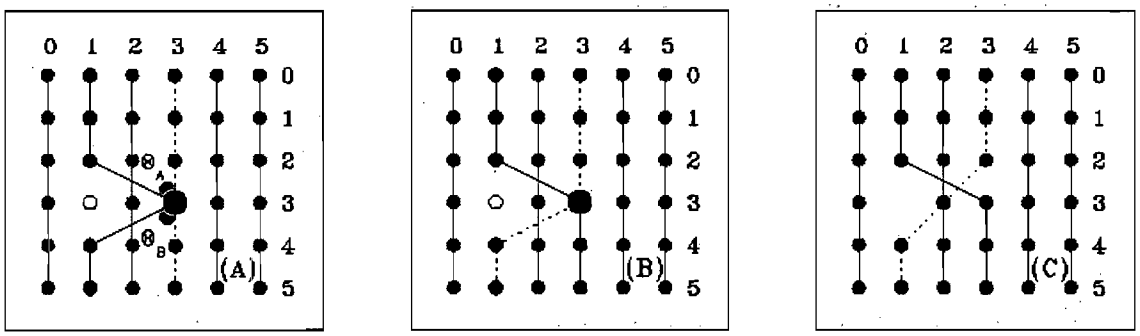

Figure 2.2: A sequence of the two-step redistribution scheme. In figure (A) we can identify the unstable site $[3,3]$ (larger black dot) formed by flux strands 1 and 3. The total energy at this stage is: $E_A = 1.25\,E_0$. In figure (B) strands are reconnected. This procedure is successful in reducing the total energy ($E_B = 1.22\,E_0$) but the site remains unstable. In (C) the node $(3,3)$, that belongs to strand 1, is displaced (to the left) leading to a configuration where the total energy is $E_C = 1.18\,E_0$ and the unstable angle is eliminated. The energy released by the whole procedure is $E_r = E_A - E_C = 0.07\,E_0$.

a new unstable angle at a neigbouring site; if so redistribution begins anew, and so on in classical avalanching manner.

If the "two-step" redistribution scheme of Fig. 2 has not been succesful, in the sense that it would lead to an *increase* of lattice energy, then we have to introduce an additional step. To do this we operate over the four nearest nodal neighbors of the unstable site, i.e., nodes located at $j \pm 1$ on each of the two strands crossing at the unstable site. One at a time, each of these nodal neighbours is displaced randomly right or left, and the (provisional) lattice energy recomputed and compared to the current lattice energy. The procedure stops as soon as one such energy-reducing displacement is found. We call this procedure a "three-step" redistribution scheme. An example is shown in Figure 3. Here the total angle $\Theta_{[3,2]} = \Theta_A + \Theta_B + \Theta_D$ is comprised of three contributions, namely $\Theta_A = \Theta_D = \arctan(1) = \pi/4$, and $\Theta_D = \arctan(2) \sim 1.10$, so that $\Theta_{[3,2]} = 2.67$. Assuming once again that $\Theta_c = 2$, then $[3,2]$ is an unstable

site. We begin redistribution in the same manner as before: strands 2 and 3 are reconnected (A→ B), but at site [3, 2] we still have not reduced or eliminated the unstable angle; moreover, the lattice energy has risen from $1.32E_0$. to $1.332E_0$. Either one (randomly chosen) of the two nodes occupying that site is then displaced. In this case the node (3, 2) (belonging to strand number 3) was moved one unit to its left (B→C). In this manner the site [3, 2] is no longer unstable, but lattice energy has now climbed to $1.4E_0$. With lattice energy having increased throughout the A→C sequence, it becomes necessary to add an additional step to the redistribution scheme. This new step consists in moving one of the four neigbouring node (one at a time) and monitor the corresponding variations in lattice energy. Here the four neigbouring nodes are at sites: [2, 1], [5, 1], [2, 3] and [3, 3] (open squares). The order in which these neighbouring nodes are displaced, and the direction of the horizontal displacement, are both chosen randomly. For the specific case illustrated in Fig. 3, node (3, 1) is displaced from site [5, 1] to [4, 1] (C→D), and this turned out to to lower the lattice energy to $1.19E_0$, so that the total energy released during the redistribution is $E_r = E_A - E_D = 0.13E_0$. This brings the three-step scheme redistribution scheme to a close. However, this final configuration D now contains a new unstable site at [4, 1]. This is the beginning of an avalanche.

Whether the two- or three-step redistribution scheme ends up being used, all operations are assumed to take place within a single time iteration. Monitoring of our model runs reveals that the three-steps redistribution scheme ends up taking place at 40% to 45% of unstable nodes (depending on lattice size and threshold angle), with the remainder redistributing according to the basic 2-steps algorithm. Whichever version of the redistribution scheme ends up being used, the sum of all energy so released at each unstable site represents the energy released by the flare at that iteration.

The reconnection step in our redistribution schemes (A → B on Fig. 2) may appear superfluous, as it is not changing anything to the distribution of angles at or near the unstable site, nor is it changing the total length of the two strands involved. It is,

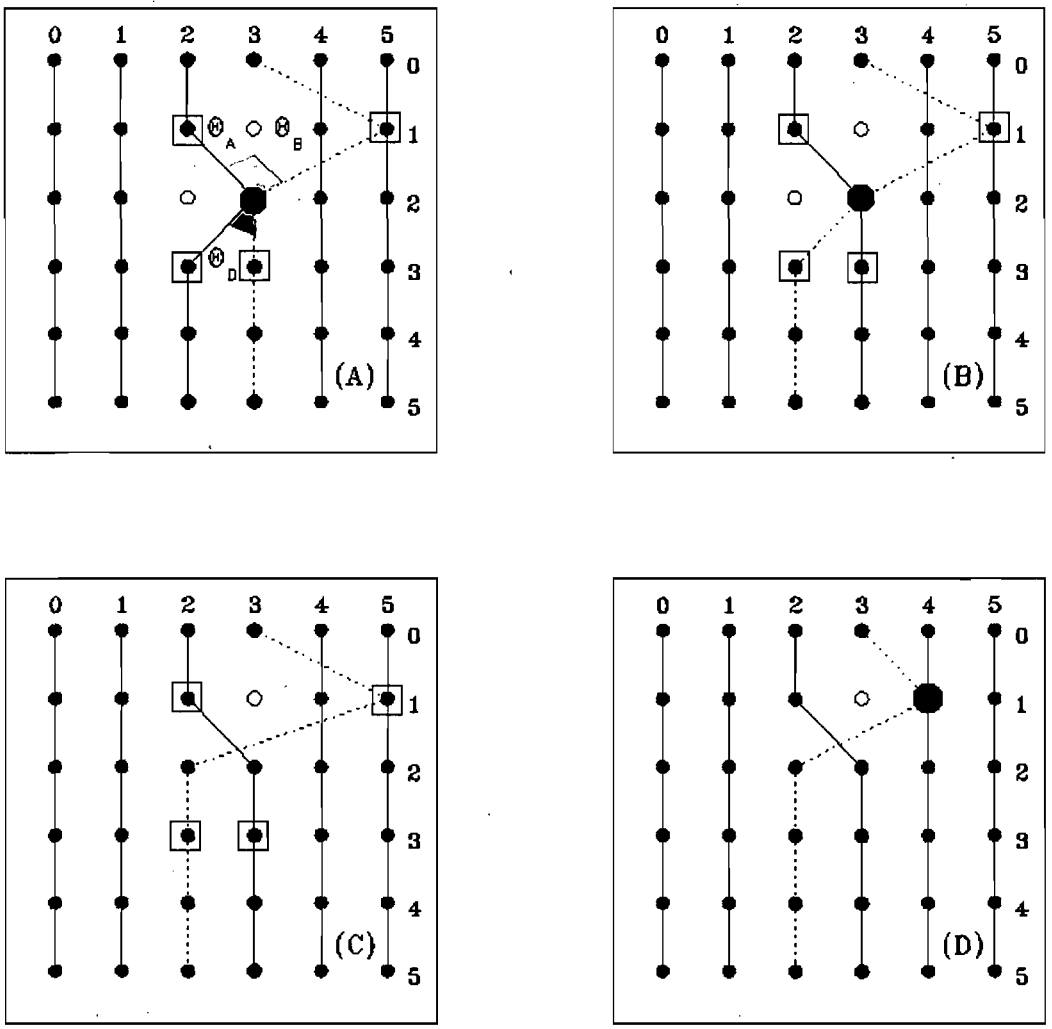

Figure 2.3: An example of the three-steps redistribution scheme applied when the two-steps scheme fails to release energy. In (A) strands 2 and 3 form an unstable angle at site [3, 2] (larger black dot): $\Theta_{[3,2]} = \Theta_A + \Theta_B + \Theta_D$, as labeled. The lattice energy is here equal to $1.32E_0$. Panel (B) shows the lattice after the reconnection step; the new lattice energy is $1.332E_0$, but the site [3, 2] remains unstable. Panel (C) shows configuration after displacing one node at the unstable site, with lattice energy $E_C = 1.4E_0$ and panel (D) the configuration resulting from the displacement of one of the four nearest-nodal neighbours (open squares), finally lowering the lattice energy to $E_D = 1.19E_0$. Here the three-steps sequence A→B→C→D has released an amount of energy equal to $E_r = E_A - E_D = 0.13E_0$.

however, changing the lattice energy (proportional to the sum of the lengths squared, viz. eq. 2.5). Its most important role, however, is to allow topological changes in the lattice; otherwise the simulation rapidly reaches a stationary state characterized by very frequent small avalanches, where nodes just move back and forth in response to driving and redistribution, with all strands arched to the right (for $\delta_+ > \delta_-$) with similar curvatures. There is a direct analogy here with Parker's nanoflare scenario, where reconnection is needed to break the topological constraints imposed by flux-freezing, with energy release being a form of side-effect associated with the return of the stressed coronal loop to a metastable dynamical equilibrium.

2.4 Model Results

We have run the cellular automaton described in the preceding section for different lattice sizes and stability threshold values, as listed in Table 1. In all cases driving makes uses of an anisotropic perturbation amplitude, i.e., $\delta_+ = 2$ and $\delta_- = 1$, chosen randomly but with equal probability at each driving iteration. All simulation begin with a configuration of vertically-oriented, straight flux strands parallel to one another.

2.4.1 Getting to the SOC state

Figure 2.4 shows results for the first 1.5×10^6 iterations of simulation C2 (128×128 lattice, $\Theta_c = 2.5$), and is representative of other runs at different stability thresholds or lattice sizes. Part (A) shows the variation of lattice energy (solid line), part (B) the energy released by avalanches, and part (C) the frequency distribution of flux strand lengths at four (non-avalanching) iterations, corresponding to times indicated by solid dots and labeled a through d on part (A). In the cases c and d we used an enhanced sample producced by using 18 neigbouring-non statisticaly related iterations.

Table 2.1: Simulations parameters and global results

Simulation	N	Θ_c(rad)	η	$\langle\eta\rangle$	$t_{\rm SOC}[10^5]$
A1	32	2	1.45	0.00280	5
A2	32	2.25	1.56	0.00253	5.9
A3	32	2.5	1.33	0.00195	7.5
B1	64	2	0.62	0.00091	2
B2	64	2.25	0.72	0.00060	3.2
B3	64	2.5	0.21	0.00040	5
C1	128	2	0.13	0.00072	2.8
C2	128	2.25	0.04	0.00052	3.3
C3	128	2.5	0.15	0.00034	8

As flux strands are inexorably stretched by the driving process, the lattice energy grows rather quickly at first, increasing by a factor of ~ 6 with respect to the initial energy. During this growth phase the mean of the distribution of strand lengths (Fig. 2.4C) increases more than twofold, while the distribution itself broadens significantly. The lattice energy levels off gradually after some $\simeq 3 \times 10^5$ iterations, while small avalanches take place intermittently. By then a statistically stationary state seems to have been reached, but pushing the simulation further reveals a rather sudden increase in the size of the largest avalanches, taking place here after some $\simeq 9 \times 10^5$ iterations, and accompanied by a small but significant drop in lattice energy. It is only now that the system is in a truly stationary state, which we identify as a SOC state. As in the Lu & Hamilton model, arrival at the SOC state is accompanied by a sudden increase in the size of the largest avalanches (compare Fig. 2.4 herein to Fig. 3 in [Charbonneau et al., 2001]). In the context of the present model, the best indicator we have found to ascertain when this occurs is the mean rate of energy released by avalanches, plotted along the bottom of Fig. 2.4(A) as a gray line, which rises abruptly upon arrival in the SOC state. Some-

what surprisingly, one notes on part (C) that the distributions of flux strand lengths do not show large differences between snapshots c and d, except perhaps for the distribution in the SOC state being a little broader. It's not so much the length of the strands that matters, but the pattern of crossing angles they make on the lattice. The time at which the SOC state appears is henceforth denoted t_{SOC}, and is listed in Table 2.1 for all simulations included therein. Examination of the various simulation runs reveals that it is only starting at t_{SOC} that avalanche spanning the whole lattice begin to take place.

2.4.2 Avalanche energetics

In the SOC state, the amount of energy released by the larger avalanches is one to two orders of magnitude smaller than the total lattice energy. Releasing a few percent of the lattice energy is still quite substantial; for example, in the 2D version of the Lu & Hamilton model run on a lattice of comparable size, that fraction is around 10^{-6}. In order to quantify the efficiency of our cellular automaton we define a ratio η between the energy liberated by the largest avalanche to the mean lattice energy in the SOC state, as well as a ratio $\langle\eta\rangle$ of mean energy release per iteration to the mean lattice energy. Both of these quantities are listed in Table 2.1. For any fixed lattice size, the ratio $\langle\eta\rangle$ is found to decrease as the critical threshold angle is increased. This trend is precisely that suggested by the theoretical analysis presented in Parker (1988).

Figure 2.5 shows three histograms of the frequency distribution of angles normalized to the instability threshold Θ_c. The distributions are constructed using forty non-avalanching iterations, widely spaced in time but all at times larger than t_{SOC}, in simulations A2, A3 and C3 (see Table 1), as labeled. In view of the discrete nature of the nodal distribution along flux strands and of the nodal displacements used for driving, the geometrically realizable angles at lattice sites are themselves not uniformly distributed in the $[0, \pi]$ interval, which is why in part the binned distributions of unstable

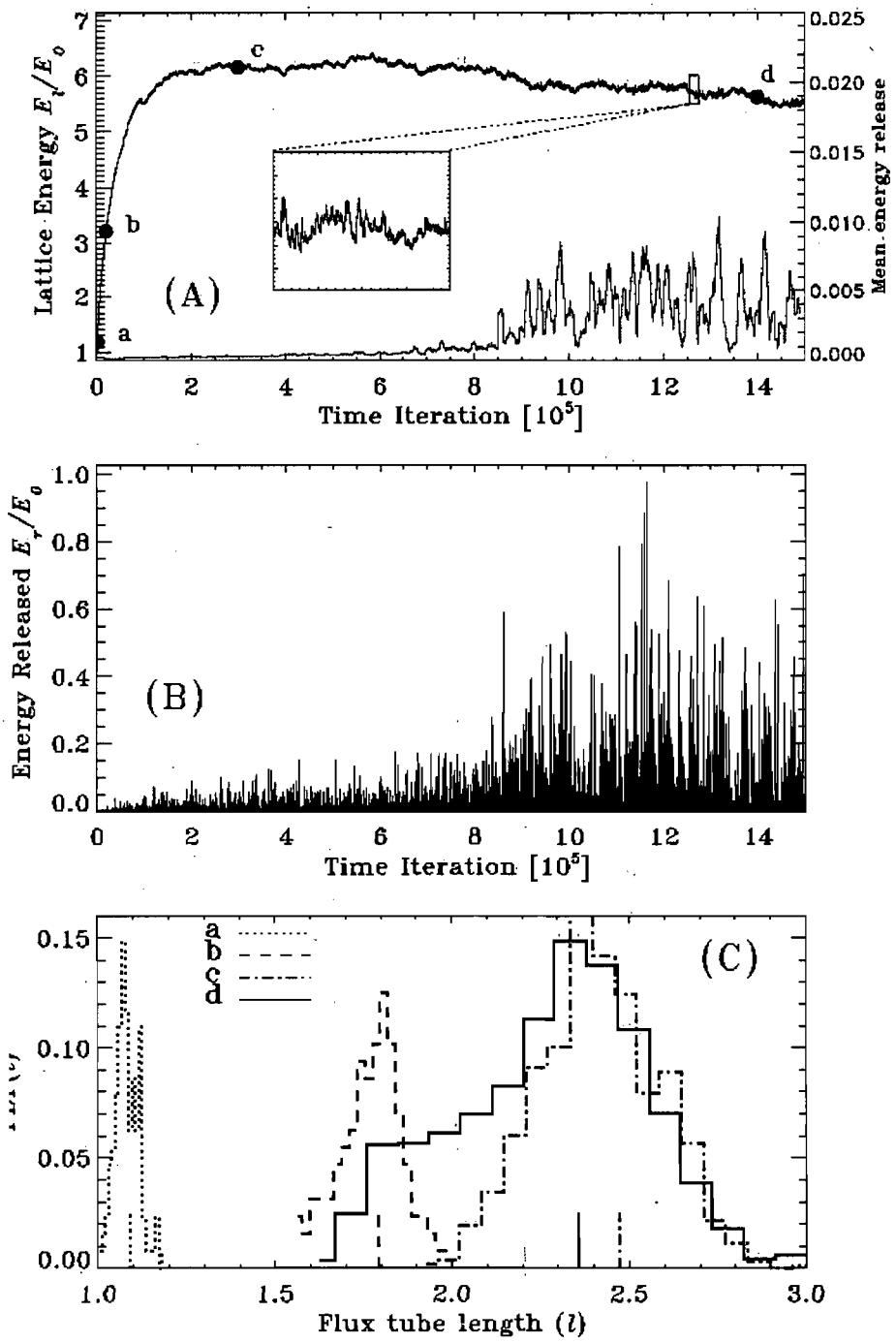

Figure 2.4: Time series of (A) total lattice energy and (B) energy released in avalanches for a 128 × 128 node lattice with $\Theta_c = 2.5$ rad. The inset on panel A shows a small portion of the lattice energy time series within the SOC, and the gray line shows the mean value of energy release calculated as a running mean spanning one thousand iterations. Panel (C) depicts the frequency distribution of strand length values extracted at the four different epochs in the simulation indicated by the solid dots along the energy release curve on part A.

angles on Fig. 2.5 show so much structure. Nonetheless, all distributions are similarly shaped and have a mean value $\Theta/\Theta_c \sim 0.6$, for varying threshold angles and lattice sizes. Moreover, in all cases the vast majority of angles formed at sites where two strands cross are well below their stability threshold. This is analogous to the Lu & Hamilton model, where the majority of lattice nodes also present a curvature significantly below the curvature threshold (see Fig. 4 in [Charbonneau et al., 2001]).

2.4.3 Spatial structure of avalanches

Figure 2.6 illustrates the unfolding of a typical large avalanche in the B1 simulation after the SOC state has been reached. The first five frames (A through E) are snapshots showing the locii of unstable sites at specific iterations in the course the avalanche, with (A) corresponding to onset (a first, single unstable site), (C) to the iteration with peak energy release, and (E) to the end of the avalanche, here with a single remaining unstable site. On frames (A) and (E) the global shape of the two flux strands crossing at the unstable site are also plotted. Frame (F) shows the "footprint" of the avalanche, i.e., the locii of all lattice sites having gone unstable at least once during the avalanche, here adding up to 204 sites. Note the small "island" of unstable sites to the right of the main avalanche footprint. This may appear odd —and has no counterpart in classical cellular automaton such as the LHMB model,— but recall that here the nearest neighbour nodes of a node at an unstable site $[i, j]$ need not be located only at $[i \pm 1, j \pm 1]$; On Fig. 1 for example, node $(1, 2)$ located at site $[3, 2]$ has its two nearest neighbour top+down nodes at sites $[1, 1]$ and $[1, 3]$). What matter in our model are nearest neighbours along a given flux strand, which do not necessarily lie at nearest neighbouring lattice sites.

The bottom panel on Fig. 2.6 shows the corresponding time series of energy release. Notice how the energy release can fluctuate quite markedly during the avalanche, with multiple sub-peaks presents; with real data, i.e., in the presence of a detection threshold, background noise or poor time resolution, it may be difficult to recognize this as a single

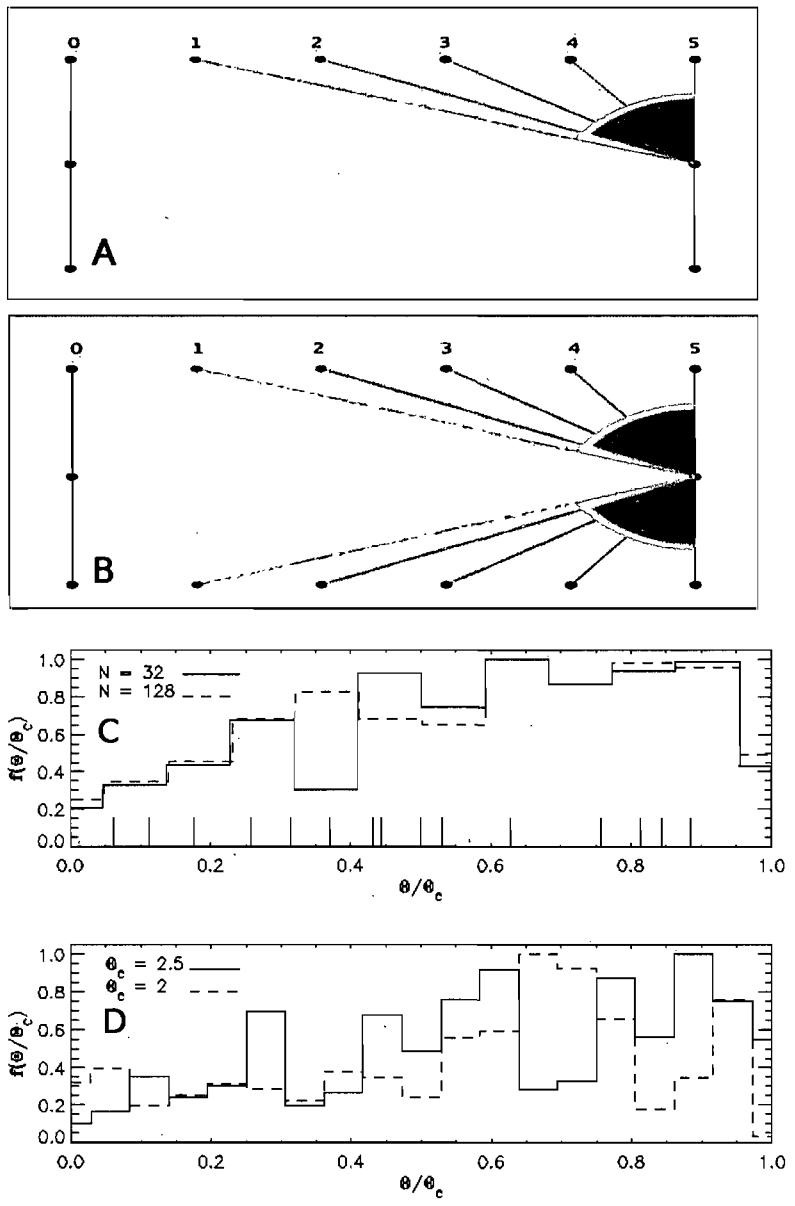

Figure 2.5: Distribution of angles (normalized to the critical threshold Θ_c. In (C) we compare simulations A1, A3 and in (D) we compare simulations A3 and C3 (see Table 1). Each distribution is constructed from a selection of sixty non-avalanching iteration widely spaced in time but all in the SOC state. For the three distributions the mean value is 0.6. Panels (A) and (B) show for a small lattice some of the different situations in which two strands can intersect and form and angle. The correspondingly discrete set of angles are plotted along the x-axis on panel (C). The full set of possible angles forms a dense, non-uniform discrete spectrum.

avalanche, rather than a sequence of closely spaced smaller distinct avalanches. In other words, the energy release curve (corresponding conceptually to flare luminosity in hard radiation) is not comprised of a well-defined rising phase followed by a smooth decay phase, but is instead quite bursty. This feature is also present in time series of energy release in the LHMB model, but not to the same extent as here. Observations of flares in hard X-Rays are indeed far more bursty than at longer UV wavelengths (see, e.g., Fig. 2 in Warren & Warshall 2001).

2.4.4 Avalanche statistics

We now turn to the global characterization of avalanches, using the following four quantities: the peak energy release (P) is the maximum energy released in a single iteration in the course of an avalanche (such as at time C on the lower panel of Fig. 2.6); the total energy (E) is the sum of all energy released at all unstable sites in the course of an avalanche (the sum of all bins on the time series in Fig. 2.6); the duration (T) is the number of iterations from the onset of the avalanche to the recovery of stability across the whole lattice (between A and E on Fig. 2.6); and finally the waiting time (ΔT), the time elapsed between the end of one avalanche and the beginning of the following one. These quantities are thus readily extracted for each avalanche in the time series of energy release produced by the model. We can then build the probability distribution functions (hereafter PDF) for E, P, T and ΔT. The results of this exercise are shown in Figure 2.5 for model C3 (128×128 lattice with $\Theta_c = 2.5$). The PDFs for E, P and T all take the form of power-laws, i.e.:

$$\mathrm{PDF}(X) \propto X^{-\alpha_X} , \qquad X \in \{E, P, T\} , \tag{2.7}$$

spanning up to three orders of magnitude in size. The corresponding power law indices are listed in Table 2.2. For comparison, in the 2D scalar version of the LHMB model one finds $\alpha_E = 1.40$, $\alpha_P = 1.70$, $\alpha_T = 1.70$ for a 128×128 lattice ([Charbonneau et al., 2001]).

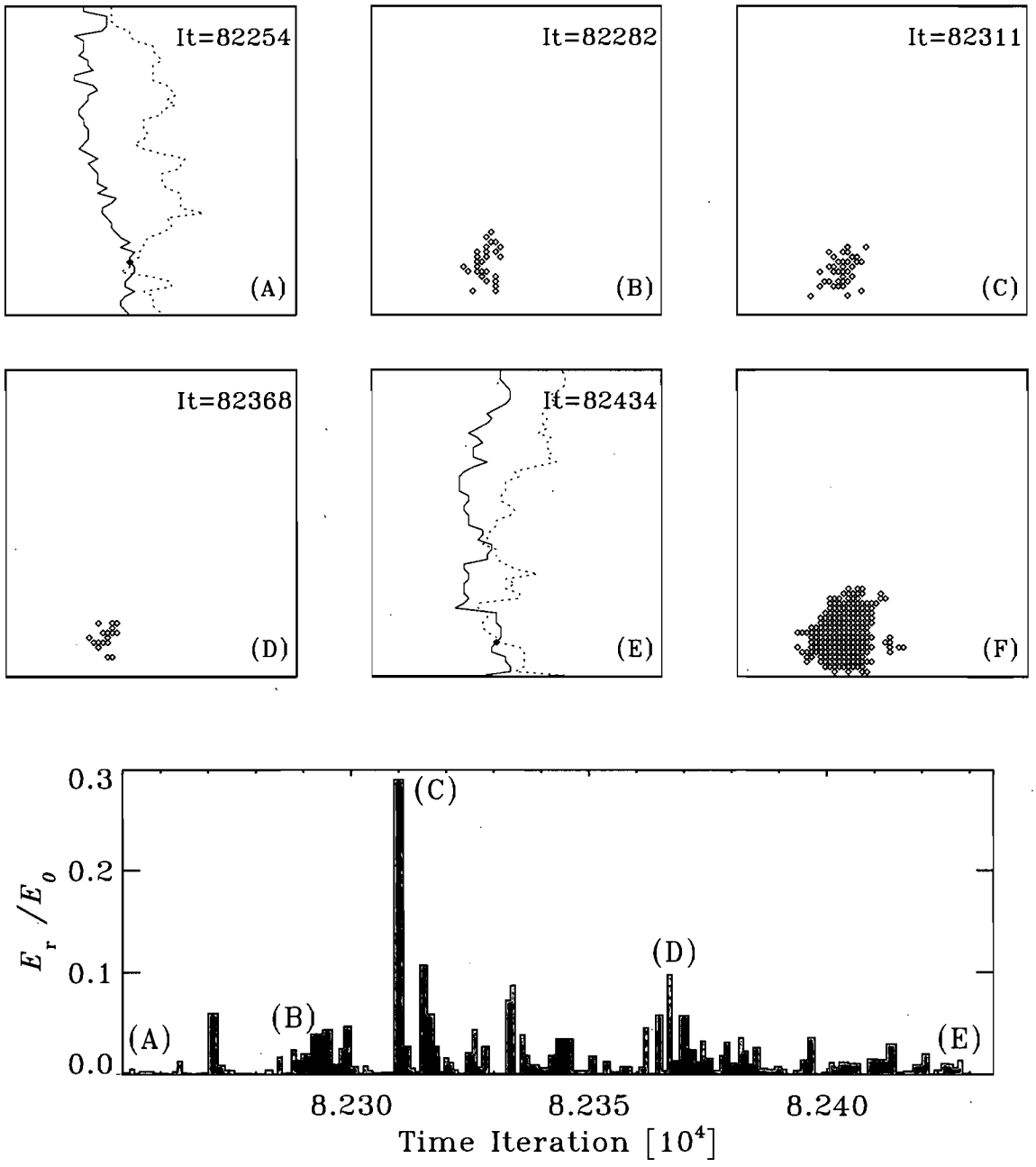

Figure 2.6: Snapshots of an ongoing avalanche in simulation B1 (A-E). (A) and (E) are the beginning and the end of the avalanche respectively. (B) and (D) are any two moments during the avalanche and (C) is extracted at the iteration of peak energy release during the avalanche. (F) shows the total area covered throughout the avalanche, i.e., the ensemble of lattice sites having gone unstable at least once during the avalanche. The bottom panel is the corresponding energy release time series; note that this does correspond to a single, continuous avalanche, energy release falling all the way back to zero only at the very end of the plotted time interval.

Observational determinations, on the other hand, indicate $\alpha_E = 1.54 \pm 0.11$ (Aschwanden & Parnell 2002); α_P ranging from 1.79 ± 0.05 to 2.11 ± 0.13 (cf. [Yashiro et al,, 2006] and [Veronig et al., 2002]); the observational determination of α_T is usually the hardest, because of background noise and detection threshold effects, with values scattered in a broad range, going from $\alpha_T \sim 1.15 \pm 0.04$ to 2.93 ± 0.12 (see [Yashiro et al,, 2006], [Veronig et al., 2002], [Yang et al., 2006] and [Georgulis et al, 2001]). Our PDFs are thus slightly steeper than LHMB, but match observational statistics comparably well. The waiting time distribution, on the other hand, is exponential, reflecting the fact that the driving mechanism is a stationary, memoryless random process (in this context see [Wheatland, 2000] and [Norman et al., 2001]).

As can be seen on Figure 2.8, the avalanches size measures E, P and T are also statistically related via power law relationships of the general form

$$Y \propto X^{\gamma_{XY}} , \qquad X, Y \in \{E, P, T\} . \tag{2.8}$$

The associated power-law indices are again listed in Table 2.2. In the 2D scalar version of the LHMB model one finds: $\gamma_{PE} = 1.42$, $\gamma_{TE} = 1.72$, $\gamma_{TP} = 1.71$ for a 128×128 lattice (e.g., [Charbonneau et al., 2001], Table II); observations suggest $\gamma_{PE} = 1.12 - 1.14$ and $\gamma_{TE} = 1.47 - 1.88$, $\gamma_{TP} = 1 - 1.64$ ([Veronig et al., 2002]; [Georgulis et al, 2001]). Here the present avalanche model fits within the observationally determined ranges much better than the LHMB model.

One feature on Fig. 2.7A and B that has no counterpart in the Lu & Hamilton-type avalanche model is the presence of a well-defined plateau in the PDFs for E and P, at the low end of the size distributions. Interestingly, no such plateau appears in the PDF for avalanche duration, suggesting that we are not witnessing here a break of finite size scaling. What is happening is that a small avalanche involving even just a single node can still liberate energy within a broad range, since this is determined by the difference in lengths squared before and after the reconnection for the two flux strands involved (cf. §2.3.2). Depending on the two strands being reconnected, this difference can span

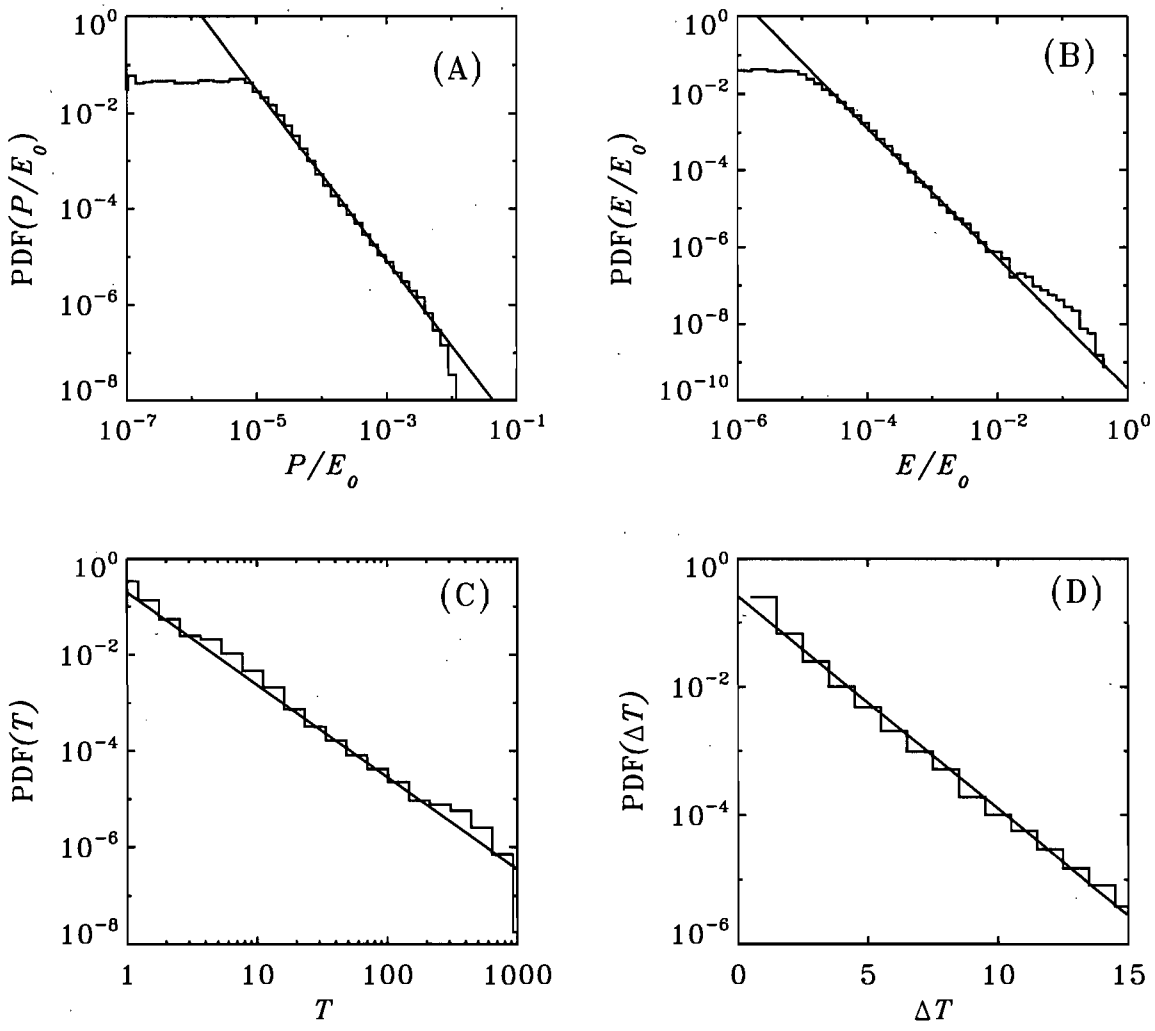

Figure 2.7: Probability distribution functions of avalanche size measures E, P and T and inter-event waiting time ΔT in a representative 1.5×10^6 iterations run of model C3. Only the portion of the time series corresponding to the SOC state is used to build these statistics.

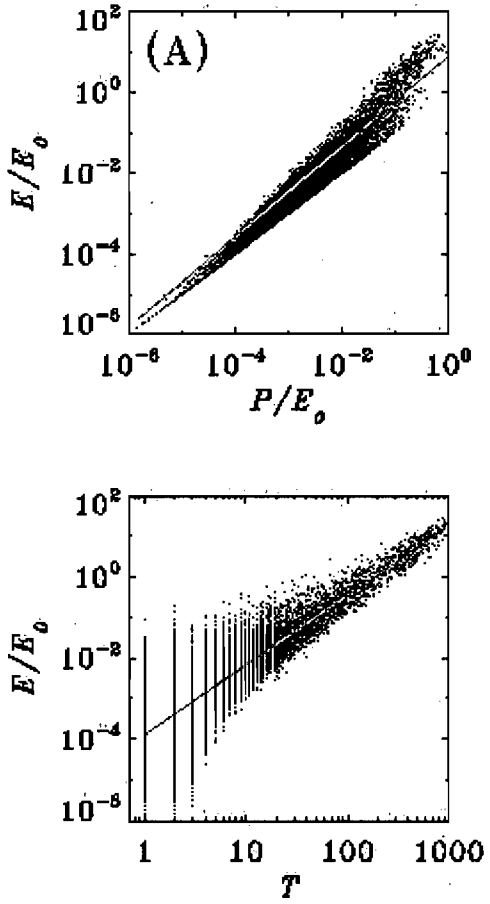

Figure 2.8: Correlation plots of avalanche energy (E) vs peak luminosity (P), energy vs duration (T) and peak luminosity vs duration, for simulation C3. Note that by definition, $E \geq P$. Gray lines are least-squares fits.

Table 2.2: Simulations parameters and results

Simulation	α_E	α_P	α_T	γ_{PE}	γ_{TE}	γ_{TP}
A1	1.63 ± 0.03	1.79 ± 0.03	1.82 ± 0.09	1.13 ± 0.1	1.94 ± 0.3	1.45 ± 0.3
A2	1.63 ± 0.03	1.78 ± 0.02	1.95 ± 0.09	1.09 ± 0.1	1.73 ± 0.3	1.26 ± 0.25
A3	1.64 ± 0.04	1.73 ± 0.05	1.93 ± 0.05	1.09 ± 0.1	1.78 ± 0.3	1.34 ± 0.25
B1	1.70 ± 0.02	1.74 ± 0.03	1.80 ± 0.09	1.15 ± 0.1	1.75 ± 0.3	1.45 ± 0.25
B2	1.70 ± 0.03	1.76 ± 0.01	1.89 ± 0.09	1.23 ± 0.2	1.88 ± 0.2	1.32 ± 0.15
B3	1.65 ± 0.02	1.81 ± 0.02	1.90 ± 0.07	1.1 ± 0.2	1.60 ± 0.2	1.20 ± 0.2
C1	1.66 ± 0.05	1.84 ± 0.04	1.79 ± 0.08	1.26 ± 0.1	1.77 ± 0.2	1.20 ± 0.2
C2	1.72 ± 0.05	1.84 ± 0.04	1.85 ± 0.07	1.25 ± 0.2	1.80 ± 0.2	1.18 ± 0.2
C3	1.71 ± 0.05	1.78 ± 0.05	1.92 ± 0.02	1.20 ± 0.2	1.71 ± 0.2	1.15 ± 0.2

a wide range; yet if one of the nodes is displaced to an empty site in the course of redistribution (cf. §2.3.5), the avalanche immediately stops, leading to an avalanche of duration unity. Indeed, the statistics includes many avalanches for which $E = P$ (the signature of avalanches of duration unity) showing up as a well defined "diagonal" on Figure 2.8A. Moreover, moving on to Fig. 2.8B, avalanches of duration unity are seen to span five orders of magnitude in flare energy. Consequently, the upper left portions of Figure 2.8B and C are more populated than the corresponding correlation plots for the LHMB model (see Fig. 7 in LMHB, or Fig. 6 in [Charbonneau et al., 2001]), also leading to somewhat lower power law exponents in eqs. (2.8). However, we have not been able to come up with a simple, convincing explanation for the sharpness of the transition between the plateau and power-law portions of the total energy and peak PDFs.

Examination of Table 2 readily reveals that values of the α and γ exponents obtained on different lattice sizes or threshold angle all fit within each other within their error

bars (associated with the least-squares fits). The existence of power-law relationships between avalanches size measures, together with the power-law form of their PDFs, and the constancy of the associated power-law exponents as the lattice size and threshold value are varied, all point to a lack of a typical scale for avalanches, a sine qua non feature of SOC systems.

2.5 Return to dimensionality

One of the most appealing differences between our SOC model for solar flares and the more conventional sandpile-like models is the possibility to restore physical dimensions to the simulations output. In what follows we outline how this can be achieved, reserving a fully detailed comparison to observations to a subsequent paper.

2.5.1 Loop size

Our cellular automaton is defined over a 2D unit lattice with equal horizontal and vertical spacing between lattice sites. If the lattice is to be interpreted as the outer surface of a coronal loop, with the horizontal (periodic) direction corresponding to the loop perimeter and the vertical to loop length, then one would expect the latter to be much larger than the former. In what follows we consider "typical" values for coronal loop lengths $L = 10^{10}\,\mathrm{cm}$ and diameter $D = 10^{8}\,\mathrm{cm}$, as listed in Golub & Pasachoff (1997). Note however that a 1:100 aspect ratio is probably too high if considering coronal loops at the small end of the observed size distribution (see Table 1 in [Aschwanden et al., 2002]).

An important issue is the interpretation to be attached to an increase in lattice size; in going from a 32×32 to a 128×128 lattice (say), are we increasing fourfold the length and diameter of the loop —the *Ansatz* we favor at this juncture,— or are we implying

that the loop is made of a greater number of finer strands that develop sharper kinks? Both interpretations are physically plausible, but have different consequences at the level of energetics. Recall (cf. Table 1) that for a fixed threshold angle Θ_c, the mean rate of energy release $\langle \eta \rangle$, *expressed in terms of initial lattice energy*, falls with lattice size; under the first *Ansatz*, and for a fixed magnetic field strength doubling the lattice size increases the initial lattice energy fourfold, so that in fact larger lattices/loops liberate more energy in absolute terms. Under the second interpretation, a loop made up of many finer strands liberates less energy than a loop of the same size but made of fewer, thicker strands, and there is no dependency of the energy release rate on physical loop size; these features, in our opinion, add up to a less-than-satisfactory picture of energy release in coronal loops, thus motivating our preference for the first interpretation.

2.5.2 Critical angle

Having ascribed linear dimensions to our pseudo-coronal loop, it becomes possible to translate the critical angle Θ_c on the unit lattice into a geometrical crossing angle between two strands of the coronal loop. For example, a critical threshold half-angle $\Theta_c/2 = 1.25\,\mathrm{rad}$ implies a horizontal-to-vertical internodal distance ratio of 3:1. With an assumed length-to-diameter ratio 100:1, and mapping the horizontal extent of the lattice onto the perimeter πD of a loop of diameter D, one finds a geometrically corrected critical angle $\Theta_c^* = 2\arctan(3\pi/100) \simeq 11°$, which is comparable to the 14° value estimated by Parker (1988), but notably smaller than the 40° value obtained in [Dahlburg et al., 2005]. Because we always increase lattice size by the same factor horizontally and vertically, increasing lattice size leaves this 'physical' critical angle value unaltered. The key point here is mostly that, for a reasonable choice of length-to-diameter ratio, we recover a reasonable figure for the critical angle at which reconnection sets in, i.e., it is neither extremely small nor extremely large.

2.5.3 Energetics

With our adopted values for a typical coronal loop length and diameter, and an assumed field strength $B_0 = 200\,\mathrm{G}$ everywhere within the loop, one readily finds that in physical units our basic energy unit, the initial lattice energy is $E_0 \simeq 10^{29}\,\mathrm{erg}$. Examination of Figure 2.7B reveals that total flare energy covers the range $10^{-6} \leq E_r/E_0 \leq 0.9$, which then translates into energy covering the range $10^{23} \leq E_r \leq 10^{29}\,\mathrm{erg}$. The lower bound is not far removed from Parker's estimate or nanoflare energy. Note that larger flare energies can be produced on larger lattices, under our favored interpretation that increasing lattice size amounts to increasing loop size, and therefore the total magnetic energy content of the lattice. However, a detailed scaling analysis of flare energy release for varying loop sizes would also require specifications of the scaling relationship between physical loop parameters (magnetic field strength, etc) with linear size. Such scaling relationships have been inferred observationally (e.g. Aschwanden & Aschwanden, 2007), but at this juncture we opt to defer to a subsequent paper such detailed comparison with specific flare observations.

2.6 Concluding remarks

In this paper we presented and discussed a new avalanche model of magnetic energy release by solar flares, based on an idealized representation of a coronal loop. Our model is a line-based 2D cellular automaton, driven by stretching of randomly chosen line subsections. We identify these lines with strands of magnetic flux collectively making up the coronal loop. Stability is defined in terms of the angle subtended by two (or more) strands at lattice sites where they cross. Recovery to stability is enforced by cut-splice-move sequences mimicking magnetic reconnection, designed to lower lattice energy and alter topological linkage between strands.

Our simulations show that this driven dissipative cellular automaton evolves to a SOC state, with energy release occurring in a spatially and temporally intermittent fashion through avalanche of reconnection events collectively spanning a wide range of sizes, from a single site to large fraction of the whole lattice. The probability distribution functions for avalanche size measures (total energy released, peak luminosity, duration) take the form of power-laws, with indices comparing favorably to observationally-inferred values. In particular, our power law exponent for the PDF of total energy release, $\alpha_E = 1.66$, falls within the one-sigma range of the recent observational determination $\alpha_E = 1.52 - 1.77$ of Aschwanden & Parnell (2002), which takes into account some of the temperature-related observational biases affecting the analysis of EUV and soft-X-Ray flare data. This is a robust result that does not involve the tuning of any adjustable model parameter. The various avalanche size measures also correlate with each other as power laws, and here again our model compares favorably with observations, significantly better, in fact, than other SOC avalanche models of solar flares relying on "classical" sandpile-like isotropic lattices. Our results also show that the numerical values of these assorted power-law indices are independent of lattice size and stability threshold values. This is strongly suggestive of a self-organized critical state and we rigorously prove that by a formal scaling analysis in Morales & Charbonneau 2008.

At the level of physical interpretation in the solar flare context, the model introduced herein offers a number of attractive features. First, the flux conservation constraint $\nabla \cdot \mathbf{B} = 0$ is satisfied by design; second, the avalanching process releases a significant fraction of the magnetic energy stored in the lattice; third, for reasonable values of coronal loop parameters (cf. §4.5), the energy released by avalanches in the model spans the range from nanoflares ($\sim 10^{23}$ erg) to $\sim 10^{29}$ erg. Fourth, when mapped back onto a coronal loop of typical dimensions, the threshold angle above which reconnection sets in is of the same order of magnitude as the theoretical estimates of Parker (1988) and numerical simulations of [Dahlburg et al., 2005]. On the other hand, the logarithmic slope

α_E of the probability distribution function of energy release is too low for nanoflares to dominate the energy release budget. Therefore, although the present model is a viable model for the statistics of flare energy release, in its present form it does not represent a viable statistical model for coronal heating by nanoflares.

There exist a number of obvious extension to the avalanche model presented herein. Generalizing the model to three spatial dimensions would add 'radial' structure to the pseudo-loop and, perhaps more importantly, allow the design of driving mechanism that would introduce a systematic sense of true twist within the lattice. At the level of comparison with observations, one particularly interesting avenue consists in mapping our pseudo-loop as a arching structure projected onto the plane of the sky, and investigate the statistical properties of projected avalanching areas. The probability distribution function of flaring areas is currently one of the major point of discrepancy between observations and LHMB-type avalanche models of solar flares ([McIntosh et al., 2002]). It will also be interesting to make use of the various observationally inferred scaling laws between loop length, diameter, field strength, etc. (e.g., [Aschwanden et al., 2000]; [Aschwanden & Aschwanden, 2008]), to investigate the flare/avalanche energy release budget in greater quantitative detail than the simple order-of-magnitude estimates presented in §4.5.

Bibliography

[Aschwanden & Aschwanden, 2008] Aschwanden, M. J. & Aschwanden, P. 2008, ApJ, **674**, 530

[Aschwanden & Aschwanden, 2008b] Aschwanden, M. J. & Aschwanden, P. 2008, ApJ, **674**, 544

[Aschwanden et al., 2000] Aschwanden, M. J., Tarbell, T. D., Nightingale, R. W., Schrijver, C. J., Title, A., Kankelborg, C. C., Martens, P., Warren, H. P. 2000, Astrophys. J., **535**, 1047

[Aschwanden & Parnell, 2002] Aschwanden, M. J. & Parnell, C. 2002, ApJ, **572**, 1048

[Aschwanden et al., 2002] Aschwanden, M. J., De Pontieu, B., Schrijver, C. J. & Title, A. M. 2002b, Solar Phys., **206**, 99

[Bak, 1996] Bak, P., 1996, *How nature works*, Springer/Copernicus, New York.

[Bélanger et al., 2007] Bélanger, E., Vincent, A., & Charbonneau, P. 2007, Solar Phys., **245** (1), 141

[Charbonneau et al., 2001] Charbonneau, P., McIntosh, W., Liu, H . & Bogdan, T.J. 2001, Solar Phys. **203**, 231

[Dahlburg et al., 2005] Dahlburg, R. B., Klimchuk, J. A., & Antiochos, S. K. 2005, ApJ, **622**, 1191

[Dennis, 1985] Dennis, B. R. 1985, Solar Phys.,**100**, 465

[Georgulis & Vlahos, 1996] Georgoulis, M. K. & Vlahos, L. 1996, ApJ, 469, L135

[Georgulis & Vlahos, 1998] Georgoulis, M. K., & Vlahos, L. 1998, A&A, 336, 721

[Georgulis et al., 2001] Georgoulis, M. K., Vilmer, N. & Crosby, N. B. 2001, A&A, **367**, 326

[Isliker, Anastasiadis & Vlahos, 2000] Isliker, H., Anastasiadis, A. & Vlahos, L. 2000, A & A, **363**, 1134

[Isliker et al., 1998] Isliker, H., Anastasiadis, A., Vassddialiadis, D. & Vlahos, L. 1998, A & A, **335**, 1085

[Isliker et al., 2001] Isliker, H., Anastasiadis, A., & Vlahos, L. 2001, A&A, 377, 1068

[Jensen, 1998] Jensen, H. J. 1998, Self-organized criticality (Cambridge: Cambridge University Press)

[Kadanoff et al., 1989] Kadanoff, L. P., Nagel, S. R., Wu, L., & Zhou, S. 1989, PRA, **39**, 6524

[Klimchuk, 2007] Klimchuk, J.A. 2006, Solar Phys., **234**, 41

[Liu et al., 2002] Liu, H.-L., Charbonneau, P., Pouquet, A., Bogdan, T. J., & McIntosh, S. W. 2002, Phys. Rev. Lett., **66**, 056111

[Lu, 1995] Lu, E. T. 1995, ApJ, **446**, 109

[Lu & Hamilton, 1991] Lu, E. T and Hamilton, R. J. 1991, Astrophys. J., **380**, L89

[Lu et al., 1993] Lu, E. T., Hamilton, R. J., McTiernan, J. M. and Bromund, K. R. 1993, Astrophys. J., **412**, 841

[McIntosh et al., 2002] McIntosh, S. W, Charbonneau, P., Bogdan, T. J, Liu, H.-L., & Norman, J. P. 2002, Phys. Rev. E, **65**, 46125.

[Norman et al., 2001] Norman, J. P., Charbonneau, P., McIntosh, S. W., and Liu, H.-L. 2001, ApJ, **557**, 891

[Parker, 1983] Parker, E. N. 1983, Astrophys. J., **264**, 642.

[Parker, 1988] Parker, E. N. 1988, Astrophys. J., **330**, 474.

[Parker, 1994] Parker, E. N. 1994, Spontaneus current sheets in magnetic Fields (Oxford University Press, New York)

[Veronig et al., 2002] Veronig, A., Temmer, M., Hanslmeier, A., Otruba, W. & Messerotti, M. 2002, A&A, **382**, 1070

[Warren & Warshall, 2001] Warren, H. P. & Warshall, A. D. 2001, ApJ, **560**, L87

[Wheatland, 2000] Wheatland, M. S. 2000, ApJL, **536**, L109

[Yang et al., 2006] Yang, S., Gan, W. Q., Li, Y. P. 2006, Solar Phys., 238 (1), 61

[Yashiro et al., 2006] Yashiro, S., Akiyama, S., Gopalswamy, N. & Howard, R. A. 2006, ApJ, 650

[Zirker & Cleveland, 1993] Zirker, J. B. & Cleveland, F. M, 1993, Solar Phys., **145**, 119

Chapter 3

Scaling laws and frequency distributions of avalanche areas in a SOC model of solar flares

Laura F. Morales & Paul Charbonneau

Département de Physique, Université de Montréal,

C.P. 6128 Succ. Centre-ville, Montréal, Qc, H3C-3J7 CANADA

Received 5 November 2007; accepted 17 January 2008; published 26 February 2008

Published in: *Geophysical Research Letters*, Volume 35, Issue 4, CiteID L04108

3.1 Abstract

We calculate the spreading exponents and some geometrical properties of avalanches in a novel avalanche model of solar flares, closely built on Parker's physical picture of coronal heating by nanoflares. The model is based on an idealized representation of a coronal loop as a bundle of magnetic flux strands wrapping around one another, numerically implemented as an anisotropic cellular automaton. We demonstrate that the growth of avalanches in this model exhibits power-laws correlations that are numerically consistent with the behavior of a general class of statistical physical systems in the vicinity of a stationary critical point. This demonstrates that the model indeed operates in a self-organized critical regime. Moreover, we find that the frequency distribution of avalanche peak areas A assumes a power-law form $f(A) \propto A^{-\alpha_A}$ with an index $\alpha_A \simeq 2.45$, in excellent agreement with observationally-inferred values, unlike other extant sandpile-like avalanche models of solar flares.

3.2 Introduction

Solar flares are the observational manifestation of spatially and temporally intermittent release of magnetic energy in the lower solar corona. The flaring process, most likely mediated by fast magnetic reconnection, is accompanied by the acceleration of energetic particles and a rapid rise of emission at the short wavelengths ($\leq 2000\,\text{Å}$) of the electromagnetic spectrum. This is most spectacular and readily observed in the extreme ultraviolet (euv) and x-ray domains. Systematic studies from space-borne platforms have revealed that the frequency distributions of size measures of solar flares is well described by power laws, spanning eight orders of magnitude in the case of flare energy E, i.e.,

$$f(E) = f_0\, E^{-\alpha_E}, \qquad 10^{25} \leq E \leq 10^{33}\,\text{erg}\ , \tag{3.1}$$

with $\alpha_E = 1.55 - 1.67$ for flare observations ranging from UV to XRays (see [Aschwanden & Parnell, 2002]). similar power laws are obtained for the peak energy flux, and flare duration (T) (see [Aschwanden et al., 2000], and references therein).

Because of their intrinsic spatial and temporal self-similarity, avalanche models provide an attractive explanatory framework for these observed power laws in flare parameters ([Lu & Hamilton, 1991], [Lu et al., 1993], [Vlahos et al., 1995], [Charbonneau et al., 2001]; and references therein). The main idea beneath these models is that solar flares are the collective manifestation of energy released by avalanches of small-scale reconnection events, cascading through coronal magnetic field structures mechanically stressed by stochastic motions of their photospheric footpoints forced by turbulent convective fluid motions. This physical picture, originally put forth in the context of coronal heating ([Parker, 1983]), includes all the ingredients believed necessary to lead to self-organized criticality (hereafter SOC; [Bak, 1996], [Jensen, 1998]): an open system (coronal loop) slowly driven by an external energy source (footpoint motions), and subject to a self-stabilizing local threshold instability (magnetic reconnection).

To this day, most extant avalanche models for solar flares are sandpile-like, using threshold conditions and redistribution rules inspired by the pioneering work of [Lu & Hamilton, 1991] (for a basic introduction to see [Charbonneau et al., 2001]; and for examples of models that do depart from the sandpile Ansatz, see, e.g., [Zirker & Cleveland, 1993], [Hughes et al(2003)]). Such models do succeed in producing flare size distributions having the form of power laws, with indices comparing reasonably well with observationally inferred values. However, they have proven notoriously difficult to link back to the magnetohydrodynamical equations known to ultimately describe the flaring phenomenon ([Isliker, Anastasiadis & Vlahos, 2000], [Isliker et al, 1998]).

We have recently designed a novel avalanche model of solar flares, using magnetic field lines as a basic dynamical element ([Morales & Charbonneau, 2008a]). The model

is cellular automaton-like, in that it is defined over a discrete lattice and the evolution of nodal values are rule-based. We consider an idealized representation of the outer surface of a straightened coronal loop, consisting in a 2 D lattice of size $N \times N$ on which is defined a network of vertically interconnected nodes with periodic boundary conditions in the horizontal direction. Each vertical line so defined represents a magnetic flux strand (or tube), i.e., a bundle of magnetic fieldlines behaving as a coherent entity. The system is driven by introducing horizontal displacements at randomly selected nodes, mimicking the effects of random footpoint displacements. The inexorable lengthening of the flux strands produced by such successive displacements amounts to pumping energy into the lattice. This driving mechanism will eventually cause two or more flux strands to "cross" at certain lattice sites; we use the angle Θ subtended by such crossing strands as a stability criterion ([Parker, 1988]; [Dahlburg et al., 2005]); whenever Θ exceeds some preset value Θ_c, we cut-and-splice the two flux strands and displace one of the two nodes away from the unstable site, in a manner such as to lower magnetic energy. This, in turn, can create new unstable crossing angles at neighboring lattice sites, which are then themselves spliced and displaced, and so on in classical avalanching style. As with most SOC sandpile models, driving is suspended during avalanches, corresponding to a separation of timescales between photospheric driving (24 hs) and avalanching (typical duration of a flares is of the order of tenth of second to tenth of minutes).

In [Morales & Charbonneau, 2008a] we showed that such a strongly anisotropic model does produce spatially and temporally intermittent, avalanche-like release of magnetic energy (see Fig. 3.1), with frequency distributions of avalanche size parameters in the form of power laws with indices comparing to observationally inferred values at least as well as earlier isotropic sandpile-like models. Moreover, and unlike in most of these models, avalanches now release a significant fraction of the total energy stored in the lattice. Thus, assuming that our model represents a typical coronal loop of magnetic field strenth of $B_0 = 200G$ the release energy ranges between 10^{23} and 10^{30} erg.

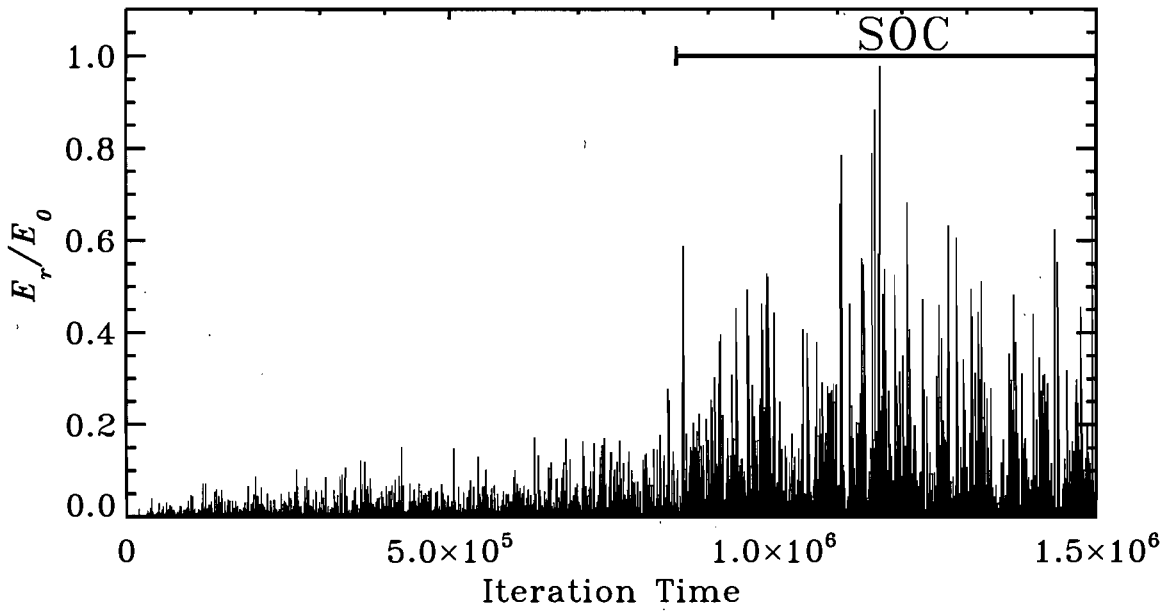

Figure 3.1: A representative time series of energy release E_r, as produced by our avalanche model running on a 128 × 128 lattice with $\Theta_c = 2.5\,\mathrm{rad}$. Energy release is expressed in units of the initial lattice energy E_0. The simulation begins with vertical parallel flux strands, and reaches the SOC at $\sim 8.5 \times 10^5$ iterations, at which time a fairly abrupt increase in the mean size of avalanches is observed.

In the present paper we focus on geometrical properties of avalanches in the [Morales & Charbonneau, 2008a] model. Specifically, we compute the critical exponents linking geometrical properties to the underlying avalanche dynamics (§2), and show that these exponents satisfy the mutual numerical relationships expected of systems in a SOC state. We then show that the associated frequency distribution of avalanching/flaring areas compares much better with observations than that associated with earlier avalanche models (§3). This fixes what, up to now, remained arguably the most glaring discrepancy between flare observations and SOC avalanche models of solar flares ([McIntosh et al., 2002]; [Aschwanden & Parnell, 2002]).

3.3 Dynamical properties of the SOC model

When SOC systems arrive in the vicinity of a critical state, they exhibit a number of scaling laws that characterize their dynamical properties. Let t be the time, measured in iterations, since the beginning of a given avalanche. Define $n(t)$ to be the ensemble-averaged number of active lattice sites at t, and $p(t)$ the ensemble-reconstructed survival probability that an avalanche lasts up to t; these two quantities are expected to scale with t as power laws:

$$n(t) \sim t^{\eta} , \qquad p(t) \sim t^{\delta} , \tag{3.2}$$

η and δ being the so-called spreading exponents ([Muñoz et al., 1999]). This implies that the total number of active sites having a lifetime T scales as $n_s \sim T^{\eta+\delta}$, and therefore its time integral should be characterized by the exponent:

$$\kappa = 1 + \eta + \delta . \tag{3.3}$$

If all of these various scaling relationships indeed hold, then the size (S) of an avalanche, defined as the total number of toppling events, scales with its lifetime T as:

$$\mathbf{S(T) \sim T^{\kappa}} \ . \tag{3.4}$$

Another spreading exponent characterizes the probability distribution of avalanche sizes: $P(S) = S^{-\beta}$. The index β can be computed in terms of η and δ. Given that an avalanche of size S can have different durations T (since s and t are only statistically correlated), the probability of an avalanche reaching size s before ending is:

$$P(s) = \int_{t_{min}}^{t_{max}} P(s|t)\,(1 - t^{-\delta})\mathrm{d}t \tag{3.5}$$

where t_{min} and t_{max} are the upper and lower duration bounds of size-s avalanches, and $P(s|t)$ is the conditional probability of an avalanche having reached size s at time t since onset. Since $P(s|t)$ is bell-shaped and peaks at $t \sim 1/s^{1+\eta+\delta}$ one can show (see [Muñoz et al., 1999]) that $P(s)$ scales as:

$$P(s) \propto s^{-\beta} \ , \qquad \beta = \frac{1 + \eta + 2\delta}{1 + \eta + \delta} \ , \tag{3.6}$$

with, therefore, the same scaling expected for $P(S)$.

Working off the energy release time series produced by our SOC model of solar flares (viz. Fig. 3.1), it is straightforward to identify individual avalanches, and for each measure their size, duration, etc. From the ensemble of all avalanches occurring in a given simulation it is then possible to compute the size, duration, survival probabilities $p(t)$ and growth measure $n(t)$. These various quantities are indeed found to be related by well-defined power laws, usually spanning many orders of magnitude. One example is shown in Figure 3.2, for the size-duration correlation. The relationship is really statistical, but nonetheless quite tight except for the smaller avalanches, where deviation from power-law behavior is apparent. This is quite typical, and simply reflects the fact that smaller avalanches are more severely constrained by the discrete nature of the

Table 3.1: Spreading exponents

Simulation	N	Θ_c(rad)	η	δ
B1	64		0.10 ± 0.03	1.29 ± 0.1
B2	64	2.25	0.09 ± 0.03	1.18 ± 0.1
B3	64	2.5	0.12 ± 0.03	1.30 ± 0.1
C1	128	2	0.10 ± 0.02	1.26 ± 0.1
C2	128	2.25	0.12 ± 0.02	1.25 ± 0.1
C3	128	2.5	0.12 ± 0.02	1.1 ± 0.08

lattice. From this and equivalent plots for other quantities, we then compute, by least-squares fits, the numerical values for the exponents η, δ, κ and β. The resulting values are listed in Table 1, for a set of simulations performed using different lattice sizes and threshold angles. In all cases these fits were carried out excluding avalanches with duration $T \leq 40$ iterations, as per the aforementioned large dispersion in the correlation plots associated with the smaller avalanches.

The first important thing to note on Table 1 is that there is no significant difference between the values of the spreading exponents obtained for a variety of lattice sizes and critical angles. The key check on the SOC nature of the model is to now calculate, via eqs. (3.3) and (3.6), the *expected* values of κ and β, given the values for η and δ extracted from the simulation results. These are listed in the two rightmost columns of Table 1. This comparison is quite good in the case of β, but for κ the measured values are systematically lower than the computed $1 + \eta + \delta$. Admittedly, redistribution at unstable sites is a more complex affair in our model than in classical sandpile models, so it is not clear a priori that the total number of toppling events S is the optimal measure of avalanche size. To guard against this potential problem, we recomputed the above correlation using instead the energy (E) released by avalanches as a size measure. The κ values extracted from correlation plots between E and T (see figure 8B

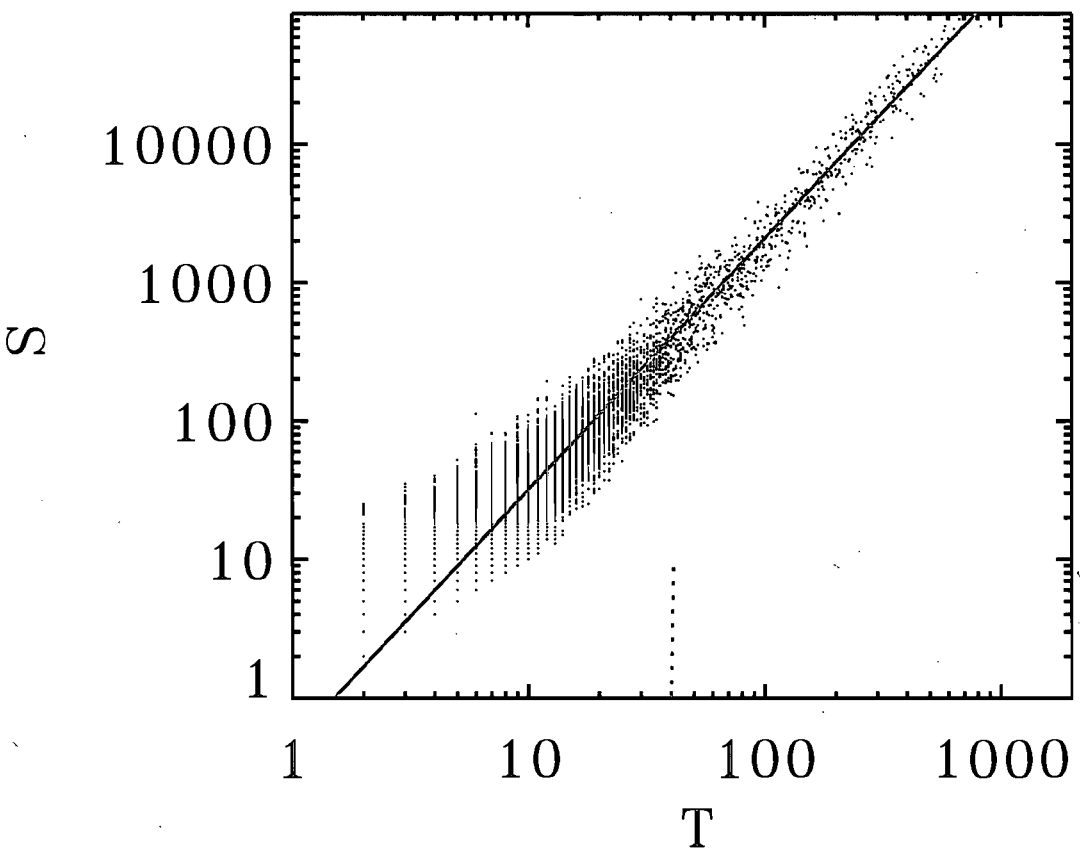

Figure 3.2: Correlation plot of avalanche sizes (S) vs lifetimes (T) for a simulation on a 128×128 lattice and $\Theta_c = 2.5$ rad. The gray line is a least-squares fit, computed using only avalanches with lifetime $T > 40$ iterations.

Table 3.2: Spreading exponents (continuation)

Sim.	$\kappa_{T\geq 10}$	$\kappa_{T\geq 40}$	$1+\eta+\delta \equiv \kappa$	$\beta_{T\geq 10}$	β_{Tge40}	$\frac{1+\eta+2\delta}{1+\eta+\delta} \equiv \beta$
B1	1.70 ± 0.4	1.84 ± 0.30	1.66 ± 0.1	1.51 ± 0.1	2.39 ± 0.13	1.54 ± 0.01
B2	1.77 ± 0.4	1.87 ± 0.30	1.47 ± 0.1	1.48 ± 0.1	2.26 ± 0.13	1.53 ± 0.01
B3	1.64 ± 0.4	2.03 ± 0.31	1.74 ± 0.2	1.75 ± 0.2	2.42 ± 0.13	1.54 ± 0.01
C1	1.78 ± 0.3	2.00 ± 0.30	1.72 ± 0.2	1.60 ± 0.2	2.36 ± 0.12	1.53 ± 0.02
C2	1.84 ± 0.3	1.82 ± 0.30	1.67 ± 0.2	1.80 ± 0.2	2.37 ± 0.10	1.53 ± 0.01
C3	1.83 ± 0.3	1.88 ± 0.25	1.79 ± 0.2	1.60 ± 0.2	2.19 ± 0.10	1.48 ± 0.01

in [Morales & Charbonneau, 2008a]) turn out quite similar to those listed in Table 1. In this case the magnetic energy can be related to the length of the strands by means of the mass and flux conservation. $B' = B \times l'/l$ and thus $E \sim l^2$. The energy released by the lattice is then calculated by the difference between the magnetic energy before and after the redistribution. At any rate, for most lattices sizes and threshold angles the κ values at least fall within the one-sigma error bounds associated with the fits. Given the aforementioned ambiguity in defining avalanche size, we conclude that avalanches in our model of solar flares do behave as expected of avalanches in a SOC system.

3.4 Geometrical properties

We now turn to a purely geometrical property of the avalanches produced by our SOC model, namely the area of avalanches. Although previous avalanche models of solar flares did succeed in producing power laws in areas, the associated index turned out much smaller than observationally-inferred values (see, e.g., [McIntosh et al., 2002]). In keeping with prior practice, we consider the following two (related) measures of avalanche area: The total number of lattice nodes having avalanched at least once

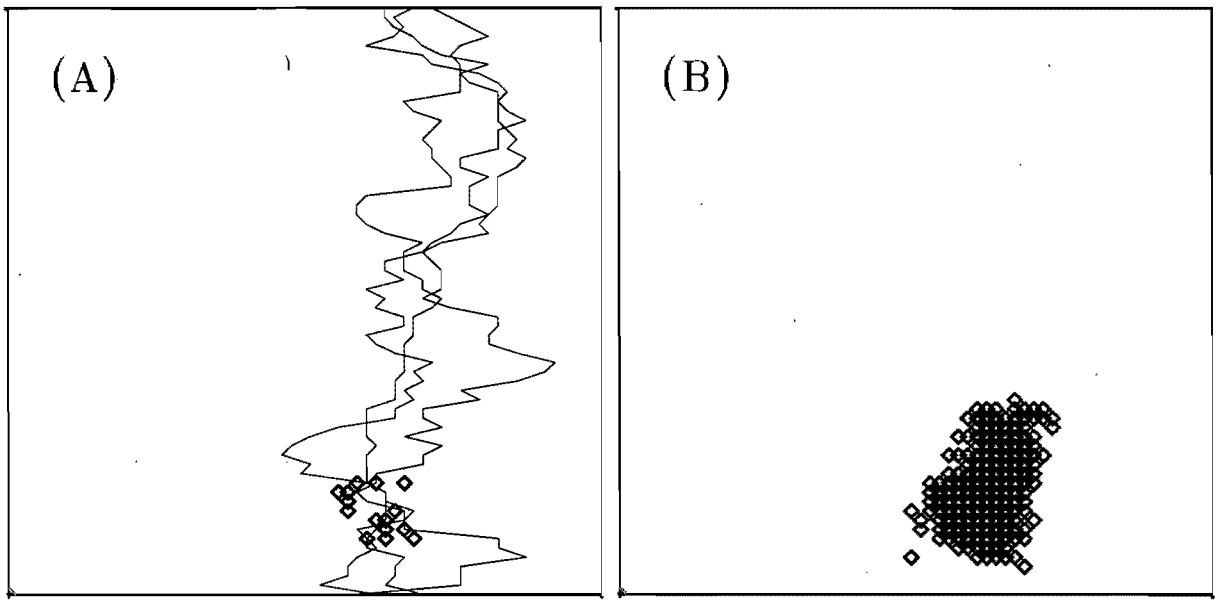

Figure 3.3: The spatial structure of a moderately large avalanche ($T = 135$) on a two-dimensional 64×64 lattice with $\Theta_c = 2.5$. Panel (A) is a view of the lattice plane, showing the spatial distribution of unstable nodes **(diamonds)** at the time of peak energy release ($A = 20$ nodes). Also the position of three representative 'active' flux strands are plotted showing that at this point of the simulation each flux strand is far from the initial tidy condition. Panel (B) shows the equivalent distribution for all nodes having gone unstable at least once in the course of that avalanche, yielding the time-integrated area $A^* = 1142$.

during the course of a given avalanche, A^*; and the total number of unstable nodes at the time of peak energy release, A. As exemplified on Figure 3.3, these can be quite different, especially for the larger avalanches. A^* represents what would be observed by an instrument with low temporal cadence, while A would only be visible to an instrument with a very high cadence. Thus A and A^* conveniently bracket the range of observational possibilities.

As exemplified on Figure 4.3 for a simulation on a $N = 128$ lattice with $\Theta_c = 2$, both A and A^* are found to have frequency distributions taking the form of power-laws. The

Table 3.3: Simulations parameters and global results

Simulation	N	Θ_c(rad)	α_A^*	α_A
B1	64	2	1.83 ± 0.07	2.45 ± 0.15
B2	64	2.25	1.82 ± 0.05	2.53 ± 0.15
B3	64	2.5	1.93 ± 0.07	2.41 ± 0.15
C1	128	2	1.81 ± 0.07	2.53 ± 0.16
C2	128	2.25	1.93 ± 0.07	2.45 ± 0.11
C3	128	2.5	1.77 ± 0.07	2.20 ± 0.17
LH-2D	64	N/A	0.52 ± 0.03	1.05 ± 0.07
LH-2D	128	N/A	0.55 ± 0.02	1.02 ± 0.06
LH-3D	64	N/A	0.49 ± 0.04	1.04 ± 0.04

associated indices, α_A and α_A^*, are listed in Table 2 for varying simulation parameters. Once again no systematic, significant variations are found as a function of N or Θ_c. The corresponding values for two versions of the [Lu & Hamilton, 1991] avalanche models, taken from [McIntosh et al., 2002] are listed at the bottom of the table, for comparison purposes.

Recent observational determinations **of** $f(A) \sim A^{-\alpha_A}$ ([Aschwanden & Parnell, 2002]) yield power-law indices that depend to some extent on the dataset being used, with α_A ranging from 2.45 for EUV-TRACE observations, down to 1.86 for Yohkoh SXR data. These values are much higher than those obtained in isotropic sandpile-like SOC models of flares, but are in much better agreement with results from the present model (cf. Table 2).

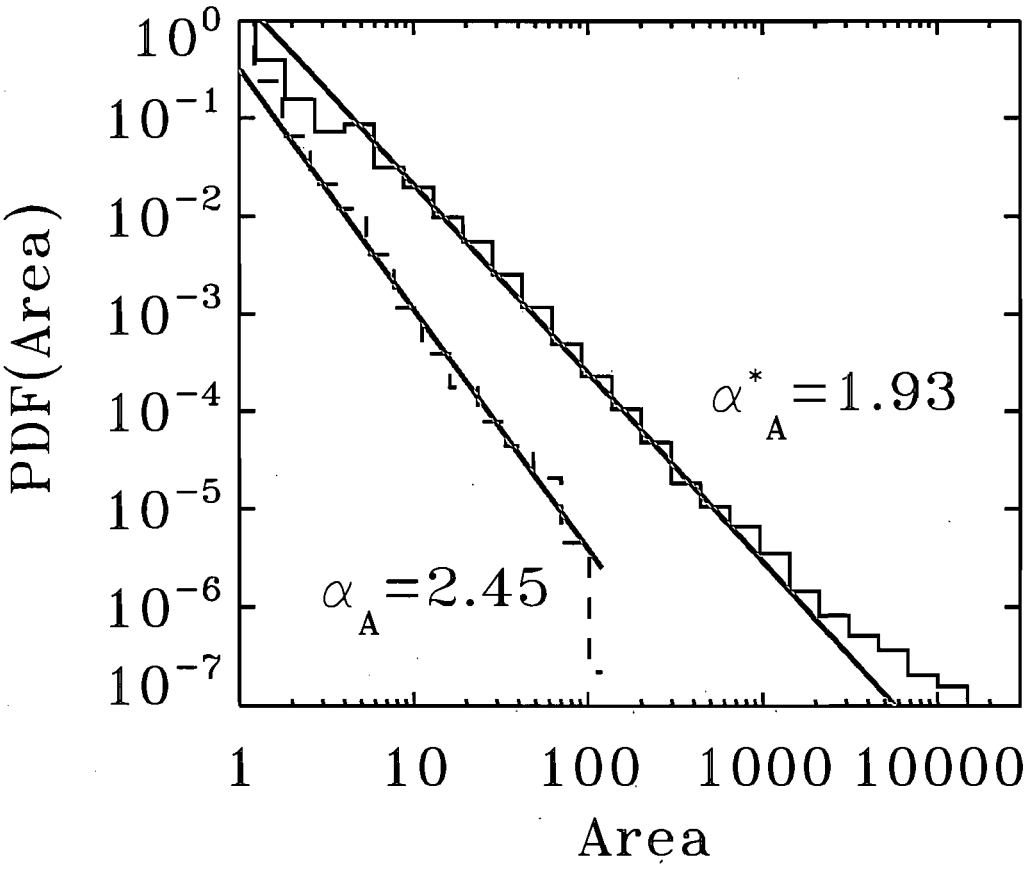

Figure 3.4: Frequency distribution for peak and integrated avalanche areas, for a simulation on a 128×128 lattice and $\Theta_c = 2.25$ rad. Both area measured are well-fitted by power-laws.

3.5 Conclusions

In [Morales & Charbonneau, 2008a], we have proposed a new SOC model for solar flares, readily amenable to physical interpretation in terms of the physical picture of photospherically-forced coronal loops originally put forth by [Parker, 1983] in the context of the coronal heating problem. We have demonstrated here that the growth of avalanches in this model does exhibit the dynamical scaling relations characteristic of critical behavior. We have also calculated the so-called spreading exponents η and δ and verified that they satisfy the mutual numerical relationship expected from SOC systems. Based on these results we can conclude that the [Morales & Charbonneau, 2008a] avalanche model for solar flares is indeed a *bona fide* instance of a self-organized critical system.

To the best of our knowledge, there have been no attempts at determining the spreading exponents associated with observations of solar flares. This has been carried out successfully in other physical settings, notably for auroral emission (see [Uritsky & Klimas, 2004], [Uritsky et al., 2001]), where it has proven a useful comparison point between models and observations. The quality of current spatially and temporally resolved flare observations should allow a similar comparison to be made in the context of solar flares.

We also showed that the [Morales & Charbonneau, 2008a] model succeeds in correcting what, up to now, had remained arguably the most serious discrepancy between flare observations and prediction from isotropic sandpile-like avalanche models, namely the power-law index of the frequency distributions for flaring areas. This suggests that the present model should be ideally suited to push further the detailed comparison with high-cadence, high-resolution flare observations obtained by space-borne instruments such as TRACE. In particular, proper account should be made for projection effects, differential emission measure, and variations in loop lengths. The one-to-one

geometric correspondence between our anisotropic lattice and actual coronal loop make these tasks quite feasible within the context of our model.

At a more general level, our results strengthens the case for the existence of self-organized criticality in the solar corona. Indeed, with flare energy release spanning over eight orders of magnitude in energy, and with a sound physical underpinning to the model, we can legitimately argue that solar flares represent one of the most convincing case for SOC in a natural physical system (on this point, see [Lu (1995)]).

Bibliography

[Aschwanden et al. (2000)] Aschwanden, M. J., Tarbell, T. D., Nightingale, R. W., Schrijver, C. J., Title, A., Kankelborg, C. C., Martens, P., & Warren, H. P. (2000), Time Variability of the "Quiet" Sun Observed with TRACE. II. Physical Parameters, Temperature Evolution, and Energetics of Extreme-Ultraviolet Nanoflares, *ApJ*, *535*, 1047-1065.

[Aschwanden & Parnell (2002)] Aschwanden, M. J & Parnell, C. E. (2002), Nanoflare Statistics from First Principles: Fractal Geometry and Temperature Synthesis, *ApJ*, *572*, 1048-1071.

[Bak et al. (1987)] Bak, P., Tang, C., & Wiesenfeld, K. (1987), Self-organized criticality, *Phys. Revi. Lett*, *59*, 381-384.

[Charbonneau et al. (2001)] Charbonneau, P., McIntosh, S. W., Liu, H.-L., & Bogdan, T. J. (2001), Avalanche models for solar flares (Invited Review), *Sol. Phys*, *203*, 321-354.

[Dahlburg et al. (2005)] Dahlburg, R. B., Klimchuk, J. A., & Antiochos, S. K. (2005), An Explanation for the "Switch-On" Nature of Magnetic Energy Release and Its Application to Coronal Heating, *ApJ*, 622, 1191-1201.

[Hughes et al. (2003)] Hughes, D., Paczuki, M., Dendy, R. O., Helander, P. & McClements, K. G. (2003), Solar Flares as Cascades of Reconnecting Magnetic Loops, *Phys. Rev. Lett.*, *90*, 131101.

[Isliker et al. (2000)] Isliker, H., Anastasiadis, A., & Vlahos, L. (2000), MHD consistent cellular automata (CA) models. I. Basic features, *A&A*, *363*, 1134-1144.

[Isliker et al. (1998)] Isliker, H., Anastasiadis, A., Vassiliadis, D., & Vlahos, L. (1998), Solar flare cellular automata interpreted as discretized MHD equations *A&A*, *335*, 1085-1092.

[Jensen (1998)] Jensen, H. J. (1998), *Self-organized criticality*, Cambridge University Press, Cambridge.

[Lu (1995)] Lu, E. T. (1995), The Statistical Physics of Solar Active Regions and the Fundamental Nature of Solar Flares, *ApJ*, *446*, 109.

[Lu & Hamilton (1991)] Lu, E. T., & Hamilton, R. J. (1991), Avalanches and the distribution of solar flares, *ApJ*, *380*, 89-92.

[Lu et al. (1993)] Lu, E. T., Hamilton, R. J., McTiernan, J. M., & Bromund, K. R. (1993), Solar flares and avalanches in driven dissipative systems, *ApJ*, *412*, 841-852.

[McIntosh et al. (2002)] McIntosh, S. W, Charbonneau, P., Bogdan, T. J, Liu, H.-L., & Norman, J. P. (2002), Geometrical properties of avalanches in self-organized critical models of solar flares, *Phys. Rev. E*, *65*, 46125.

[Morales & Charbonneau (2007)] Morales, L. F. & Charbonneau, P. 2007, Self-Organized Critical model of energy release in an idealized coronal loop, *ApJ*, submitted.

[Muñoz et al. (1999)] Muñoz, M. A., Dickman, R., Vespignani, A. and Zapperi, S. (1999), Avalanche and spreading exponents in systems with absorbing states, *Phys. Rev. E*, *59* (5), 6175-6178.

[Parker (1983)] Parker, E. N. (1983), Magnetic neutral sheets in evolving fields. *ApJ*, *264*, 635-647.

[Parker (1988)] Parker, E. N. (1988), Nanoflares and the solar X-ray corona, *ApJ*, *330*, 474-479.

[Uritsky et al. (2001)] Uritsky, V. M., Klimas, A. J. & Vassiliadis, D. (2001), Comparative study od dynamical critical scaling in the auroral electrojet index versus solar wind fluctuations, *Geophys. Res. Lett.*, *28* 3809-3812.

[Uritsky & Klimas (2004)] Uritsky, V., M. & Klimas, A. J. (2004), Scaling and predictability of complex geospace disturbances, Substorms-7, Proceedings of the 7th International Conference on Substorms.

[Vlahos et al. (1995)] Vlahos, L., Georgoulis, M., Kluiving, R., and Paschos, P. (1995), The statistical flare, *A&A*, *299*, 897.

[Zirker & Cleveland (1993)] Zirker, J. B. & Cleveland, F. M, (1993), Avalanche models of active region heating and flaring *Sol. Phys.*, *145*, 119-128.

This work was supported by the Natural Sciences and Engineering Research Council Canada and by the Fonds Québécois de Recherche sur la Nature et les Technologies.

Chapter 4

Geometrical properties of avalanches in a pseudo-3D coronal loop

Laura F. Morales & Paul Charbonneau

Département de Physique, Université de Montréal,

C.P. 6128 Succ. Centre-ville, Montréal, Qc, H3C-3J7 CANADA

Submitted to: *The Astrophysical Journal*

4.1 Abstract

We investigate the geometrical properties of energy release of synthetic coronal loops constructed using a recently published self-organized critical avalanche model of solar flares. The model is based on an idealized representation of a coronal loop as a bundle of closely-packed magnetic flux strands wrapping around one another in response to photospheric fluid motions, much as in Parker's nanoflare model. Simulations were performed with a 2D-cellular automaton that satisfies the constraints $\nabla \cdot \mathbf{B} = 0$ by design. We transform the avalanching nodes produced by simulations into synthetic flare images by converting the 2D lattice into a bent cylindrical loop that is projected onto the plane of the sky. We then studied the statistical properties of avalanches peak snapshots and time-integrated avalanches occurring in these synthetic coronal loops. We found that the frequency distribution of avalanche peak areas A assumes a power-law form $f(A) \propto A^{-\alpha_A}$ with an index $\alpha_A \simeq 2.37$, in excellent agreement with observationally-inferred values and reducing error bars from previous works. We also measured the area fractal dimension D of avalanches produced by our simulations using the box counting method, which yields $1.17 \leq D \leq 1.24$, a result falling nicely within the range of observational determinations.

4.2 Introduction

In the last three decades a large amount of observational evidence have supported the idea that solar flares are generated by the storage and sudden, dynamical release of magnetic energy occurring in the solar atmosphere and lower corona. The very short observed timescales for flare onset point to magnetic reconnection as the most likely viable physical mechanism to convert magnetic energy to heat, although detailed quantitative models are still in the making.

Because the sun's atmosphere is characterized by a high electrical conductivity, the stressing of magnetic field by fluid motions can press together magnetic flux surfaces of different magnetic orientations, and lead to the formation of electrical current sheets (e.g. [Parker, 1988]). As the currents build up, magnetic reconnection sets in and causes a local topological reconfiguration and dissipation of the magnetic field within the current sheets. The many such currents sheets continuously undergoing reconnection everywhere in the corona power what amounts to a large number of very small flares. [Parker (1988)] estimated the energy release of one such elementary reconnection event at $\sim 10^{24}$ erg (and thus dubbed them "nanoflares"). In Parker's picture, stochastic photospheric fluid motions of convective origin shuffle the footpoints of magnetic coronal loops. With the frozen-in condition applicable within the loop to all but the very smallest spatial scales, in the low plasma-β characteristic of the corona the subsequent dynamical relaxation within the loop results in a complex tangled magnetic field essentially force-free everywhere except in numerous tangential discontinuities where strong current sheets build up and reconnection can set in.

On the observational front, numerous attempts have been made to verify of falsify Parker's nanoflare conjecture, and more specifically to extent flare observations, and determine distributions functions of their properties, all the way down to the nanoflare regime. One of the most remarkable observational facts derived from observed flare statistics is that the frequency distribution of the energy release takes the form of a tight power law spanning at least eight orders of magnitude in flare energy (see, e.g., [Dennis (1985)]; [Aschwanden et al., 2000]), indicative of self-similarity in the flaring process.

Motivated in part by this idea, Lu and Hamilton ([Lu & Hamilton, 1991]) developed the first avalanching sandpile model of flaring active regions, which later gave rise to numerous variations on the same theme ([Lu & Hamilton, 1991], [Lu et al., 1993], [Georgulis & Vlahos, 1996], [Georgulis & Vlahos, 1998] and [Charbonneau et al., 2001]). All these models share common features, notably the fact that they are cellular-automaton-

like, i.e., their spatiotemporal evolution is governed by discrete, simple local stability and redistribution rules. They all produce power-law distribution of avalanche energy, in many cases with logarithmic slopes comparing favorably to observations (see [Charbonneau et al., 2001] for a review). However, all these models suffer from the same fundamental drawback, namely the difficulty in linking back in an unambiguous and quantitative manner their internal rules to the physical laws governing the evolution of coronal magnetic fields, namely magnetohydrodynamics.

In a recent paper [Morales & Charbonneau, 2008a] we presented a novel avalanche model of solar flares, using magnetic field lines as a basic dynamical element. While still cellular-automaton-like in its use of local, discrete stability and redistribution rules, this model (1) can be unambiguously mapped onto a coronal loop, (2) allows the quantitative calculation of energy release in physical units, and (3) ensures by its very design that $\nabla \cdot \mathbf{B} = 0$. Our simulations showed that this driven dissipative cellular automaton evolves to a SOC state with avalanche of reconnection events collectively spanning a wide range of sizes and with frequency distribution of size parameters comparing to observations at least as well as earlier sandpile models.

Comparisons between geometrical properties of avalanches and flare observations at high spatial and temporal resolution are not abundant in the literature ([McIntosh et al. (2002)], [McIntosh et al. (2001)], [Morales & Charbonneau, 2008b], [Aschwanden & Aschwanden, 2008b] and [Uritsky et al. (2007)]). Nevertheless, all of them agree in suggesting that geometrical assumptions made in reconstructing the flaring volume from areas observed in the plane of the sky play a critical role when calculating the energy released by individual flares. Consequently, in this paper we investigate the geometrical properties of avalanches in our new SOC model for solar flares. To do this we reconstruct the cylindrical geometry of the coronal loop and study the geometrical properties and associated statistical distributions of projected avalanche areas.

In the following section we briefly review the design and operation of our recent SOC model for solar flares, and define the various geometrical measures to be used in what follows. In section 3 we describe the sequence of transformation steps required to map our 2D simulations results onto 3D-loop-like structures, which then allows us to synthetize pseudo-flare observations. Sections 4 and 5 are devoted to study the geometrical properties of projected avalanches. In section 4 we calculate frequency distributions of flaring areas and in section 5 we compute the fractal dimension of our synthetic solar flares by means of a box counting method. We summarize our results and conclude in section 6.

4.3 The strand-based model for solar flares

In this section we summarize the conceptually novel SOC model for solar flares we have recently developed. For full details concerning the model, implementation and numerical simulations, see [Morales & Charbonneau, 2008a].

The model is a basically an anisotropic cellular automaton that uses magnetic field lines as the main dynamical element. We define a 2D regular cartesian lattice of size $N \times N$ as an idealized representation of the outer surface of a straightened coronal loop. On this lattice we define a network of vertically interconnected nodes with periodic boundary conditions in the horizontal direction. Each vertical line so defined represents a magnetic flux strand (or tube), i.e., a bundle of magnetic fieldlines behaving as a coherent entity. Driving is introduced in the form of sequential, horizontal displacements (with non-zero mean) at randomly selected single nodes, mimicking the effects of random photospheric footpoint displacements propagating within the loop. Over time each node thus ends up executing a form of biased random walk, which inexorably leads to an increase in the length of the flux strands, which, via mass and flux conservation within each strand, leads to an increase in the magnetic energy content

of the strand. Consequently, the total magnetic energy collectively stored within all strands defines the lattice energy.

After many steps of this driving process, there will also inevitably come a point where two or more flux strands "cross" at certain lattice site, jointly subtending an angle hereafter denoted Θ. We use the value of this angle as a stability criterion, as suggested by theoretical considerations ([Parker (1988)]), which have recently found support in numerical simulations ([Dahlburg et al. (2005)]); whenever Θ exceeds some preset threshold Θ_c, we cut-and-splice the two flux strands and displace one of the two nodes away from the unstable site, in such a way that the magnetic energy of the system decreases. This, in turn, can lead to the formation of new unstable crossing angles at neighboring lattice sites, which are then themselves spliced and displaced, and so on in classical avalanching style. The energy collectively liberated by all such unstable nodes is what we associate with flare energy release.

Figure 4.1 illustrates the operation of these rules, here for a very small lattice for graphical clarity. As in so-called "stop-and-go" classical SOC sandpile models, driving is suspended during the course of an avalanche. This is meant to mimic the separation of timescales between photospheric driving (of the order of minutes to hours) and flare onset (seconds).

This novel avalanche model exhibits at least two important characteristics. In terms of the underlying physical basis, all the elements of the cellular automaton can be interpreted without any ambiguity in terms of Parker's picture of stressed coronal magnetic fields. In terms of sandpile-like cellular automata, the whole notion of neighborhood is modified since "nearest-neighbour" here does not necessarily corresponds the neighbouring lattice sites (up/down/top/bottom), but rather the nearest nodes located above and below (open squares on Figure 4.1) along the flux strand forming an angle with another strand at a given lattice site (large solid dot on Figure 4.1). Being thus anisotropic and non-local to some extent our model may belong to a different universality class than the

more conventional isotropic sandpile models developed up to now in the flaring context ([Morales (in preparation)]).

In [Morales & Charbonneau, 2008a] we showed that such a strongly anisotropic model does produce spatially and temporally intermittent, avalanche-like release of magnetic energy, with frequency distributions of avalanche size parameters in the form of power laws with logarithmic slopes comparing well to observationally inferred values. In particular, we showed that the power law exponent for the PDF of total energy release, $\alpha_E = 1.66$, falls within the one-sigma range of the recent observational determination $\alpha_E = 1.52 - 1.77$ of [Aschwanden & Parnell (2002)]. Moreover we also calculated the so-called spreading exponents η and δ and verified that they satisfy the mutual numerical relationship expected from SOC, thus indicating that the cellular automaton does behave as a self-organized critical system ([Morales & Charbonneau, 2008b]).

In [Morales & Charbonneau, 2008b] we also calculated the power-law index of the frequency distribution for flaring areas. We considered two distinct possible definition of flaring area, as exemplified of Figure 4.3, again for a small lattice. The first case is the model's equivalent to a time-integrated flare/avalanche observation, whereby we consider the area A^* defined by the total number of lattice nodes having avalanched at least once during the whole duration of a given avalanche. The second case, loosely akin to very high time cadence observations, consists in defining the area A as the total number of avalanching nodes at the time of peak energy release. Obviously, $A^* > A$, yet we could show that both measures yields frequency distributions of areas having the form of power-laws, with logarithmic slopes comparing much better with observationally inferred values than those produced by isotropic sandpile-like avalanche models.

These encouraging results have motivated us to push further the comparison between our model results and flare observations. In this paper we take advantage of the unambiguous mapping onto loop-like structures that is possible within our model to synthetize artificial images of flaring loops, arbitrarily oriented with respect to the

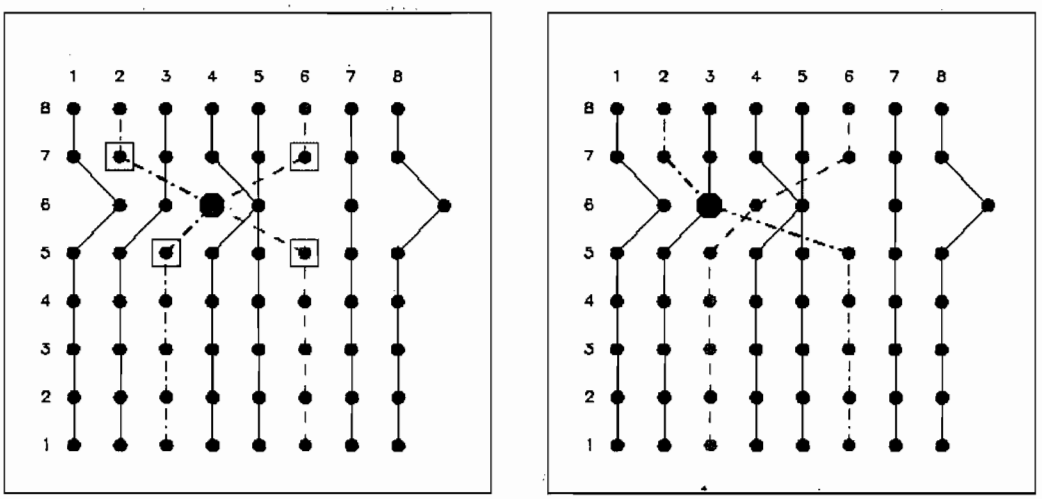

Figure 4.1: Detail of a small lattice showing the basic lattice structure and driving mechanism. The "photosphere" correspond to the top and bottom horizontal rows of nodes. Strands are numbered from left to right and nodes along a given strand, from bottom to top. On the left plot, node $(2, 6)$ of strand 2 has been displaced two units to the right and for strand 6 the node $(6, 6)$ has been displaced two units to the left. Both strands meet at the highlighted node $(4, 6)$ forming an angle $\Theta = 4.1$ rad $> \Theta_c$. The actual first neighbors of node $(4, 6)$ are shown as squares. In the right plot the redistribution rule has been applied and strands 2 and 6 have 'reconnected' and a new unstable angle is formed at node $(3, 6)$. Periodic boundary conditions are enforced in the horizontal direction, so that strands 1 and 8 always experience the same displacement (here one unit to the right).

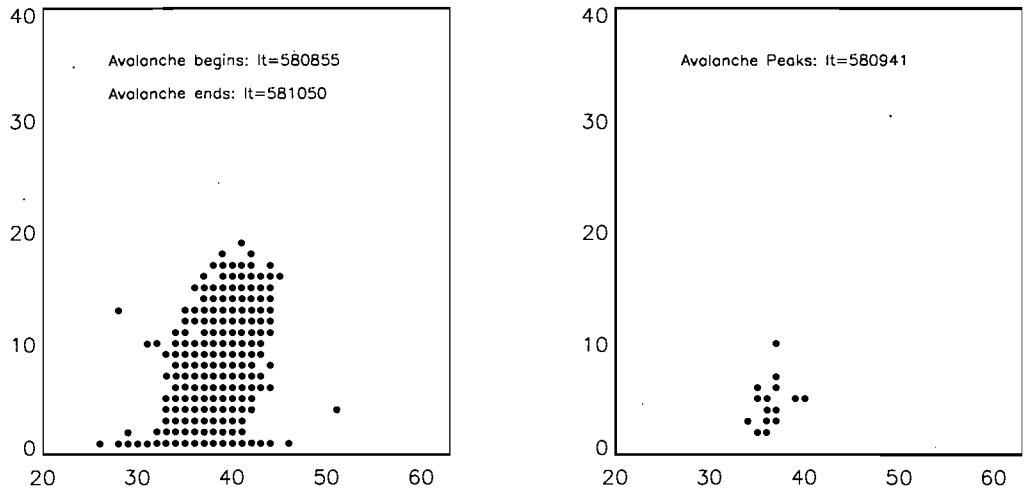

Figure 4.2: The spatial structure of a moderately large avalanche on a 64×64 lattice with $\Theta_c = 2.5$. Each solid dot on the left panel corresponds to a lattice node that has become unstable at least once during the whole avalanche (4535 distinct redistibution events spread over 195 iterations). The right panel shows the 15 nodes that were simultaneously unstable at the time corresponding to the peak of energy release in the course of this avalanche. Note that only part of the lattice is plotted here.

heliocentric radius vector and projected against the plane of the sky. This yields a geometrical setup that is entirely analogous to the way in which spatiotemporally-resolved flare observations are analyzed.

4.4 From a 2D lattice to a synthetic coronal loop

Our simulation is defined over an horizontally periodic 2D cartesian plane representing the outer surface of a "straightened" coronal loop, with the vertical direction parallel to the loop axis. To generate a 3D-synthetic coronal loop with appropriate shape, aspect ratio and orientation, we need to apply a sequence of sequential transformations to our 2D lattice: (1) wrapping into a cylinder; (2) stretching along the cylinder's axis; (3) bending in half into a loop-like structure; (4) rotate in a plane having an arbitrary orientation with respect to the line-of-sight; (5) project into the plane of the sky as a pixel image. We now detail these steps one by one.

We first define a reference right-handed coordinate system where the coordinate z is in the vertical direction and the x, y coordinates define the photospheric plane. Assuming that the 2D lattice is located at the plane $y = 0$, as shown on Figure 4.4A, the nodes (i, j) can be written in terms of the 3D coordinate system as $(0, i, j)$.

The first step is to wrap the 2D lattice around a vertical axis and position the resulting cylinder so that its symmetry axis coincides with the $(x, y) = (0, 0)$ line, as shown on Figure 4.4. Since the length unit on the lattice is by definition the internodal distance, the total width of a $N \times N$ lattice is $N - 1$; assuming that this is the total perimeter of the cylinder, then its radius is simply:

$$r_c = \frac{N-1}{2\pi} , \tag{4.1}$$

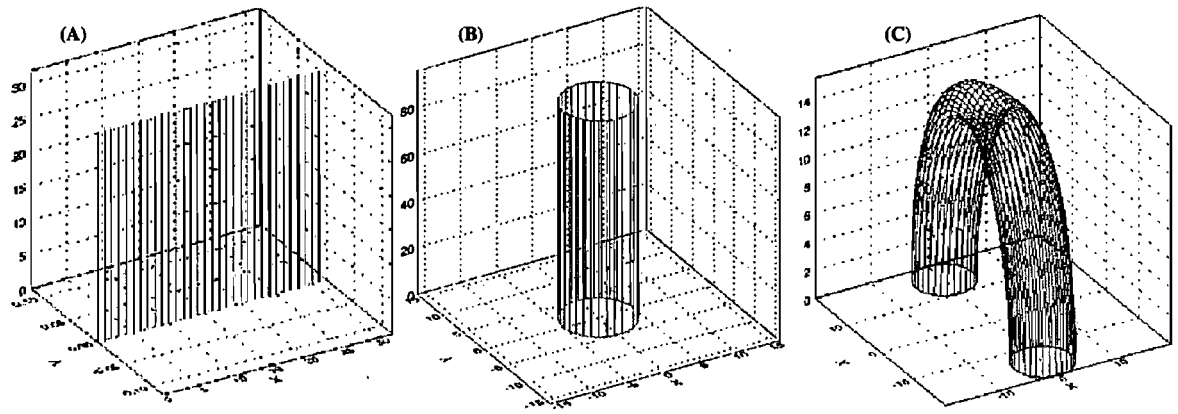

Figure 4.3: Pictorial representation of how a 2D lattice is converted in a cylinder and then bended in a loop. (A) Original 2D lattice of linear size $N = 32$. (B) The formed cylinder that has tripled in length ($\Delta = 3$). (C) A possible view of the synthetic coronal loop, after bending with $R = (N-1)/\pi$.

since the total angle covered by the nodes in the cylinder is 2π we can estimate the angle separation ϕ between node i and the $i = 0$ node as:

$$\beta_i = \frac{2\pi}{N-1} i \ , \qquad i = 1, ..., N-1 \ . \tag{4.2}$$

Thus the new cylindrical coordinates of a node (i, j) will be:

$$x_c(i,j) = r_0 \sin(\beta_i) \ , \tag{4.3}$$

$$y_c(i,j) = r_0 \cos(\beta_i) \ , \tag{4.4}$$

$$z_c(i,j) = j \ . \tag{4.5}$$

In order to bring the model closer to the real aspect ratios characterizing coronal loops we can stretch the cylinder by multiplying the z coordinate by a constant Δ, so that we now have:

$$z_c(i,j) = \Delta j \ , \qquad i = 1, ..., N-1 \ , \qquad j = 1, ..., N \ , \tag{4.6}$$

with $\Delta > 1$ since the length of coronal loops is typically much larger than their cross-section. Figure 4.4B shows the end result of the wrap and stretch steps.

We must now proceed with the (mathematically trickier) bending step. To do this we assume that the total height of the cylinder is the typical radius of the synthetic loop (R_L), so:

$$R_L = \frac{N-1}{\pi} \, . \tag{4.7}$$

The angle formed between each node and the XY plane will be:

$$\phi_i = \frac{\pi}{N-1} i \, . \tag{4.8}$$

Thus, the new coordinates for each node belonging now to the bent cylinder centered and located symmetrically with respect to the vertical axis (z) will be:

$$x_L(i,j) = r_0 \, \sin(\beta_i) \tag{4.9}$$

$$y_L(i,j) = -(R_L + r_0 - y_c(i,j)) \, \cos(\phi_j) \tag{4.10}$$

$$z_L(i,j) = -(R_L + r_0 - y_c(i,j)) \, \sin(\phi_j) \tag{4.11}$$

The result of this bending step is shown on Fig. 4.4C.

To sum up, we can obtain the new coordinates of any node in the synthetic loop by applying to the original 2D lattice nodes a total transformation matrix T that is obtained after multiplying several transformation matrices that wrap, stretch and bend the nodes of the original 2D lattice:

$$\begin{pmatrix} x_L \\ y_L \\ z_L \end{pmatrix} = \begin{pmatrix} R_L\cos(\phi) & R_L\sin(\phi) & 0 \\ -R_L\sin(\phi) & R_L\cos(\phi) & 0 \\ 0 & 0 & 1 \end{pmatrix} \begin{pmatrix} 1 & 0 & 0 \\ 0 & 1 & 0 \\ 0 & 0 & \Delta \end{pmatrix} \begin{pmatrix} r_0\cos(\beta) & r_0\sin(\beta) & 0 \\ -r_0\sin(\beta) & r_0\cos(\beta) & 0 \\ 0 & 0 & 1 \end{pmatrix} \begin{pmatrix} 0 \\ i \\ j \end{pmatrix} \tag{4.12}$$

In a detailed analysis of microflares [Aschwanden et al., 2000] suggested that observations are the projection of the flaring volume of a cylindrical loop onto the plane of the sky. With our model we can project the 3D coordinates of the flaring nodes within the synthetic loop into any chosen plane by simply applying a projection matrix P to the vector (x_L, y_L, z_L). The projection matrix can be easily expressed in terms of the components of the vector $\hat{n} = (a, b, c)$ normal to the projection plane: $aX + bY + cZ = 0$ [1]. For such a plane the corresponding projection matrix is:

$$P = \begin{pmatrix} b^2 + c^2 & -a\,b & -a\,c \\ -b\,a & a^2 + c^2 & -b\,c \\ -c\,a & -c\,b & a^2 + b^2 \end{pmatrix} \tag{4.13}$$

The projected coordinates of any given 3D point belonging to the synthetic loop will be:

$$\begin{pmatrix} x_p \\ y_p \\ z_p \end{pmatrix} = P \begin{pmatrix} x_L \\ y_L \\ z_L \end{pmatrix} \tag{4.14}$$

[1] This is the case for a plane passing through the origin $(0, 0, 0)$ of the cartesian coordinate system. We can work under this assumption without any loss of generality.

By applying equation (4.12) to every node within each avalanche in our simulations we were able to situate those avalanches in our pseudo-3D coronal loop, thus producing the synthetic equivalent of a synthetic flare. We achieve this by covering our projected loop by a 2D cartesian grid of contiguous square pixels, and simply sum the number of avalanching nodes that fall within each individual pixel, which then becomes a proxy for emitted flux. The top panel on The upper part of Figure 4.4 shows an example of a moderately large avalanche on a 32×32 lattice. Each solid dot corresponds to a node having avalanched at least once in the course of this event. The lower part of Figure 4.4(left) shows a 16×16 grid pixellization of the event illustrated above, with the dotted square in showing the area in the plane of the page covered by this pixellization. The gray scale encodes the number of avalanching nodes falling within each pixel. The resulting synthetic image is clearly dependent on the assumed orientation of the loop, as can be seen by comparing the two projections depicted in the lower part of Fig. 4.4. which shows the pixellization corresponding to a different projection of the same avalanche.

Evidently, the synthetic flare image associated with a given avalanche will also depend at least to some degree on the chosen values for the various numerical parameters involved in the wrap/stretch/bend/project/pixellize sequence of steps described above. As an example of the range of possible "flare images" that can be produced from the same avalanche, consider the six synthetic images displayed on Figure 4.5, all produced from the same large avalanche on a lattice of 128×128 in a simulation using a threshold angle $\Theta_c = 2$. This avalanche lasted 1094 iterations, and involved a grand total of 1142 nodal energy release events, with 113 avalanching nodes at the time of peak energy release. The synthetic images displayed in the left column are produced by using the distribution of time-integrated avalanching nodes, which the middle column uses the distribution of avalanching nodes at the time of peak energy release. All images are projection in the plane $X+Y = 0$ and use two different values of the radius of curvature. For the first four panels $R = (N-1)/\pi$ and for the two bottom panels $R = 10(N-1)/\pi$

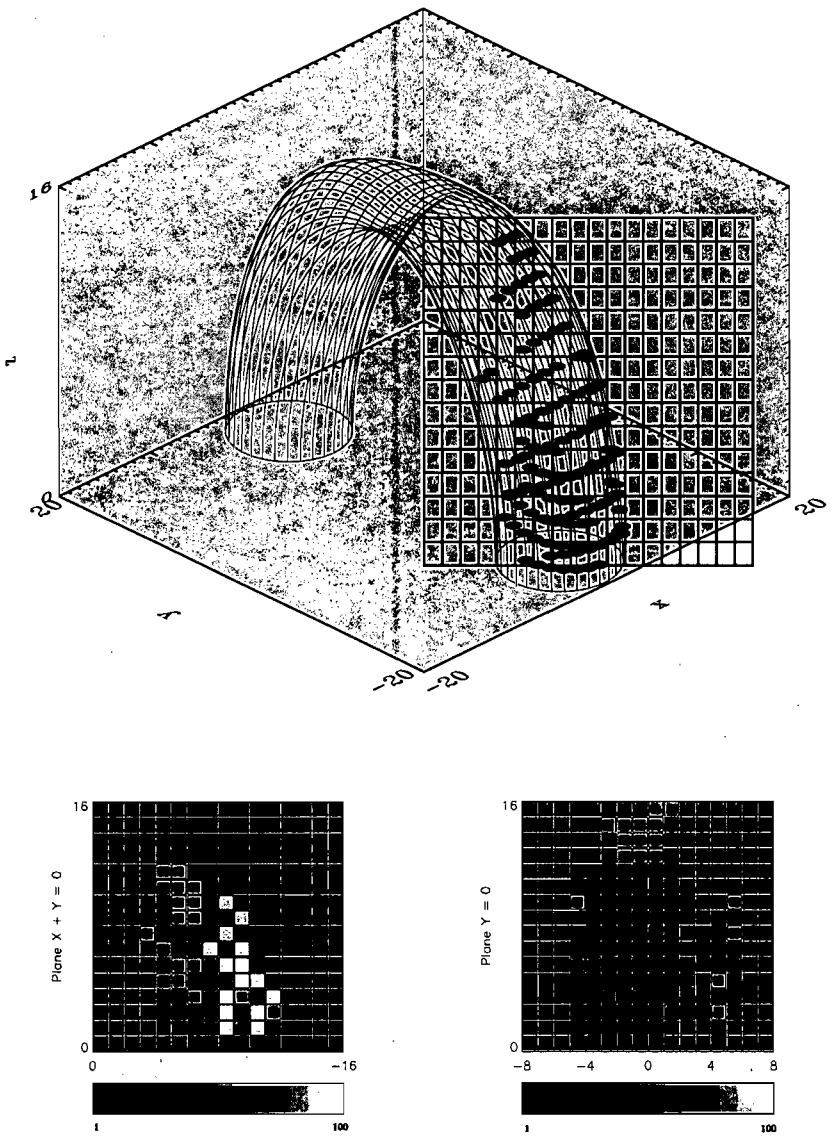

Figure 4.4: The synthetic flare structure for a 32×32 lattice converted in a synthetic coronal-loop (up). In this case $\Delta = 1$ and $R = (N-1)/\pi$. Each dot indicates a lattice node having avalanche once in the course of this avalanche, as on the left panel of Fig. 4.3. The plane of projections $X+Y=0$ is superimposed. The two bottom images show two (coarse) pixellizations of this synthetic flaring loop, for the planes defined by $X+Y=0$ (left) and $Y=0$ (right). The gray scale encodes the number of unstable nodes along the line of sight associated with each individual pixel (see text).

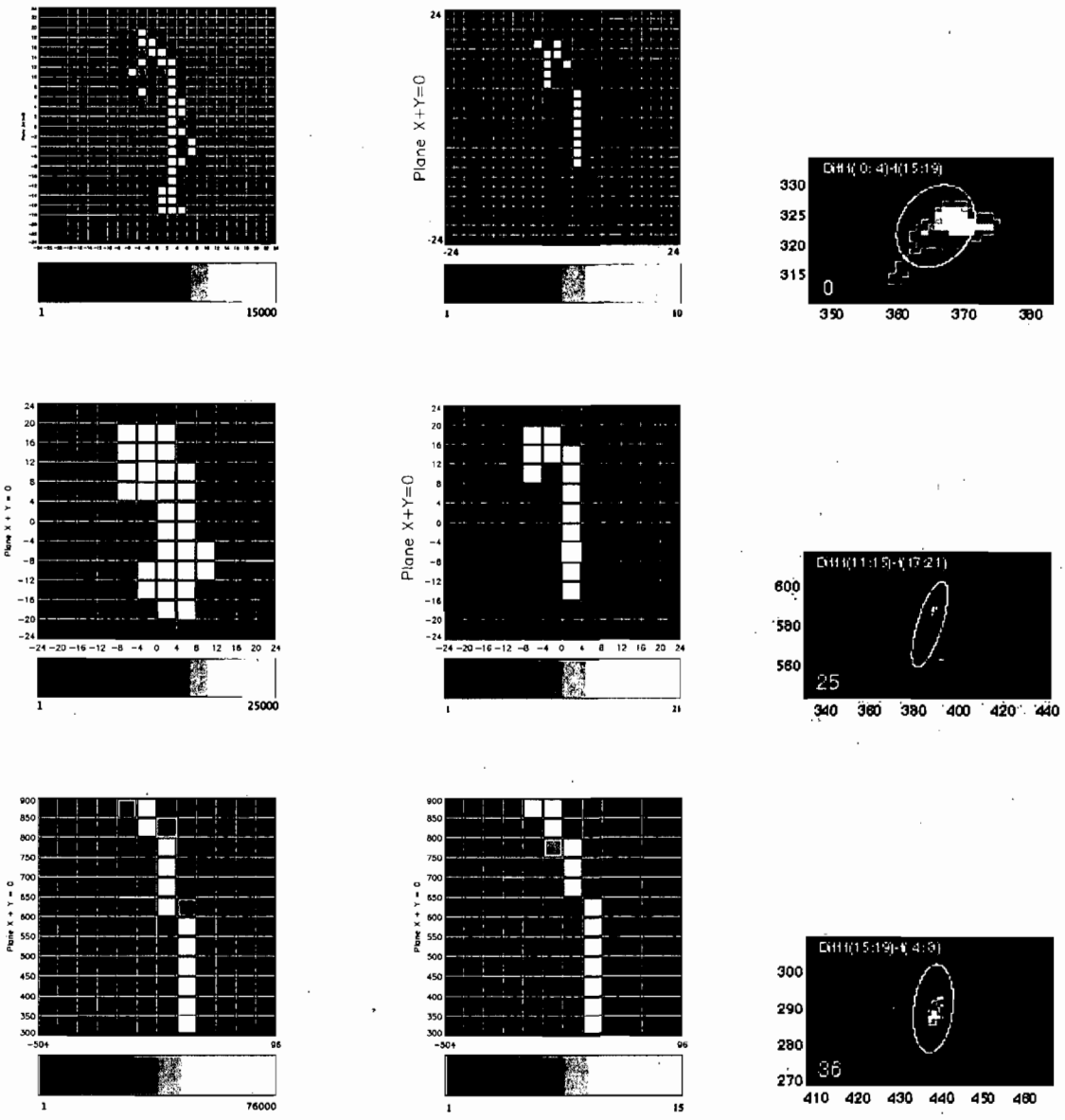

Figure 4.5: "Observational" views of the projections of the time-integrated avalanches (left panels) and at the avalanche peak (central panels) and TRACE observations performed by [Aschwanden et al., 2000] (right panels). The two upper panels show the $X + Y = 0$ projection for a 128×128 lattice and $\Theta_c = 2$ rad. The only difference between the first and second row panels is the pixel size. The third row panel shows the same set of avalanching nodes but for longer loop ($R = 100\,(N-1)/\pi$ and $\Delta = 100$). The pixel size is the same that in row number 2. The three images in the right most column were kindly provided by M. Aschwanden.

the loop length being $N-1$ for the four upper panels and $10(N-1)$ for the remaining panels. The first two rows use a stretching factor of $\Delta = 1$ but two different levels of pixellization (8×8 versus 16×16). The bottom row retains the 16×16 pixellization, but now uses a stretching factor $\Delta = 100$, i.e., 100 times that used to produce the images in the top and middle rows. As a visual comparison point, the three images displayed in the right column are TRACE observations of very small flares, taken from [Aschwanden et al., 2000]. For the the synthetic flare displayed in the bottom row, the combination of high level of stretching ($\Delta = 100$) and coarseness of the pixellization (12×12) washes out all internal structure, leaving only the same projected shape of the bent loop visible on either the time-integrated or peak energy release images. The examples displayed in Figure 4.5 illustrate that our synthetic flare images show a type of general structure that is at least qualitatively similar to observational results. This motivates the more quantitative comparisons to which we now turn.

4.5 Statistical properties of projected avalanches

Isotropic sandpile-like avalanche models of solar flares as well as our strand-based avalanche model both succeed in producing power laws for the probability distribution of avalanche areas. In the classical isotropic models the associated power-law index turned out much smaller than observationally-inferred values (see, e.g., [McIntosh et al. (2002)]) while our recent SOC model yields numerical values in better agreement with observational inferences. However, this better agreement may be fortuitous to some extent, since the flaring areas were calculated directly in the 2D cartesian lattice, which is not a one-to-one representation of the observational plane. Following the sequence of steps described in the preceding section we are in a position to synthetize observations in a plane equivalent to the plane of the sky, and revisit this question in a more meaningful manner.

Starting from long simulation runs on lattices of various sizes, we calculate the avalanche areas (time-integrated and peak time), for projections on the four planes defined by the equations: $X+Y+Z=0$, $X-Y=0$, $X+Y=0$ and $X-Z=0$. Not surprisingly, the frequency distributions of projected avalanche areas are found to take the form of well-defined power-laws, spanning over two orders of magnitude in area. A representative example is presented on Figure 4.6 for the case of a 128×128 lattice with $\Theta_c = 2.25$. Distributions are calculated for both time-integrated area and area at time of peak energy release (cf. Fig. 4.6). The top three lines of Table 1 compile the corresponding power-law indices for time-integrated areas (α_A^*) and peak area (α_A), for three different lattice sizes. The error values are the maximum of the standard deviation of the line's slope obtained by using a linear fittingst squares routine. Having established previously that the statistical properties of avalanches do not depend on the threshold angle (Θ_c) in the range considered here (see [Morales & Charbonneau, 2008a] and [Morales & Charbonneau, 2008b]), all results presented in Table 1 used as threshold angle $\Theta_c = 2$ rad. Whether working with time-integrated avalanches or peak snapshots, within error bars the inferred power-law indices are independent of lattice size, as one would expect from a SOC system.

The three lines of Table 1 identified as LH-2D and LH-3D list the corresponding power-law indices for a selection of 2D and 3D simulations using the Lu & Hamilton isotropic sandpile model, as taken from [McIntosh et al. (2002)]. In the 3D case the areas correspond to projections on the three cartesian planes of the lattice cube, while for the 2D simulations is just the area of the avalanching region (as on Fig. 4.5 herein). In the last four lines of Table 1 we reproduce the results presented in Table 3 of [Aschwanden & Parnell (2002)]. In that table they used TRACE data obtained in two wavelengths (195$\mathring{A}$ and 171$\mathring{A}$) on two dates. The campaign A took place on February 24th of 2000, produced a database of 816 flare events (436 observed at 171$\mathring{A}$ and 380 observed at 195$\mathring{A}$) with flare energies going from microflares all the way to nanoflares as shown in figure 10 in [Aschwanden & Parnell (2002)]. Campaign B, on the other hand,

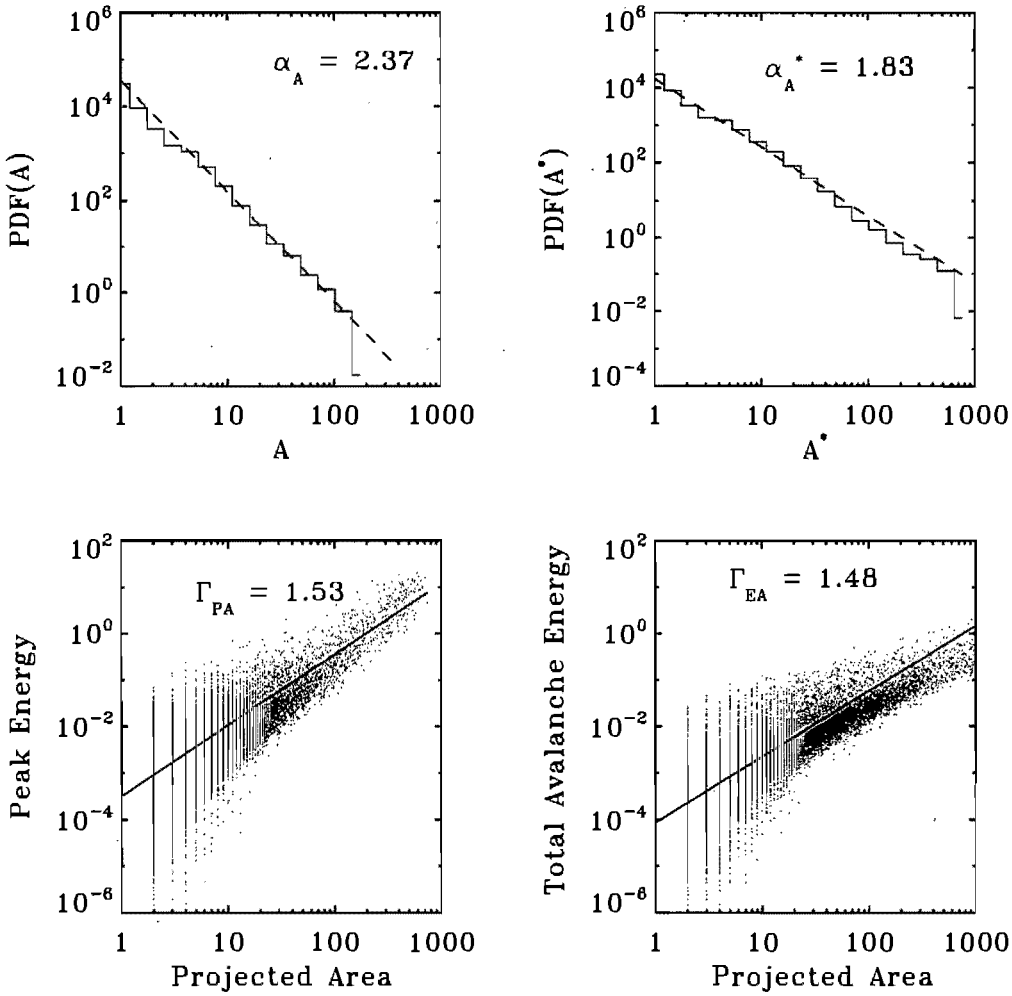

Figure 4.6: An illustrative case of the frequency distribution obtained for the projected area both for the time-integrated avalanches (top-right) and for the avalanche peak (top-left). In this case we worked with a 128×128 lattice a threshold angle $\Theta_c = 2.25$ rad and $\Delta = 1$. These correlation plots are constructed from $\sim 2.2\,10^4$ distinct avalanches. The two lower plots show the correlation between avalanches area and total released energy. The plot on the left shows the correlation between energy release and area at the time of peak energy release, while the plot on the right shows a similar plot for the time-integrated area and energy release over the duration of each avalanche.

Table 4.1: Power-law indices for correlation plots for series of lattice simulations for different lattice sizes and compilation of previous results

N	α_A	α_A^*	Γ_{EA}	Γ_{PA}
32	2.31 ± 0.09	1.73 ± 0.08	1.57 ± 0.15	1.37 ± 0.15
64	2.32 ± 0.09	1.73 ± 0.08	1.65 ± 0.10	1.56 ± 0.1
128	2.37 ± 0.09	1.83 ± 0.08	1.48 ± 0.10	1.53 ± 0.08
LH-2D (64)	1.05 ± 0.07	0.52 ± 0.03	1.07 ± 0.05	1.04 ± 0.04
LH-2D (128)	1.02 ± 0.06	0.55 ± 0.02	1.06 ± 0.04	1.04 ± 0.04
LH-3D (64)	1.12 ± 0.05	0.63 ± 0.03	1.59 ± 0.04	1.07 ± 0.03
TRACE 195(A)	2.16 ± 0.18			
TRACE 195(B)	2.25 ± 0.04			
TRACE 171(A)	2.45 ± 0.09			
TRACE 171(B)	2.34 ± 0.09			

took place on February 17th of 1999. In this case they registered 281 flare events with energies spanning from 10^{24} erg to 10^{32} erg (see [Aschwanden & Aschwanden (2008a)]) and measured the equivalent of the flare peak avalanching areas.

We also studied the correlation between the projected areas and the energy liberated by each avalanche. We found tight power laws extending over at least three to four orders of magnitude as illustrated in Figure 4.6. [Aschwanden & Aschwanden (2008a)] calculated the correlations measures between area and total emission measure and between area and thermal energy (figure 7). They obtain correlation exponents of 1.539 and 1.634 respectively. This values are in agreement with the ones presented in the fourth column of Table 2.

Having obtain a first evidence of the utility of the synthetic avalanching loop as a tool to model solar flares we turn now to a pure geometrical property of avalanches: the fractal dimension.

4.6 Fractal dimension of projected avalanches

Solar flares have fractal and filamentary structure. Thermal energy or electron density can be determined more accurately if the fractal dimension of the filling factor is known [Aschwanden & Aschwanden (2008a)]. In the last twenty years several observational determinations of the flaring area's fractal dimension D have been carried out using different kind of data such as photospheric magnetograms, EUV and soft X-ray images of nanoflares, and EUV images of the quiet Sun. The inferred values of D cover an extremely broad range, down from 1, corresponding to linear objects, to 1.93, i.e., almost a pure 2D object (see Table 1 in [Aschwanden & Aschwanden (2008a)] and references therein). Essentially all of these determinations use one of two approaches: calculating the area/volume or radius/area relationship, or the box-counting method.

For numerical avalanche models of flares, on the other hand, there exist comparatively few determinations of the fractal dimension. Only [McIntosh et al. (2001)] and [McIntosh et al. (2002)] have performed estimations of the fractal dimension using the ratio of area to linear dimensions, the latter estimated via the radius of gyration, for avalanching areas taken from for 2D simulations and cartesian plane projections of 3D simulations. They obtained fractal index values in the range $1.55 \leq D \leq 1.79$ for peak area, and $D \simeq 2$ in the case of time-integrated avalanche areas.

Calculating the fractal dimension of structures is analogous to measuring the length of a curve, the area of a surface, or the volume of a 3D-object. To do this one calculates the number of segments, or squares or cubes (depending on the structure's euclidean dimension) of size δ needed to cover the whole structure. For the case of a segment of length L:

$$L = N(\delta)\delta \ , \tag{4.15}$$

where $N(\delta)$ is the number of segments needed to cover the line of length L. If $L = 1$ it can be easily calculated that $N(\delta) = 1/\delta$. In the same way for a unit square $N(\delta) = 1/\delta^2$ and for a unit cube $N(\delta) = 1/\delta^3$.

In more complicated cases one can find very twisted curves that have infinite length. The Hausdorff-Besicovitch fractal dimension gives a better way of characterizing such complex objects. For a general introduction on the subject see: [Mandelbrot, 1977], [Feder, 1988] and [Schuster, 1989]. In a general case one may try to measure the size of a set of points, S, in the space by using á test function:

$$h(\delta) = \gamma(d)\delta^d \,, \tag{4.16}$$

where γ is a geometrical factor. One may then use this function to cover the fractal object of interest so that its measure M_d is:

$$M_d = \sum_{N(\delta)} \gamma(d)\delta^d \,. \tag{4.17}$$

When $\delta \to 0$ this measure will be:

$$\lim_{\delta\to 0} M_d = \lim_{\delta\to 0} \sum_{N(\delta)} \gamma(d)\delta^D = \lim_{\delta\to 0} \gamma(d)N(\delta)\delta^D \to \begin{cases} 0, & d > D \\ \infty, & d < D \end{cases} \tag{4.18}$$

The Hausdorff-Besicovitch dimension D of a structure S is the critical dimension for which M_d changes from 0 to infinity. The quantity D is a local property, in the sense that it measures properties of sets of points in the limit of a vanishing diameter or size δ of the test function used to cover the set S.

The result of equation (4.18) can be used to calculate the fractal dimension of a given surface. Assuming that the frame containing the surface of interest is of unit size it is possible to cover this surface by evenly spaced squared grid of side δ so that:

$$1 \propto \sum_{N(\delta)} \delta^D \propto N(\delta)\delta^D \ , \tag{4.19}$$

from which:

$$D \propto \frac{\log(N(\delta))}{\log(1/\delta)} \ . \tag{4.20}$$

Equation (4.20) now gives the Hausdorff-Besicovitch dimension in terms of a countable amount of squares, rather than a limit measure, as in eq. (4.18), which is more convenient computationally.

In order to estimate the value of D for the avalanches produced by our simulations we applied the following procedure: we start with a bitmap of the pixellized images associated with some chosen projection plane, as produced following the procedure described previously in §3. Two representative examples are shown in the leftmost column of Figure 4.7, for a reference pixel size $\delta = 1$. White (black) pixels are those in which no (at least one) active lattice node is mapped for the chosen mapping and projection parameters. The middle and rightmost column show the result of the same procedure applied with pixels of successively doubled size ($\delta = 2$ and $\delta = 4$). It is then just a matter of counting the number $N(\delta)$ of black pixels associated with each pixellization, and using equation (4.20) to compute D. One should rightfully expect that the computed values of D will depend on choices made for the numerical parameters used in converting our 2D cartesian lattice to a bent loop-like structure, and in particular on the stretching factor Δ. Table 2 lists the computed values of D for sets of simulations carried out on three different lattice sizes, for values of Δ varying from unity (thick short loop) to 100 (thin long loop) that corresponds to radius varying between ~ 40 and 4000. For a given lattice size, the "database" of avalanches is always

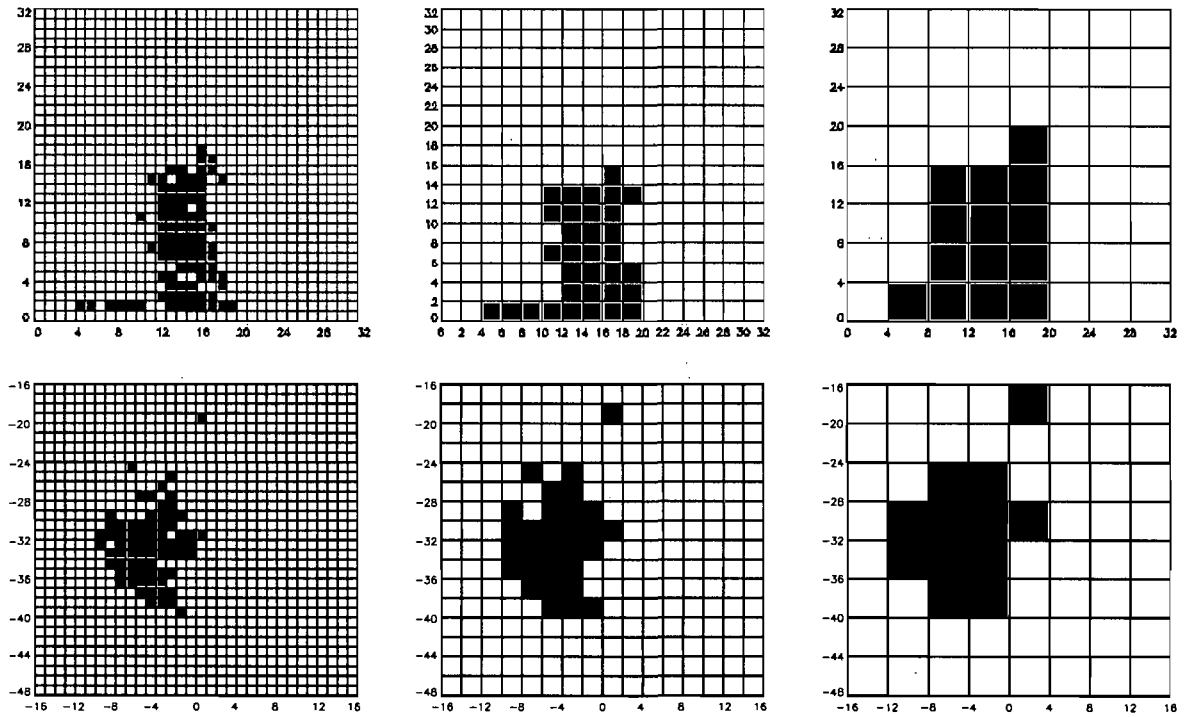

Figure 4.7: Box counting method displayed for two different lattices. In the upper figure we present the XZ-projection of an avalanche produced in a 32×32 lattice. The avalanche involves 771 nodes and lasted 217 iterations. The lower figure presents the XY-projection of an avalanche produced in a 64×64 lattice. The avalanche involves 2541 nodes and lasted 190 iterations.

the same, and so are the projection planes used to construct the synthetic flare images. The error represents the maximum standard deviation from the average value.

Table 4.2: Area fractal dimension D for different lattice sizes and stretching factors

N	D	Δ
32	1.28 ± 0.05	1
64	1.24 ± 0.06	1
128	1.34 ± 0.06	1
32	1.20 ± 0.05	10
64	1.19 ± 0.04	10
128	1.17 ± 0.05	10
32	1.12 ± 0.04	30
64	1.11 ± 0.04	30
128	1.12 ± 0.05	30
32	1.03 ± 0.04	100
64	1.06 ± 0.04	100
128	1.08 ± 0.05	100
LH-2D(64)	2.02 ± 0.05	$\equiv 1$
LH-2D(128)	2.01 ± 0.06	$\equiv 1$
EIT/SOHO ([Uritsky et al., 2001])	1.5 ± 0.1	$\equiv 1$
EUV 171 $\AA$ ([Aschwanden & Aschwanden (2008a)])	1.34 ± 0.24	$\equiv 1$

For a given value of Δ, the calculated fractal dimension is independent of lattice size within error bars, as expected from the self-similarity characterizing avalanching dynamics in the model. Even at $\Delta = 1$ the inferred fractal dimension D is far from the Euclidean limit $D = 2$; this is not surprising since a large fraction of the simulated avalanches tend to exhibit an elongated structure, a direct consequence of the strongly anisotropic nodal connectivity on the lattice. This leads to fractal dimension that look

more like nearly unidimensional structures, such as the Koch's curve: $D = 1.2618$ (see, e.g., Fig. 2.8 in [Feder, 1988]).

In Figure 4.8 we plot the fractal dimension (D) versus loop stretching Δ, for various lattice size, as coded by the various symbols. All these data can be well fit by a power-law relationship of the form:

$$D \propto \Delta^{-\epsilon} , \tag{4.21}$$

with a least-squares fit yielding a power-law slope $\epsilon = -0.043 \pm 0.007$. The proportionality constant in this case, D_0 is the value of the fractal index when the synthetic loop experiences no stretching ($\Delta = 1$). That the fractal dimension should then towards unity as the loop is stretched to very large aspect ratio is of course not surprising. What is noteworthy is that even for rather large stretching factors (many tens), the flaring area retain a markedly non-linear fractal dimension ($D \simeq 1.2$ at $\Delta = 10$).

Recent high time cadence observations presented by [Aschwanden & Aschwanden (2008a)] showed that the fractal dimension of flaring areas evolves with time with values ranging between $[1, 1.64]$ for the initial fractal dimension, up to $[1.78, 1.97]$ for the fractal dimension corresponding to the moment of maximum area. Since our model does not simulate the thermalization phase occuring in flares and we can only reproduce the initial energy release at flaring onset event we believe that our results should be compared to the fractal dimension values obtained at the onset of the flare. Inspection of Table 2 of [Aschwanden & Aschwanden (2008a)] show that $1 \leq D \leq 1.31$ for 6 out of 10 of the initial fractal dimension values for the M-Class flares (see also their Figure 10), with the mean value of the whole data set: $< D >= 1.34 \pm 0.24$. This would suggest that our shorter loops model more properly the observed flares.

In Table 2 we also presented the results obtained by [Uritsky et al. (2007)]. In this case they calculated the fractal dimension for an EUV-brigh region at the peak of a brightening event. They identify an avalanching region as the region where EUV flux

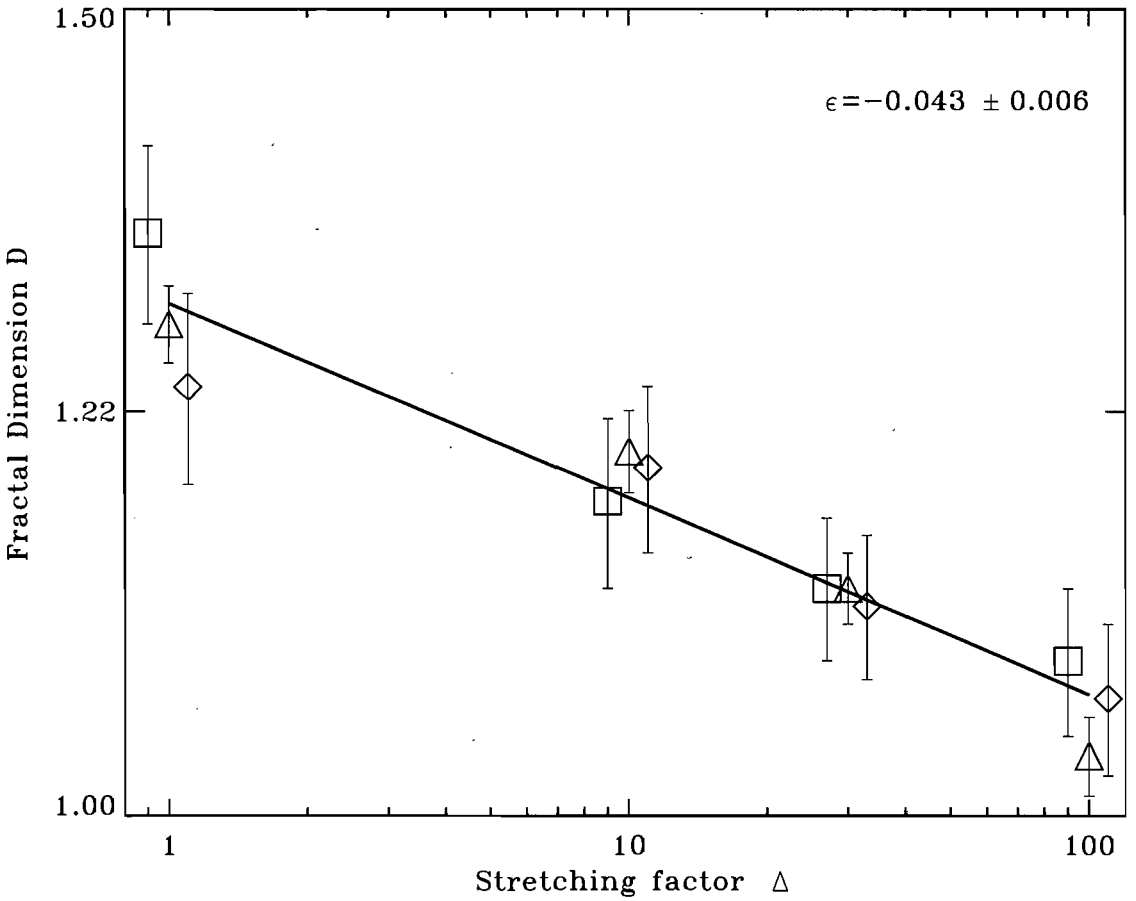

Figure 4.8: Best fit to eq. (4.21) obtained by performing linear regression analysis on the three differents set of simulation results compiled in Table 2: triangles for a 32×32 lattice, diamonds for 64×64 and squares for the 128×128.

exceeded a certain threshold. For more than 7000 EIT images collected by SOHO in the 195$\AA$ wavelength, they obtain $D = 1.5 \pm 0.1$ for both solar maximum and minimum. This value is closer to that inferred by [Aschwanden & Aschwanden (2008a)] for the epoch of peak energy release than for the epoch of flare onset which, we believe, is more appropriate for comparison with our synthetic images.

4.7 Summary and discussion

In this paper we have generated synthetic flare-like spatiotemporal energy release events using the novel self-organized critical avalanche model described in Morales & Charbonneau (2008a). This model is based on a two-dimensional isotropic cellular automaton designed to offer an idealized representation of a coronal loop, geometrically and operationally, and is very much along the line of the physical picture of nanoflares proposed by Parker (1983, 1988). By virtue of its design, this avalanche model can be mapped onto a geometrically realistic coronal loop without ambiguity with regards to the physical correspondence of model elements. A sequence of straightforward transformations can then turn an avalanche taking place on the 2D lattice into an avalanche occurring within a 3D curved loop-like structure with realistic aspect ratio. This can then be projected at arbitrary angles onto the plane of the sky and turned into a two-dimensional pixel intensity image akin to those produced by high resolution EUV and X-Ray imaging instruments.

We have focused here primarily on the geometrical properties of synthetic flares images produced by our SOC model. In particular, we have computed the frequency distribution of flaring areas, which was found to take the form of a well-defined power-law with a logarithmic slope $\alpha_A = 2.35$ comparing very well to the observationally-inferred value ($1.86 \leq \alpha_A \leq 2.45$, see, e.g., Aschwanden & Parnell 2002), unlike earlier SOC models of flares based on conventional, isotropic sandpile-like cellular automata.

This is a robust result that was found to depend very little on the adopted lattice size and other model parameters, or on the assumed aspect ratio for the loops. As shown in Morales & Charbonneau (2008a), this model also yields frequency distribution of flaring energy, peak flux and duration that also compare favorably to observations.

We also studied the fractal dimension of our synthetic flares images. We first established that these images do obey the self-similar scaling expected of fractal structures, and then obtained a fractal dimension (D) in the narrow range $1.1 \leq D \leq 1.34$, with the lower bound corresponding to "long thin loops" with length-to-diameter aspect rations of up to 100:1, and the upper bound to "short fat loops" with aspect ratio of order unity. This range compares quite well to the mean fractal dimension $D = 1.34$ inferred observationally using data from [Aschwanden & Aschwanden (2008a)] for M-Class flares.

The good agreement between the observed geometrical properties of real solar flares and their synthetic counterpart produced by our model suggests that the latter, despite its (relative) simplicity, could serve as a bridge between spatiotemporally resolved observations of flare energy release and the microscale physical processes underlying the flaring phenomenon, most notably magnetic reconnection, that are below the resolution limit of current and forthcoming instruments. In our model, the unfolding of an avalanche is intimately tied to the discrete rules introduced to mimick magnetic reconnection and destabilization of neighbouring nodes. In principle, different reconnection scenarios could translate into different choices for these discrete rules, and therefore into distinct avalanching dynamics. Observational constraints on the latter then become constraints on the small-scale microphysics underlying the discrete rules. Conversely, the synthetic flares produced by our model could be used to test and validate algorithms for the automatic detection and tracking of flare energy release, and/or reconstruction of coronal loop geometrical parameters from observed EUV or soft X-Ray emission.

The fact remains that cellular-automaton models such as the one used here remain far removed from the plasma and magnetohydrodynamical processes collectively producing what we call flares. Yet, these models evidently catch some essential aspect of the process. Self-similarity in energy release statistics and a non-integer, fractal dimension for the flaring volumes all hint that solar flares represent yet another instances of physical phenomena increasingly becoming known under the name of *natural complexity*. The hallmark of such systems is a global dynamical behavior governed by local threshold-interactions between a large number of degrees of freedom. Without denying the fact that the physical heart of the flaring process, magnetic reconnection, would be better described by magnetohydrodynamics rather than largely ad hoc discrete interaction rules, natural complexity offers a higher level framework unifying processes taking place in very different physical systems ([Uritsky & Klimas, 2004]). As a case in point, it should be noted that energy release in the earth's magnetotail is increasingly being viewed as yet another instance of natural complexity (see for example [Uritsky et al., 2001] and [Uritsky & Klimas, 2004]), and modelling frameworks similar to that used here are gaining more and more recognition as viable descriptors of magnetospheric substorms (see for example [Chang (1992)], [Liu et al. (2006)]; and references therein).

Many developments of our model are still possible, notably the generalization to a truly 3D cylindrical lattice, which would allow the introduction of driving rules that would incoporate a prefered direction of twist. At a more theoretical level, it would be interesting to investigate whether our line-based, anisotropic cellular automaton belongs to a universality class distinct from the curvature-triggered isotropic sandpile models that have dominated the modelling of flares as avalanches of elementary reconnection events. Improved synthesis of pseudo-flare statistics could also make use of some of the loop parameter scalings established observationally (see, e.g., [Aschwanden et al., 2000]).

Another important possible step towards physical realism would be to use the localized nodal energy release produce by our model as input to 1D thermalization models of coronal loop ([Klimchuk (2008)]), in order to synthetize actual EUV emission measures that would be comparable in detail to spatiotemporally resolved flare observations.

This research is supported in part by the Natural Sciences and Engineering Research Council (Canada) and by the Fond Québécois pour la Recherche sur la Nature et les Technologies (Québec).

Bibliography

[Aschwanden & Aschwanden (2008a)] Aschwanden, M. J. & Aschwanden, P. 2008, ApJ, 674, 530

[Aschwanden & Aschwanden (2008b)] Aschwanden, M. J. & Aschwanden, P. 2008, ApJ, 674, 544

[Aschwanden et al. (2000)] Aschwanden, M. J., Tarbell, T. D., Nightingale, R. W., Schrijver, C. J., Title, A., Kankelborg, C. C., Martens, P., & Warren, H. P. 2000, ApJ, 535, 1047

[Aschwanden & Parnell (2002)] Aschwanden, M. J & Parnell, C. E. 2002, ApJ, 572, 1048

[Bak et al. (1987)] Bak, P., Tang, C., & Wiesenfeld, K. 1987, Phys. Rev. Lett, 59, 381

[Chang (1992)] Chang, T. 1992, EEE Transactions on Plasma Science, 20 (6), 691

[Charbonneau et al. (2001)] Charbonneau, P., McIntosh, S. W., Liu, H.-L., & Bogdan, T. J. 2001, Sol. Phys, 203, 321

[Dahlburg et al. (2005)] Dahlburg, R. B., Klimchuk, J. A., & Antiochos, S. K. 2005, ApJ, 622, 1191

[Dennis (1985)] Dennis, B. R. 1985, Sol. Phys., 100, 465

[Feder (1988)] Feder, J. 1988, Fractals (Plenum press: New York)

[Georgoulis & Vlahos (1996)] Georgoulis, M. K. & Vlahos, L. 1996, ApJ, 469, L135

[Georgoulis & Vlahos (1998)] Georgoulis, M. K., & Vlahos, L. 1998, A&A, 336, 721

[Klimchuk (2008)] Klimchuk, J. A., Patsourakos, S., Cargill, P. J. 2007, ApJ, 682 (2), 1351

[Liu et al. (2002)] Liu, H.-L., Charbonneau, P., Pouquet, A., Bogdan, T. J., & McIntosh, S. W. 2002, Phys. Rev. E, 66, 056111

[Liu et al. (2006)] Liu, W. W., Charbonneau, P., Thibault, K., Morales, L. F. 2006 Geophys. Res. Lett., 33, L19106

[Longcope & Noonan (2000)] Longcope, D. W. & Noonan, E. J. 2000, ApJ, 542, 1088

[Lu (1995)] Lu, E. T. 1995, Phys. Rev. Lett., 74, 2511

[Lu & Hamilton (1991)] Lu, E. T., & Hamilton, R. J. (1991), ApJ, 380, 89

[Lu et al. (1993)] Lu, E. T., Hamilton, R. J., McTiernan, J. M., & Bromund, K. R. 1993, ApJ, 412, 841

[Mandelbrot (1977] Mandelbrot, B. B. 1977 The fractal geometry of nature. W. H. Freeman and Company, New York

[McIntosh et al. (2001)] McIntosh, S. W & Charbonneau, P. 2001, ApJL, 563, 165-168

[McIntosh et al. (2002)] McIntosh, S. W, Charbonneau, P., Bogdan, T. J, Liu, H.-L., & Norman, J. P. 2002, Phys. Rev. E, 65, 46125.

[Morales & Charbonneau (2008a)] Morales, L. F. & Charbonneau, P. 2008, ApJ, 682 (1), 654.

[Morales & Charbonneau (2008b)] Morales, L. F. & Charbonneau, P. 2008, Geophys. Res. Lett., 35, L04108

[Morales (in preparation)] Morales, L. F. (in preparation)

[Parker (1983)] Parker, E. N. 1983, ApJ, 264,635

[Parker (1988)] Parker, E. N. 1988, ApJ, 330, 474

[Schuster (1989)] Schuster, H. G. 1989 Deterministic Chaos: An introduction. Wiley-VCH, Weinhein

[Uritsky et al. (2007)] Uritsky, V. M., Paczuski, M., Davila, J. M. & Jones, S. I. 2007, PRL, 99(2), 25001

[Uritsky et al. (2001)] Uritsky, V. M., Klimas, A. J. & Vassiliadis, D. 2001, Geophys. Res. Lett., 28, 3809

[Uritsky & Klimas (2004)] Uritsky, V., M. & Klimas, A. J. 2004, Substorms-7, Proceedings of the 7th International Conference on Substorms, 51-54

Chapter 5

Conclusions

Self-organized criticality has been a successful paradigm used to produce models that simulate the main statistical properties of solar flares. From the first models developed by Lu and Hamilton ([Lu & Hamilton, 1991], [Lu et al., 1993]), many variations have been constructed, making use of a variety of stability criteria, redistribution rules, driving mechanisms and lattice structures. Nevertheless, as has been pointed out by Charbonneau and collaborators ([Charbonneau et al., 2001]), in many of the classical SOC models it is hard to clarify the underlying physical basis of the principal constitutive elements, and even harder to interpret them in terms of magnetic reconnection in coronal structures ([Parker, 1983] and [Parker, 1988]).

In this thesis our main goal was to develop a new self-organized model for solar flares which could address many of the difficulties presented by classical SOC models. With this model we are getting closer to the theoretical model proposed by Parker ([Parker, 1983], [Parker, 1988]).

In chapter 2 we introduced the new avalanche model of magnetic energy release by solar flares. The model is based on an idealized representation of a coronal loop, in the form of 2D anisotropic cellular automaton whose fundamental element is a magnetic

flux strand. These strands of magnetic flux collectively make up the coronal loop. The driving is produced by stretching of randomly chosen line subsections representing the effect of the photospheric footpoint motions. Stability is defined in terms of the angle subtended by two (or more) strands at lattice sites where they cross [Parker, 1988], [Dahlburg et al., 2005]. The redistribution rule applied to recover stability is enforced by a cut-splice-move sequences that mimics magnetic reconnection. This "synthetic reconnection" is designed to decrease lattice energy and alter topological linkage between strands that form the loop.

We showed that this driven dissipative cellular automaton evolves to a SOC state where energy is released intermittently (both spatially and temporally) by avalanches of reconnection events collectively spanning a wide range of sizes, from a single site to a large fraction of the whole lattice. The probability distribution functions for avalanche size measures (total energy released, peak luminosity and avalanche duration) take the form of power-laws. The typical values obtained are in accordance with observationally-inferred values. In particular, our power law exponent for the probability distribution function of total energy release is $\alpha_E = 1.66$, which falls within the one-sigma range of the recent observational determination $\alpha_E = 1.52 - 1.77$ of Aschwanden & Parnell (see [Aschwanden & Parnell, 2002]). Power-law indices were calculated for different lattice sizes and threshold angles and shown to remain constant (within the error bars). This is a clear indication that the system behaves in a self-organized critical way, without need of tuning any parameter. The other avalanche size measures also correlate with each other and here again our model compares favorably with observations, significantly better, in fact, than other SOC avalanche models of solar flares relying on "classical" sandpile-like isotropic lattices.

We carried on this power-law analysis by calculating, in our second paper ([Morales & Charbonneau, 2008b]), some geometrical properties of avalanches. Specifically, we examined the avalanches surface at their peak and as time-integrated objects and calculated the power-law indices (α_A and α_A^*) associated to their frequency

distribution function. Both quantities had already been calculated for classical SOC models, and they remained far from the observationally estimated values: $\alpha_A = 2.45$ and $\alpha_A^* = 1.86$ [Aschwanden & Parnell (2002)]. The avalanches produced by our simulations yield α_A between 2.2 and 2.53 and α_A^* between 1.77 to 1.93. Indeed, the [Morales & Charbonneau, 2008a] model succeeds in correcting what, up to now, had remained arguably the most serious discrepancy between flare observations and prediction from isotropic sandpile-like avalanche models. The fact that the quantities (E, P, T, ΔT and areas) all exhibit well-defined power laws spanning many orders of magnitude is strongly suggestive of a self-organized critical state, and we have rigorously proven this by a formal scaling analysis in chapter 3 ([Morales & Charbonneau, 2008b]). In particular, we have demonstrated that the growth of avalanches in the new SOC model presented in this thesis exhibits the dynamical scaling relations characteristic of critical behavior. We achieved this demonstration by calculating the so-called spreading exponents η, δ, κ and β and verified that they satisfy the mutual numerical relationship expected from SOC systems.

The aforementioned results suggested that the numerical model should be ideally suited to push further the detailed comparison with high-cadence, high-resolution flare observations obtained by space-borne instruments such as TRACE. Solar flares observations actually consist in measuring the flux of short wavelenght radiation coming from a flaring loop as seen projected on the plane of the sky.

The one-to-one geometric correspondence between our anisotropic lattice and an actual coronal loop, and the periodic boundary condition imposed by design allowed us to transform the 2D cartesian lattice into a synthetic coronal loop and project this result onto any pre-selected plane. This transformation was performed in the work presented in chapter 4 ([Morales & Charbonneau, 2008c]) by applying a series of matrices transformations to the original nodes that formed the lattice. After this procedure we obtained avalanches regions that visually resemble the flaring regions observed by SOHO and TRACE. We calculated the fractal dimension of the flaring-like avalanche

structures by using a box counting method. The results obtained compare well with observational values documented in the bibliography [Aschwanden & Aschwanden, 2008].

At the level of physical interpretation in the solar flare context, the model introduced herein offers a number of attractive features. First, the flux conservation constraint $\nabla \cdot \mathbf{B} = 0$ is satisfied by design; second an unstable node can be thought as a place where a current sheet is forming and, moreover, reconnection occurs as a consequence of this instability; third, during driving, the length of flux strands increases, reproducing the growth of magnetic energy; fourth, the periodic boundary conditions allow us to restore the cylindrical loop structure to 2D lattice. Once the avalanching process has started, the system releases a significant fraction of the magnetic energy stored in the lattice; for reasonable values of coronal loop parameters, the energy released by avalanches in the model spans the range from nanoflares $\sim 10^{23}$ erg to much larger flares $\sim 10^{29}$ erg. Finally, when mapped back onto a typical coronal loop dimensions, the threshold angle above which reconnection occurs is of the same order of magnitude as the theoretical estimates of Parker (1988) and numerical simulations of [Dahlburg et al., 2005].

The logarithmic slope α_E of the probability distribution function of energy release characterizing our simulations results is too low for nanoflares to dominate the energy release budget, which would require $\alpha_E > 2$. So, even if the present model is a viable way of modeling the statistical properties of flares, it is not, in its current form, a viable statistical model for coronal heating by nanoflares.

In summary, the new cellular automaton introduced and fully analyzed in this thesis, represents a major breakthrough in the field of self-organized critical models for solar flares since:

- Every element in the model can be directly mapped to Parker's model for solar flares, thus solving the major problems of interpretation posed by classical SOC models.

- For the first time a SOC model for solar flares succeeded in reproducing observational results for all the typical quantities that characterize a SOC model: the energy released by avalanches (E), the maximum energy released during an avalanche (P), the total duration the avalanches (T), the waiting time between one avalanche an the other (ΔT), the time integrated surface (A) and the peak surface (A^*) of the flaring region.

- The association of dimensions to the model produced threshold angles which agree with theoretical estimates (see by [Dahlburg et al. (2005)] and [Parker, 1988]), as well as typical values for the energy release that match the observational determinations.

- Spreading exponents can be estimated, and they satisfy the mutual numerical relation predicted for SOC systems.

- The fractal dimension of the avalanches produced by the model agrees well with previous observational inferences.

- The synthetic loop generated from the SOC model allows direct and geometrically unambiguous comparisons with solar flares observations, something that was virtually impossible to achieve with classical isotropic SOC models.

These successes should not make as overlook the fact that a number of significant improvements to this model are possible, and should be carried out. One of them will be to generalize the model to three spatial dimensions by adding a radial structure to the pseudo-loop. With such a modification we will be able to introduce a driving mechanism that simulates a real systematic twist within the lattice.

With respect to the 2D model, we shall investigate the consequences of changing the location and form of the driving mechanism. For instance, we could add a perturbation only near the vertical boundaries of the lattice, thus getting closer to the photospheric

driving; also, instead of adding constant amplitude driving, we could use an exponential perturbation scheme.

On the experimental side our model can produce different types of synthetic flares that could be used as benchmarks for testing and validating flare data analysis techniques.

The self-organized critical approach used to model solar flares have had considerable success since first introduced by Lu and Hamilton in 1991 [Lu & Hamilton, 1991]. Nevertheless, these classical models had reached stagnation regarding their predictive and modeling possibilities. The work presented here has re-opened the field on both the observational and the theoretical fronts.

Bibliography

[Aschwanden, 2006] Aschwanden, M. J., *Physics of the solar corona* Springer Praxis Books / Astronomy and Planetary Sciences.

[Aschwanden & Aschwanden, 2008] Aschwanden, M. J. & Aschwanden, P. 2008, ApJ, **674**, 530

[Aschwanden & Aschwanden, 2008b] Aschwanden, M. J. & Aschwanden, P. 2008, ApJ, **674**, 544

[Aschwanden et al., 2000] Aschwanden, M. J., Tarbell, T. D., Nightingale, R. W., Schrijver, C. J., Title, A., Kankelborg, C. C., Martens, P., Warren, H. P. 2000, Astrophys. J., **535**, 1047

[Aschwanden & Parnell, 2002] Aschwanden, M. J. & Parnell, C. 2002, ApJ, **572**, 1048

[Aschwanden et al., 2002] Aschwanden, M. J., De Pontieu, B., Schrijver, C. J. & Title, A. M. 2002b, Solar Phys., **206**, 99

[Bak, 1996] Bak, P., 1996, *How nature works*, Springer/Copernicus, New York.

[Bak, Tang & Wiesenfeld, 1988] Bak, P., Tang, C. and Wiesenfeld, K., 1988, Phys. Rev. Lett. **59**, 381

[Bélanger et al., 2007] Bélanger, E., Vincent, A., & Charbonneau, P. 2007, Solar Phys., **245** (1), 141

[Bromund et al., 1995] Bromund, K. R., McTiernan, J. M. and Kane, S. R., 1995, Astrophys. J., **455**, 733

[Carrington, 1859] Carrington, R. C., 1859, MNRAS, **20**, 13-15

[Charbonneau et al., 2001] Charbonneau, P., McIntosh, W., Liu, H . & Bogdan, T.J. 2001, Solar Phys. **203**, 231

[Choudhuri, 1998] Choudhuri, A. R. 1998. The physics of fluids and plasmas: an introduction for astrophysicists. New York: Cambridge University Press.

[Clar et al., 1995] Clar, S., Drossel, B. & Schwabl, F. 1995, Phys. Rev. Lett., **75**, 2722

[Crosby et al., 1993] Crosby, N. B., Aschwanden, M.J. and Dennis, B. R. 1993, Solar Phys. **143**, 275

[Crosby et al., 1998] Crosby, N. B., Vilmer, N., Lund, N., and Sunyaev, R. 1998, A & A, **334**, 299

[Dahlburg et al., 2005] Dahlburg, R. B., Klimchuk, J. A., & Antiochos, S. K. 2005, ApJ, **622**, 1191

[Dennis, 1985] Dennis, B. R. 1985, Solar Phys.,**100**, 465

[Feder, 1988] Feder, J. 1988, Fractals (Plenum press: New York)

[Galsgaard, 1996] Galsgaard, K., 1996, A&A, **315**, 312

[Georgulis & Vlahos, 1996] Georgoulis, M. K. & Vlahos, L. 1996, ApJ, 469, L135

[Georgulis & Vlahos, 1998] Georgoulis, M. K., & Vlahos, L. 1998, A&A, 336, 721

[Georgulis et al, 2001] Georgoulis, M. K., Vilmer, N. & Crosby, N. B. 2001, A&A, **367**, 326

[Ginzburg, 1946] Ginzburg, V. L. 1946, On solar radiation in the radio spectrum. Comptes Rendus (Doklady) de l'Académie de Sciences de l'URSS. **52**, 487

[Golub & Pasachoff, 1997] Golub, L. & Pasachoff, J.M. 1997, "The Solar Corona", Cambridge University Press, Cambridge.

[Hodgson, 1859] Hodgson, R. 1859, MNRAS, **20**, 15-16

[Hughes et al., 2003] Hughes, D., Paczuki, M., Dendy, R. O., Helander, P. & McClements, K. G. 2003, Phys. Rev. Lett., **90**, 131101

[Isliker, Anastasiadis & Vlahos, 2000] Isliker, H., Anastasiadis, A. & Vlahos, L. 2000, A & A, **363**, 1134

[Isliker et al, 1998] Isliker, H., Anastasiadis, A., Vassddialiadis, D. & Vlahos, L. 1998, A & A, **335**, 1085

[Jensen, 1998] Jensen, H. J. 1998, Self-organized criticality (Cambridge: Cambridge University Press)

[Kadanoff et al, 1989] Kadanoff, L. P., Nagel, S. R., Wu, L., & Zhou, S. 1989, PRA, **39**, 6524

[Kivelson & Russel, 1995] Kivelson M. G., Russel C. T., 1995, Introduction to space physics Cambridge University Press

[Klimchuk, 2007] Klimchuk, J.A. 2006, Solar Phys., **234**, 41

[Krucker & Benz, 1998] rucker, S. and Benz, A. O. 1998, Astrophys. J., **501**, 213

[Lee et al, 1993] Lee, T. T., Petrosian, V., McTiernan, J. M. 1993, Astrophys. J., **412**, 401

[Liu et al, 2002] Liu, H.-L., Charbonneau, P., Pouquet, A., Bogdan, T. J., & McIntosh, S. W. 2002, Phys. Rev. Lett., **66**, 056111

[Longcope & Noonan, 2000] Longcope, D. W and Noonan, E. J. 2000, Astrophys. J., **542**, 1088

[Longcope & Sudan, 1994] Longcope, D. W and Sudan, R. N. 1994, Astrophys. J., **437**, 491

[Lu (1995)] Lu, E. T. 1995, ApJ, **446**, 109

[Lu & Hamilton, 1991] Lu, E. T and Hamilton, R. J. 1991, Astrophys. J., **380**, L89

[Lu et al., 1993] Lu, E. T., Hamilton, R. J., McTiernan, J. M. and Bromund, K. R. 1993, Astrophys. J., **412**, 841

[Mandelbrot, 1977] Mandelbrot, B. B. 1977 The fractal geometry of nature. W. H. Freeman and Company, New York

[Martyn, 1946] Martyn, D. F. 1946, Nature, **158**, 632-633

[Mikic et al., 1989] Mikic, Z., Schnack, D. D. & Van Hovenm G., 1989, ApJ **388**, 1148

[McIntosh et al., 2002] McIntosh, S. W, Charbonneau, P., Bogdan, T. J, Liu, H.-L., & Norman, J. P. 2002, Phys. Rev. E, **65**, 46125.

[Morales & Charbonneau, 2008b] Morales, L. F. & Charbonneau, P. Geophys. Res. Lett., **35**, L04108

[Morales & Charbonneau, 2008a] Morales, L. F. & Charbonneau, P. 2008, ApJ, **682**, (1), 654

[Morales & Charbonneau, 2008c] Morales, L. F. & Charbonneau, P. 2008, submitted to ApJ.

[Muñoz et al., 1999] Muñoz, M. A., Dickman, R., Vespignani, A. and Zapperi, S. 1999, Phys. Rev. E, **59** (5), 6175

[Norman et al., 2001] Norman, J. P., Charbonneau, P., McIntosh, S. W., and Liu, H.-L. 2001, ApJ, **557**, 891

[Parker, 1983] Parker, E. N. 1983, Astrophys. J., **264**, 642.

[Parker, 1988] Parker, E. N. 1988, Astrophys. J., **330**, 474.

[Parker, 1979] Parker, E. N. 1979, *Cosmical Magnetic Fields,* Claredon Press, Oxford.

[Parnell & Jupp, 2000] Parnell, C. E. and Jupp, P. E. 2000, Astrophys. J., **529**, 554.

[Podladchikova & Lefebre, 2006] Podladchikova, O. & Lefebre, B. 2006 Solar Actvity and its Magnetic Origin. Proc. IAU Symposium **233**, 2006

[Priest & Forbes, 2000] Priest, E. & Forbes, T. 2000, "Magnetic Reconnection", Cambridge University Press, Cambridge.

[Priest, 1982] Priest, E. R. 1982, "Solar Magneto-Hydrodynamics", D. Reidel Publishing Company, The Netherlands.

[Shimizu, 1995] Shimizu, T., 1995, *Publ. of the Astronomical Society of Japan*

[Schuster, 1989] Schuster, H. G. 1989 Deterministic Chaos: An introduction. Wiley-VCH, Weinhein

[Uritsky et al., 2001] Uritsky, V. M., Klimas, A. J. & Vassiliadis, D. 2001, Geophys. Res. Lett., **28** 3809

[Uritsky & Klimas, 2004] Uritsky, V., M. & Klimas, A. J. 2004, Scaling and predictability of complex geospace disturbances, Substorms-7, Proceedings of the 7th International Conference on Substorms.

[van Ballegooijen, 1986] van Ballegooijen, A. A. 1986, Astrophys. J. **311**, 1001

[Van Helden, 1996] Van Helden, A. 1996, *Galileo and Scheiner on sunspots.* Proc. Am. Phil. Soc. **140**, 358

[Vlahos et al., 1995] Vlahos, L., Georgoulis, M., Kluiving, R., and Paschos, P. 1995, A&A, **299**, 897

[Veronig et al., 2002] Veronig, A., Temmer, M., Hanslmeier, A., Otruba, W. & Messerotti, M. 2002, A&A, **382**, 1070

[Warren & Warshall, 2001] Warren, H. P. & Warshall, A. D. 2001, ApJ, **560**, L87

[Wheatland, 2000] Wheatland, M. S. 2000, ApJL, **536**, L109

[Withbroe, 1981] Withbroe, G. L. 1981, In *Activity and Outer Atmosphere of the Sun* SAAS-FEE 11 P. 1. **47**, 251

[Yang et al., 2006] Yang, S., Gan, W. Q., Li, Y. P. 2006, Solar Phys., 238 (1), 61

[Yashiro et al,, 2006] Yashiro, S., Akiyama, S., Gopalswamy, N. & Howard, R. A. 2006, ApJ, 650 (2), L143

[Zirker & Cleveland, 1993] Zirker, J. B. & Cleveland, F. M, 1993, Solar Phys., **145**, 119

Acknowledgements

I want to begin by thanking my supervisor Paul Charbonneau. In the first place, I want to thank him for taking the chance of hiring an unknown student from the other side of the world. Second, I want to thank him for his patience and dedication in order to help me through all the different processes involved in my PhD and for his constant support when results seemed distant. Third, I want to thank him for the liberty he gave me furing this work. Finally, I am grateful for all time he spent to make easier my adaptation to a new country, a new language and above all an unknown weather and for always trying to understand me throughout my constant 'mélanges' between English, French and Spanish.

To the Département de Physique of the Université de Montréal for giving giving me support during this years. To the present and past members of the Groupe de Recherche en Physique Solaire for the many times they gave me a hand. To the professors of the Université de Montréal for their dedication, specially to Prof. Claude Carignan who helped me understand the universe outside the heliosphere. To my canadian friends, mostly to Brigitte who helped me (and still does) with my constant mispronunciations of French. To my argentinian friends that always supported me in spite of the distance. To my best friend Andrea who always finds time to be near me.

Last but not least to my family. To my parents and my sister Analia and my brother Javier for their long-term and unconditional support. To Gui who was and is by my side making my life happier and to our son, Francisco, for the joy of these months and for not complaining too much when I am off to work. Finally I want to thank God.